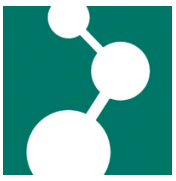

Max Planck Graduate Center
mit der Johannes Gutenberg-Universität

Mechanisms of reversible underwater adhesion in ladybug beetles

Pranav Sudersan
born in Alappuzha, India

Dissertation

for attaining the academic degree of
'Doctor rerum naturalium' (Dr.rer.nat.)
of the department
09 – Chemistry, Pharmaceutics, and Geoscience
of the Johannes Gutenberg University
Mainz

MAY 2023

This dissertation work was carried out from February 2019 until April 2023 in the department of [redacted] under the group of [redacted] at the Max Planck Institute for Polymer Research, Mainz.

Date of oral examination: 17.07.2023

Dean: [redacted]

Vice Deans: [redacted]

Supervisors

[redacted]

[redacted]

Examiners

1. [redacted]
2. [redacted]
3. [redacted]

[redacted]

Dedicated to [redacted]

Declaration

I hereby declare that I wrote the dissertation submitted without any unauthorized external assistance and used only sources acknowledged in the work. All textual passages which are appropriated verbatim or paraphrased from published and unpublished texts as well as all information obtained from oral sources are duly indicated and listed in accordance with bibliographical rules.

In carrying out this research, I complied with the rules of standard scientific practice as formulated in the statutes of Johannes Gutenberg University Mainz to insure standard scientific practice.

Here I declare that the scientific thesis I am now handing in has not yet been published at any other German University, or any university abroad, or any comparable institution, with the aim of attaining a scientific degree.

Here I also declare that I have not yet finished any other doctoral PhD or any similar gradua-tion program in any of the subjects represented by the MPGC-JGU without success.

Abstract

Many animals are known to possess the remarkable ability to stick, walk or climb on any surface. While some of the bigger animals such as monkeys or cats use their limbs or claws to mechanically grip to available protrusions on a vertical surface to climb up, some smaller animals, such as lizards and insects, can also climb on smooth surfaces where such a gripping mechanism should not be possible. On closer inspection, one would find that these animals possess specialised organs at the bottom of their feet, known as adhesive pads. The adhesive pads have naturally evolved into various forms depending on the animal: some have a dense array of hair-like structures, some are smooth and flexible, while some also secrete an adhesive fluid at the bottom. A curious property of these pads, which is not fully understood, is their ability to control adhesion instantly and achieve fast attachment and detachment as per necessity. Some animals such as ladybugs and geckos, which possess 'hairy' pads, can also surprisingly walk on underwater surfaces. Underwater adhesion is usually difficult to achieve due to the presence of interfacial water and thus, it is not entirely clear how these animals are able to accomplish this. In the present work, I attempt to resolve these mysteries by using a combination of experiments on live insects and numerical simulations. I show that, the surface tension forces due to the foot's secretions is the the primary driver of the ladybug beetle's adhesion to surfaces. Here, the balance of the different interfacial energies made by the secretion fluid with the surrounding medium is found to create the right wetting conditions for the fluid to show strong capillary forces, even when the insect's foot is submerged underwater. In order to characterise these secretions, which are of femtolitre scale volume, I develop a general method to perform surface tension measurements on microscopic liquid droplets with the help of Atomic Force Microscopy. I further show, based on a simple theoretical model, that a 'hairy' pad design of the insect's foot is not only useful to improve contact with most surfaces, but can also help control its adhesion by simply tilting the foot relative to the surface. My findings here highlight some new strategies through which underwater

adhesion can be achieved and controlled, which could potentially inspire the design of artificial reversible adhesives.

Zusammenfassung

Viele Tiere besitzen die bemerkenswerte Fähigkeit, auf jeder Oberfläche zu bleiben, zu gehen oder zu klettern. Während einige der größeren Tiere wie Affen oder Katzen ihre Gliedmaßen oder Krallen benutzen, um sich mechanisch an vorhandenen Vorsprüngen auf einer vertikalen Oberfläche festzuhalten, um hinaufzuklettern, können einige kleinere Tiere wie Eidechsen und Insekten auch auf glatten Oberflächen klettern, wo ein solcher Greifmechanismus nicht möglich sein sollte. Bei näherer Betrachtung stellt man fest, dass diese Tiere spezialisierte Organe an der Unterseite ihrer Füße besitzen, die als Haftballen bekannt sind. Die Haftballen haben sich auf natürliche Weise entwickelt und weisen je nach Tier verschiedene Formen auf: Einige haben eine dichte Anordnung haarähnlicher Strukturen, andere sind glatt und flexibel, während einige auch eine klebrige Flüssigkeit an der Unterseite absondern. Eine interessante Eigenschaft dieser Ballen, die noch nicht vollständig erforscht ist, ist ihre Fähigkeit, die Adhäsion instantan zu kontrollieren und sich je nach Bedarf schnell anzuhaften und abzulösen. Einige Tiere wie Marienkäfer und Geckos, die 'haarige' Haftballen besitzen, können erstaunlicherweise auch auf Unterwasseroberflächen laufen. Adhäsion unter Wasser ist in der Regel aufgrund des Vorhandenseins von Wasser an der Grenzfläche schwierig zu erreichen, und es ist daher nicht ganz klar, wie diese Tiere dies erreichen können. In der vorliegenden Arbeit versuche ich, diese Rätsel zu lösen, indem ich eine Kombination aus Experimenten an lebenden Insekten und numerischen Simulationen verwende. Ich zeige, dass die Oberflächenspannungskräfte, die durch die Sekrete des Fußes hervorgerufen werden, die Hauptursache für die Adhäsion des Marienkäfers an Oberflächen sind. Das Gleichgewicht zwischen den verschiedenen Grenzflächenenergien der Sekretionsflüssigkeit und dem umgebenden Medium schafft die richtigen Benetzungsbedingungen, damit die Flüssigkeit starke Kapillarkräfte entfalten kann, selbst wenn der Fuß des Insekts unter Wasser getaucht ist. Zur Charakterisierung dieser Sekrete, deren Volumen im Femtoliterbereich liegt, entwickle ich eine allgemeine Methode zur Messung der Oberflächenspannung an mikroskopis-

chen Flüssigkeitströpfchen mit Hilfe der Rasterkraftmikroskopie. Darüber hinaus zeige ich anhand eines einfachen theoretischen Modells, dass ein "haariger" Fuß des Insekts nicht nur nützlich ist, um den Kontakt mit den meisten Oberflächen zu verbessern, sondern auch dazu beitragen kann, die Adhäsion zu kontrollieren, indem der Fuß einfach relativ zur Oberfläche verkippt wird. Meine Ergebnisse zeigen einige neue Strategien auf, mit denen die Haftung unter Wasser mit Hilfe einer vermittelnden Flüssigkeit erreicht und kontrolliert werden kann, was die Entwicklung künstlicher reversibler Klebstoffe inspirieren könnte.

Contents

1. Introduction

1.1. Motivation and outline

In our everyday lives, we encounter various animals such as lizards or insects which can effortlessly climb on slippery windows or walls. This ability has fascinated human beings for centuries as it is an action we can't perform ourselves without relying on protrusions to grip with our fingers. Over the past decades, a number of controlled studies performed on animals ranging from geckos to beetles have shed some light on this mysterious 'superpower' which allow such animals to stick to surfaces. In general, their legs have a very special design which enhances their adhesion to a surface. The specific design may vary depending on the species we are looking at. For example, geckos possess hierarchical hairy nano-structures, ants or frogs have smooth and flexible foot, while certain flies or beetles rely on a sticky liquid secreted by their legs. In all cases, the specific design of the animal's leg allows it to maximise contact area, even when the surface has microscopic roughness. Roughness of a surface can otherwise drastically reduce the real contact area, which is the reason why our fingers don't stick to a wall like an insect.

Recently it was shown that some beetles can use their hairy adhesive legs to not only walk on surfaces in air, but also while underwater! This is surprising because when we look at marine animals, their strategies to achieve adhesion on underwater surfaces are completely different from that of terrestrial animals. For example, octopuses rely on suction cups on their tentacles which are manipulated using muscular control to stick and release from the sea rocks. Another example would be barnacles or mussels, which secrete an adhesive protein to more or less remain permanently attached to underwater surface such as the hulls of ships. In comparison, the humble beetle in question only has microscopic hairy structures on their leg. While their hairs do contain a tiny amount of secretion, this liquid does no possess any of the polydopamine or catechol groups, as seen in a mussel or barnacle's

adhesive secretion. Such molecular groups in the secretion are important, since they enable underwater adhesion via strong polar interactions with the surface, as well as, by displacing the intermediate water layer that might hinder contact and adhesion. Ladybugs, on the other hand, are known to only secrete an oily liquid mixture of mostly hydrocarbons. Thus the question arises how they manage to adhere so well to underwater surfaces?

Another curious ability of these animals is that they can not only stick well to most surfaces, but can also easily detach themselves as per necessity. Of course, simply having sticky legs won't be much useful if they also desire to move around! But, we see insects or lizards easily sticking to our home's walls while also running around just like they would below on the floor. It seems that the special design of their foot should also allow a certain level of control over adhesion. In the case of the ladybug, for example, perhaps the hairy structures on its legs could somehow influence its net adhesion depending on how the the leg is oriented relative to the surface. What strategies could the ladybug then utilise to efficiently control its legs to modulate its adhesion for locomotion?

The primary aim of this thesis is to understand the fundamental mechanisms by which such terrestrial beetles are able to reversibly adhere and walk underwater. A previous study hypothesised that an air bubble trapped around the beetle's hairy leg should mediate its adhesion through surface tension forces. In Chapter 3, I will test this claim by performing adhesion experiments on live ladybug beetles. The experimental results are compared with theoretical predictions based on a model to quantify the relative contribution of the trapped air bubble in underwater adhesion. Here, I find that its rather the surface tension force resulting from the insect's oily secretion that plays a dominant role in underwater adhesion. In order to characterise the nature of such secretions, in Chapter 4, I develop a new method to measure surface tension of microscopic liquid droplets. The method relies on Atomic Force Microscopy (AFM) experiments performed on a microdroplet (volume in the order of femtolitres) deposited on a surface, together with numerical simulations to calculate surface tension. Chapter 5 focuses on the aspect of reversibility of insect adhesion. A simple model is presented showing the different mechanisms by which the insect possessing a hairy foot could easily modulate the adhesion force by mechanically reorienting its leg. This would result in an in-homogeneous deformation of its hairs, resulting in a significant reduction of the leg's net adhesion force. Finally in Chapter 6, I will discuss the possible impact of my work in the

fundamental understanding of animal adhesion, with a potential to develop new bio-inspired reversible adhesives that would show good adhesion in both air and underwater conditions.

My research work described in the subsequent chapters have been either already published in scientific journals or is currently under peer-review. Chapter 3 and Chapter 5, respectively, are taken from my following publications:

1. **Sudersan, P.**; Kappl, M.; Pinchasik, B. E.; Butt, H. J.; Endlein, T. Wetting of the Tarsal Adhesive Fluid Determines Underwater Adhesion in Ladybird Beetles. Journal of Experimental Biology 2021, 224 (20). `https://doi.org/10.1242/jeb.242852`.
2. **Sudersan, P.**; Kappl, M. Mechanisms of Detachment in Fibrillar Adhesive Systems. Journal of Theoretical Biology 2023, 557, 111315. `https://doi.org/10.1016/j.jtbi.2022.111315`.

My work described in Chapter 4 has already been submitted to a journal and, as of April 2023, is being presently reviewed. All works were and will be published under the open-access CC BY 4.0 license, which allows me to reuse the published material for this dissertation. All reported experimental and theoretical work reported in this dissertation were performed by myself, unless explicitly stated otherwise.

1.2. Forces in nature

Before we look at the detailed adhesion processes that exist within the animal kingdom, let us first address a more fundamental question: How do things stick to each other? The answer to this question of course depends on what kind of "things" are we looking at and under what conditions. The standard model of physics has so far found four fundamental forces in nature, which are namely, electromagnetic, gravitational, strong and weak nuclear forces[25]. Here, electromagnetic force is the most relevant in the context of macroscopic interactions. It not only explains some obvious cases of attraction or repulsion caused due to charged bodies or electric current in a coil, but rather is quite ubiquitous in nature and is the fundamental source of most physical and chemical interactions that one may encounter. Depending on the specific conditions, electromagnetic force can manifest in various forms. Each of these forms of force could instead be conveniently expressed in terms of a model that relies on a relevant set of experimental observations specific to that condition. For example, many of us might have experienced during a nice summer holiday in a beach that sand needs to be wet in order for them to be sticky enough to make a sand castle. Any attempts to make a castle with dry sand will only end in frustration. What is the reason for this simple phenomenon? And how would one estimate the forces that seem to be keeping the sand particles intact when wet? In this section, I will overview the several relevant forms through which electromagnetic force expresses itself in nature. The mechanisms of these different forces would later provide us the necessary foundation to understand the adhesive properties of an animal foot.

1.2.1. van der Waals forces

All molecules inherently show attractive interaction force with any other molecule when they are close to each other. The forces referred to here are different from the ones responsible for atoms to covalently bond with other atoms via sharing electrons. Rather, even neutral molecules like Hydrogen or Helium possess attractive forces, which makes it possible for these gases to be condensed into liquid state if cooled sufficiently. This seemingly mysterious universal force that exist between all molecules are called "van der Waals" forces, in honour of the Dutch physicist Johannes Diderik van der Waals[52].

The origin of van der Waals forces can be understood by considering electrostatic dipole interactions between molecules[17]. For example, depending on the relative electronegativity and bond orientation between the constituent atoms, many molecules possess an inherent dipole moment. This could be imagined as an apparent shifting of the electron cloud towards the more electronegative atom of the molecule, leading to a dipole like behaviour. Classical electrostatic theory shows that the interaction potential between two dipoles depends on the their respective dipole moments (μ_1, μ_2), orientation angles $(\theta_1, \theta_2, \phi)$ as well the separation distance (D), as given by:

$$V = \frac{\mu_1 \mu_2}{4\pi\mu\epsilon_0 D^3} \left(2\cos\theta_1 \cos\theta_2 - \sin\theta_1 \sin\theta_2 \cos\phi\right)$$

Molecules are however free to reorient themselves randomly due to thermal motion. If we consider two freely rotating dipole molecules, their net interaction will be a thermal average of all possible orientations following the Boltzmann distribution. This ultimately results in a net attractive force between the molecules. This is termed as *Keesom interaction*, whose potential energy follows: $V_{keesom} = \frac{-C_{keesom}}{D^6}$. Another possible situation is when a dipole molecule interacts with a polarizable molecule. Here, a dipole moment is induced into the polarizable molecule, resulting in a permanent to induced dipole interaction. A similar thermal averaging results in a net interaction called as *Debye interaction*, with potential energy: $V_{debye} = \frac{-C_{debye}}{D^6}$.

Keesom and Debye interactions rely on at least one molecule acting as a permanent dipole and thus fail to explain the attractive interaction seen in dipole-neutral molecules such as Hydrogen or Helium. However, even neutral molecules create momentary dipoles at every instant as a result of their electron clouds oscillating around the nuclei, a mechanism that can be described in detail by quantum mechanical fluctuation theory. To put it simply, when any two molecules with oscillating electron clouds come near by, their electron clouds on average have a higher probability to assume orientations that favour attractive interactions. These resultant net attractive forces are called London dispersion forces, which exist universally between all molecules. Similar to others, it follows a potential energy dependence as: $V_{london} = \frac{-C_{london}}{D^6}$.

van der Waals between two molecules is thus defined as the sum of Keesom, Debye and London dispersion interactions: $V_{vdW} = \frac{-C_{vdW}}{D^6} = \frac{-C_{keesom}}{D^6} + \frac{-C_{debye}}{D^6} + \frac{-C_{london}}{D^6}$. Surprisingly, it has been observed that the London dispersion term usually domin-

ates, even for highly polar molecules such as alcohols. This further highlights the rather important and ubiquitous nature of van der Waals forces. Typically, van der Waals forces are considered relevant below distance $D < 10$ nm, beyond which the force trend decreases more steeply. This steep decrease in force is due to a so-called retardation effect as a consequence of the finite speed of electrostatic interactions in comparison to the electron cloud oscillation rates.

A relatively convenient model to estimate van der Waals forces between *macroscopic* bodies is by relying on the so-called Hamaker approach. Here, a simplified assumption of pairwise addition of the interacting dipole moments between each pair of molecules is used, without considering the possible influence of a third molecule's dipole on the pair's interaction. In this manner, the net attractive van der Waals force can be derived by integrating all interacting pairs of molecules. For two infinite planes, the resulting force per unit area is derived to be:

$$f_{vdW,plane} = \frac{-A_H}{6\pi D^3} \tag{1.1}$$

where A_H is the Hamaker constant for the two bodies separated by a given medium. For other arbitrary geometries, deriving a similar expression between the two macroscopic bodies by integration would be challenging. In such cases, one may use the Derjaguin approximation[28] to obtain a relation for van der Waals force, provided that the geometry's curvature is much larger than the characteristic decay length of the interaction force.

The above mentioned Hamaker approach is only an approximation because pairwise additivity of interactions is not valid for cases where the molecules are densely packed (for e.g. in solids), where the influence of the neighbouring molecules on a molecular pair's interaction potential can no longer be neglected. A more quantitative method for estimating van der Waals forces was introduced by Lifshitz based on previous work by Casimir[65]. In this approach, the electromagnetic fluctuations in the molecule, which are related to material's dielectric properties, are considered. Spectroscopic data can thus be used for precise estimation of the van der Waals force between two bodies by using Lifshitz theory. In fact, even the above mentioned Hamaker constants can be calculated from this method. A detailed description of Lifshitz theory however goes beyond the scope of my dissertation. I would direct the reader to Chapter 3 of the book by Butt and Kappl[17] for a good introduction on this topic and Parsegian's book[74] for more details.

The strength of van der Waals attraction between two bodies is determined by two factors: 1) the surface topography of the contacting bodies and 2) the dielectric properties of the bodies and the in-between medium. If we look at the macroscopic interaction relation (equation 1.1), we see that the force scales as an inverse power exponent of three rather than six that is seen for a microscopic interaction between two molecules. Thus, macroscopic van der Waals interaction force can be sufficiently long ranged for it to have a significant contribution between two bodies, provided they are under close contact. However, a close contact between two bodies can be severely hampered if their surface topography also changes beyond the length scales under which van der Waals interactions start to have an effect. For example, a typical value of Hamaker constant for two perfectly flat materials in vacuum is of the order of 10^{-20} Joules[17]. If the surfaces are each of 1 mm^2 area, equation 1.1 tells us that the attractive force would drop from roughly 0.5 N to 0.004 N when the separation distance, D, is increased from 1 nm to just 5 nm! This means that for a rough surface, if the peaks and valleys of the topography differ by 5 nm or more, the total effective contact distance is significantly reduced, which consequently results in a low net attraction due to van der Waals force. Further, if an intermediate layer of water is present, the Hamaker constant between the surfaces is further reduced by an order of magnitude due to the high dielectric constant of water. Thus in underwater conditions, van der Waals attraction between surfaces will no longer be significant. As we will see later, nature has figured out some clever ways to overcome these limitations in order to achieve strong van der Waals adhesion. For example, geckos possess a dense array of microscopic hair-like structure called setae on their foot, which further sub-divide into soft nano-scale spatulae structures that enable them to achieve a good close contact to most surfaces despite roughness. In this manner, a gecko takes advantage of van der Waals forces to stick to surfaces[7]. We will discuss the topic of biological adhesion in more detail in a later section.

1.2.2. Capillary forces

Imagine the interface between two fluid phases, for example, the surface of a liquid surrounded by ambient air. If we zoom into this interfacial region up to the molecular scale, we would find that the molecules of the liquid and air interact with each other through various intermolecular forces, such as van der Waals force (as described above) or hydrogen bond forces. Usually, molecules of one kind are

preferably more attracted to its same kind. This means that, unlike the molecules sitting inside the bulk liquid, a liquid molecule near the interface interacts with the neighbouring liquid molecules from the same phase, and with the air molecules from the surrounding phase in a nonuniform fashion. This unbalanced net interaction can be considered to be an energetic penalty wherever an interface exists. We term this energetic penalty as *surface* energy, or more generally, as *interfacial* energy. Formally, interfacial energy is the energy required to increase a unit area of a given two-phase interface. Alternatively, one may also imagine the interface to be under a constant state of tension along its plane as a consequence of the net unbalanced molecular interaction near the interface. This tension acting per unit length along the interface is termed as *surface tension* or *interfacial tension*[16]. Both interfacial energy and interfacial tension have identical numerical values, where, the former is typically expressed in the units of mJ/m^2, while interfacial tension has the units mN/m.

Even though interfacial tension has a molecular scale origin, it effects several macroscopic phenomena. For example, a small water droplet suspended in air assumes a spherical shape to minimise its total interfacial energy, since a sphere is the geometric shape with the lowest surface area for a given volume. Similarly, several other phenomena such as, the rise or depression of liquids inside a capillary tube, wetting of liquids on different surfaces, adhesion of wet sand particles, to name a few, can all be explained to be a result of interfacial tension. For a more formal mathematical analysis, it is imperative to study one of the fundamental equations which resides at the heart of all interfacial phenomena: the *Young-Laplace equation*, which was introduced by Thomas Young (1805) and Pierre-Simon Laplace (1806) independently and later expressed in a simpler form by Carl Friedrich Gauss (1830) as commonly used in the present time[100].

Before we look at the final expression, let us quickly go through a simple way to derive the Young-Laplace equation. Consider a small circular area element of diameter, d, on an arbitrary curved interface between two phases. The curvature of this area element can be imagined to be a result of a certain pressure difference, ΔP, between the two phases. Now, we can perform a force balance across the element, where, ΔP on the area is balanced by the normal component of the net force due to the interfacial tension, γ. The second term can be calculated by considering two orthogonal lines of length, dl, along the area element and integrating along quarter of the total contact line (Figure 1.1). Thus, the force balance looks like:

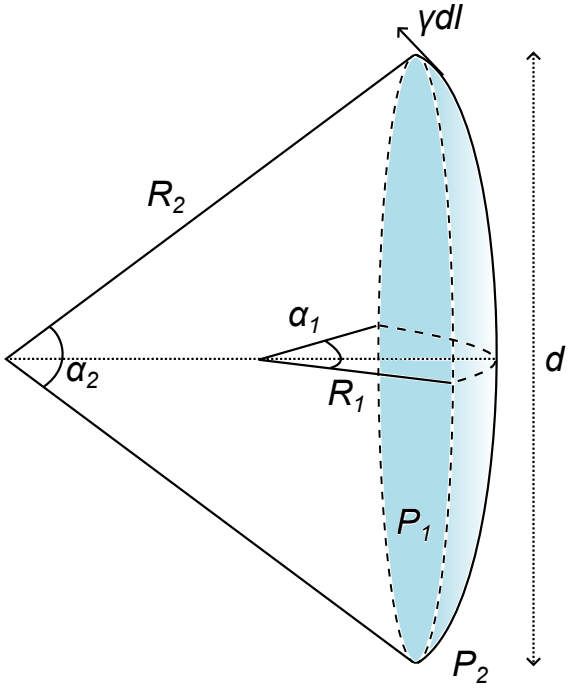

Figure 1.1.: Derivation of Young-Laplace equation

$$\Delta P \cdot \pi d^2/4 = \int \gamma \cdot dl \cdot \sin\alpha_1 + \gamma \cdot dl \cdot \sin\alpha_2 \tag{1.2}$$

For a small area element, $\sin\alpha_1 \approx \alpha_1 = \frac{d}{2R_1}$ and $\sin\alpha_2 \approx \alpha_2 = \frac{d}{2R_2}$. Integrating equation 1.2 and simplifying, we obtain the final expression of the Young-Laplace equation, given by:

$$\Delta P = \gamma \cdot \left(\frac{1}{R_1} + \frac{1}{R_2}\right) \tag{1.3}$$

Here, ΔP is the so called Laplace pressure between an interface, whose shape can be expressed in terms of its principal curvatures R_1 and R_2. Thus, for a given liquid interface if we can easily calculate the Laplace pressure, surface tension or the interface shape by using the Young-Laplace equation if we know the remaining two parameters. This is quite powerful, because we can calculate the equilibrium condition of a liquid interface using only three parameters, which would otherwise have required a rigorous analysis of the various intermolecular forces that exist for a given interface.

To illustrate this with an example, let us consider the case of pair of flat and rigid substrates separated by a thin layer of liquid (Figure 1.2). One may have

experienced a similar condition when you accidentally drop your credit card on a wet floor or table, where it can be a little tricky to pick it back up, due to an apparent adhesion between the card and the wet surface. What is the origin of this adhesive force? Of course, one may analyse this situation rigorously from a molecular point of view, where, the solid, liquid and air molecules interact with each other at their respective interfaces and ultimately cause a net attraction between the two substrates mediated by the liquid. However instead, we will calculate this adhesion force in a much simpler way by utilising the Young-Laplace equation. Referring to Figure 1.2, the liquid layer at the air-liquid interface will assume a curved shape, where, the Laplace pressure is related to the liquid curvature and surface tension as given by equation 1.3. The net adhesion force between the liquid layer and the solid substrate will have two components: 1) Force due to Laplace pressure acting along the solid-liquid contact area, A, and 2) The vertical component of the surface tension force acting along the solid-liquid contact perimeter, L. Together with equation 1.3, we can thus express the net adhesion between the two substrates as:

$$F_{cap} = \gamma \cdot \left(\frac{1}{R_1} + \frac{1}{R_2}\right) \cdot A + \gamma \cdot L \cdot \sin\theta \tag{1.4}$$

Here, the adhesive force, F_{cap}, between two solid surfaces separated by a thin liquid bridge is generally termed as the *capillary force* . Thus, if we know the shape of the liquid meniscus, the contact angle, θ, between the liquid and the surface, the surface tension of the liquid and the contact area/lengths, we can use equation 1.4 to calculate the capillary force. For more complicated cases, for example, when the surface has an arbitrary geometry or the solid-liquid interface follows a constant contact line boundary condition ('*pinning*') rather than having a constant contact angle, then calculating the principle curvatures, R_1 and R_2, is not trivial. In such cases, the equilibrium shape of the liquid interface can be numerically calculated by following an interfacial energy minimisation routine in a software such as Surface Evolver (described later in Chapter 2)[12].

In equation 1.4, the static contact angle, θ, is an important parameter within the context of wetting phenomena of liquids to different surfaces. The specific value of θ between a liquid drop and a solid surface depends on the relative interfacial energy values of each of the solid-liquid (γ_{sl}), liquid-gas (γ_{lg}) and solid-gas (γ_{sg}) interfaces near the three-phase contact line. The relation between the contact angle and these

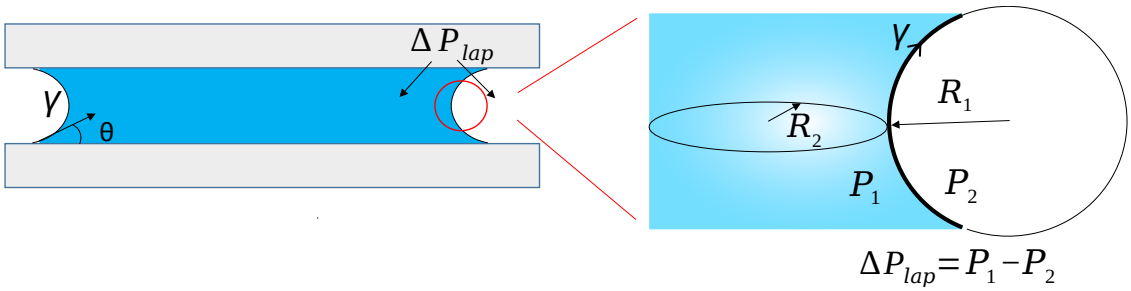

Figure 1.2.: Capillary bridge between two flat surfaces

interfacial tensions under equilibrium condition is described by the *Young-Dupré equation*:

$$\gamma_{lg} \cos\theta = \gamma_{sg} - \gamma_{sl} \tag{1.5}$$

In the field of wetting[27], surfaces are, by convention, categorised into two types depending on how well water wets on them. When a water drop has an equilibrium contact angle less than 90°, the surface is said to be *hydrophilic*. On the other hand, for θ greater than 90°, the surface is *hydrophobic*. Under ideal conditions, a surface should have a constant contact angle value. However, real surfaces have random micro or nano-scale heterogeneity, either physical or chemical in nature. Thus the quantity *contact angle hysteresis* is measured for a given liquid on a surface to get a more complete picture of the surface wetting properties. This measurement is made by observing the contact angle of a liquid interface while it is either advancing along the surface (θ_{adv}) or receding back (θ_{rec}). The difference between the advancing and receding contact angles is called as the contact angle hysteresis, $\theta_{hys} = \theta_{adv} - \theta_{rec}$. An ideal surface would have $\theta_{hys} = 0°$, while higher values of θ_{hys} (typically greater than 10°) indicate a higher level of structural or chemical heterogeneity on the surface[18]. The static contact angle of the liquid on a surface, θ, can take any value between θ_{adv} and θ_{rec}, depending on how the drop is placed on the surface.

Knowledge of contact angle is important since it influences the strength of capillary force due to a liquid bridge (equation 1.4). In general, the liquid should wet the surface quite well (i.e. low θ) for it show strong capillary forces. The presence of a liquid bridge also eliminates the problem of 'close contact' seen in the case of van der Waals force between two rough surfaces. If the liquid can wet the surface, it would fill all the valleys of the surface topography and thus can interact quite well

with both surfaces due to the large contact area. Thus, the two surfaces separated by a liquid bridge can in principle show even higher attraction due to capillary force when compared to their van der Waals force in the absence of the liquid bridge.

1.2.3. Other forces

1.2.3.1. Hydrodynamic forces

In the previous section, I only considered liquid under static conditions when defining the capillary force. However, when liquids are under flow, an additional force comes into picture. A classic example is where we consider two parallel plates of area, A, which are a vertical distance, Δx, apart and filled with liquid in between. The force, F required to slide one of the plates laterally at a particular velocity, Δv, while maintaining Δx is given by:

$$F = \eta A \frac{\Delta v}{\Delta x}$$

Here, η, a physical property of the liquid, termed as viscosity. The above equation tells as that the liquid offers a resistance to flow which, in this case, was induced by the motion of the plate in contact with it. One may thus imagine viscosity to be a measure of resistance offered by a liquid against flow, where the resistance force is called the *hydrodynamic force*. As one may expect, knowledge of the liquid flow profile for a given condition is necessary to calculate the hydrodynamic force. For a general case, the dynamic flow profile of a liquid is governed by the Navier-Stokes equation:

$$\rho \left[\frac{\partial \vec{v}}{\partial t} + (\vec{v} \cdot \nabla) \vec{v} \right] = \eta \nabla^2 \vec{v} - \nabla P + \vec{f} \tag{1.6}$$

where, $\vec{v}$ is the velocity vector field describing the liquid flow, ∇P is the pressure gradient in the direction of flow and $\vec{f}$is any other external force field which could influence the liquid flow, such as gravity.

We have already seen in the previous section that the capillary force required to separate two flat plates with liquid in between can be calculated from equation 1.4. But what about the hydrodynamic force? When we vertically separate the plates apart at a particular velocity, v, the liquid in between would radially flow inwards

which causes a resistance against separation. This vertical hydrodynamic force can be derived using the Navier-Stokes equation as:

$$F = \frac{3\pi\eta v r^4}{2d^3} \tag{1.7}$$

where, r is the radius of the plates (assumed to be shaped like disks here) and d is the plate separation distance[17].

1.2.3.2. Elastic forces

All solid materials undergo deformation when a certain force is applied to it. If this deformation is sufficiently small relative to the size of the material, then the material will return back to its undeformed state when the applied force is removed, similar to a spring. This property of the solid is called elasticity, where, the material deforms linearly with respect to the applied force. In the theory of solid mechanics, stress and strain are usually used as parameters to conveniently quantify the applied force and deformation. In the elastic regime, the general expression for material deformation is given by, $\sigma = E\varepsilon$, where, σ is the stress, which is applied force per unit area, ε is the strain, which is the deformation relative to the length of the material, and E is the Young's modulus, which is a physical property quantifying the material elasticity. The above expression tells us that if a material is brought into an elastically deformed state, then any other body in contact with it will experience an opposing force, called the *elastic force*, acting along the direction of material deformation.

Elastic forces can influence the net adhesion between materials if one of the contacting bodies undergoes sufficient deformation. A classical example in contact mechanics was derived by Johnson, Kendall and Roberts (JKR theory), which expands on Hertz theory of deformation between two material by also considering the contribution of adhesion between the materials[54]. Here, the release of elastic energy due to deformation is compensated by a gain in the surface energy due to the adhesive interaction between the two surfaces during the contact process. The adhesion force, F, between a rigid sphere of radius, R, in contact with a flat elastic surface of modulus, E, can then be derived to be:

$$F = \frac{3}{2}\pi\omega R \tag{1.8}$$

Here, ω is the adhesion energy per unit area of contact between the two materials. If both bodies had been completely rigid, the adhesion force would be equal to $2\pi\omega R$, as derived by Derjaguin. This difference illustrates the effect of the stored elastic energy on adhesion. It is quite curious that the adhesion force in equation 1.8 above is independent of the elastic modulus, E. This is however purely a geometric effect. In the case of a different contact geometry, for example, a rigid cylinder of radius, R, in contact with a flat elastic surface[58], the adhesion force based on the JKR theory would depend on E, as given by:

$$F = \sqrt{8\pi R^3 E\omega}$$

1.2.3.3. Friction forces

Our discussion so far has been limited to adhesive forces, which acts along the normal direction. But what about lateral forces? If two solid bodies under contact is moved relative to one another parallel to the plane of contact, there exist a force that resists this motion. This lateral resistance force between two surfaces is called friction force. Friction has been studied over the past several centuries, where the first known systematic experiments were done by da Vinci. Despite its seemingly simple effect, the underlying mechanisms that govern friction is in fact quite complicated. No general theory exists that can predict friction based on the physical properties of the involved materials, which necessitated the creation of an entirely new branch of science devoted to its study: tribology. Here, I will briefly summarise some of the popular models used describe our current understanding of friction.

Several empirical models have been however proposed to calculate friction forces. For the case of a dry contact, Amontons law states that the friction force (F) between two rigid bodies is proportional to the normal load (N) and is independent of the apparent contact area. That is, $F = \mu N$, where the friction coefficient, μ, is an empirical constant specific to a particular pair of contacting bodies. It has been observed that μ can have two different values depending on the state of relative motion between the contacts. The static friction coefficient determines the minimum friction force necessary to initiate lateral motion, whereas, the kinetic friction coefficient gives us the constant friction force between the two bodies while they are under relative motion.

While Amontons law is correct empirically, a microscopic picture of the contact reveals that the independence of friction to contact is area is not quite true. Since roughness exists between all surfaces at various length scales, the 'real' contact area can be quite different from the macroscopic contact area. The surfaces only contact each other on these microscopic asperities, which would further deform, either elastically or plastically, due to normal load. Thus, the dependence of friction to normal load, as given by Amontons law, is in fact a result of the 'true' contact area between the microscopic asperities deforming under load. Some notable models for friction which consider this microscopic picture are the Bowden-Tabor model and the Greenwood-Williamson model[9].

For the case of wet contact, otherwise called a lubricated contact, the friction force is generally reduced due to the presence of an intermediary liquid layer between the two surfaces. Here, the thickness of the liquid layer is crucial, and leads to different regimes in the resultant friction. When the layer is thick such that the surfaces are completely separated, the system is under *hydrodynamic lubrication* regime leading to very low friction forces. Here, continuum fluid dynamics models (e.g. equation 1.6) could be used to calculate friction. For small fluid thickness in the range of molecular or surface roughness length scales, the friction force is relatively higher and independent of the fluid viscosity, i.e. under the *boundary lubrication* regime. This regime would however still show a smaller friction force when compared to the case of a dry contact, since the fluid layer reduces the surface energy. Intermediate fluid thickness results in a combined effect of both hydrodynamic interactions due to the fluid, as well as the intermittent contact of the surface asperities. Such a condition is classified under the *mixed lubrication* regime[17].

1.3. Adhesion in animals

Animals, in general, have specialised organs known as "adhesive pads" that make contact with the surface during locomotion. As the name suggests, the primary function of such adhesive pads is to ensure they can adhere or stick to a surface, either during locomotion, or stay attached to a particular spot for an extended duration without slipping away. Nature through its countless species and evolution pathways has come up with several designs of such adhesive pads relying on unique strategies to achieve adhesion. In this section, I will overview the most commonly

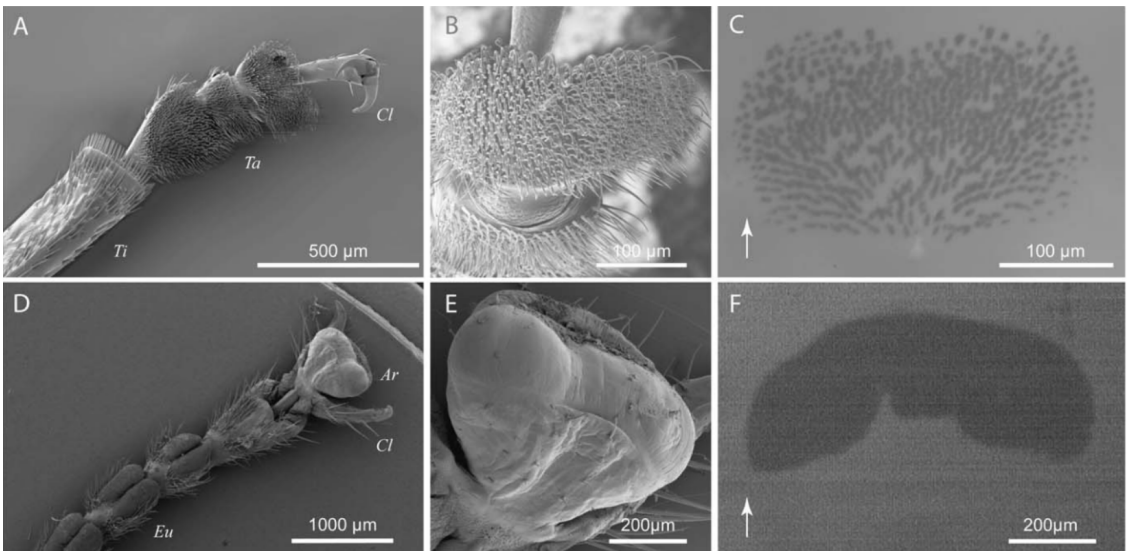

Figure 1.3.: Smooth and hairy adhesive pads of a male dock beetle (A,B,C) and Indian stick insect (D,E,F) respectively. C and F shows the corresponding contact images of the pad against a transparent glass surface[13].

studied adhesion mechanisms employed by various organisms in either air or an aquatic environment. Finally I will discuss the special characteristic of such pads that allow them to reversibly attach and detach from surfaces for countless cycles without significantly losing their adhesion capability, a process I term as "reversible adhesion".

1.3.1. Adhesion in air

Everyday experience tells us that many animals such as lizards, ants, spiders and a myriad other insects can easily climb vertically up on walls or trees, defying gravity[24,41,97]. The question on how these animals climb smooth and slippery surfaces has fascinated scientists for the past three centuries[46,85]. Clearly, their legs possess some form of adhesive properties that allow them to passively perform such a feat. For terrestrial animals in air, the geometric design of their foot, generally termed as *adhesive pads*, can be broadly classified into two types: 'smooth' and 'hairy' (Figure 1.3). Irrespective of the specific design, a general goal of an adhesive pad is to maximise its contact against any surface, since a higher contact area between the pad and surface generally result in a higher adhesion.

A 'smooth' adhesive pad can be seen in certain insects such as ants or cockroaches

as well as some amphibians like frogs. Here, the pad is composed of a very soft material, which allows it to conform to the surface roughness of certain length scales, thus enhancing the real contact between the foot and the surface. In some insects, for example in ants, the pad also secretes a tiny amount of fluid, which would make an additional contribution to the adhesion through capillary forces (Figure 1.4). The second category is the so called 'hairy' adhesive pad design, seen in certain reptiles such as geckos and other insects like house flies, beetles etc. In this case, the adhesive pad comprises of a dense array of hairlike structures, known as *setae*, where the contact with the surface occurs through its setal tips. An extensively studied example of an animal with hairy adhesive pads are geckos, since they are the largest land animals that can climb up on surfaces by relying primarily on their leg's adhesion rather than mechanical gripping. It was shown that an individual seta of the gecko's pad interacts with a surface through weak attractive van der Waals forces[7]. Since these setae have flat spatulae shaped tips that are very small of the order of 200-500 nm and are densely packed as a hierarchical array on each pads (roughly 5000 setae per mm^2), the net combined effect of all setae results in the leg having a significantly large adhesion force that can easily support the gecko's body weight[6]. The hairy adhesive pad design also enhances the real contact area by conforming to the roughness of a surface. But unlike a smooth pad, the setae does not need to be made of a very soft material. Their high aspect ratio geometry allows them to conform along the microscopic surface features simply by bending, even if the individual seta comprises of a relatively stiff material (Figure 1.4). Thus, such a design is much more resilient to mechanical wear on repeated contact, in comparison to the soft smooth pads.

Animals such as ants, bugs or frogs, irrespective of the their pad design being 'smooth' or 'hairy', are also known to secrete some fluid which mediates the pad's adhesion. The secreted fluid are typically a mixture of hydrocarbons with traces of triglycerides, fatty acids and cholesterol[5,37,51]. The role of the secreted fluid in the animal's attachment is however not completely understood. The secretion certainly does not act like a conventional 'glue', since the animal would also want to easily detach its leg for locomotion rather than staying permanently attached to a fixed spot. Forming a strong chemical bond with the surface is thus not an option. However, presence of an intermediate fluid layer can still contribute to adhesion in two ways: capillary force (equation 1.4) and hydrodynamic viscous force (equation 1.7)[29,36,61]. Our discussion from the earlier section tells us that thinner the fluid

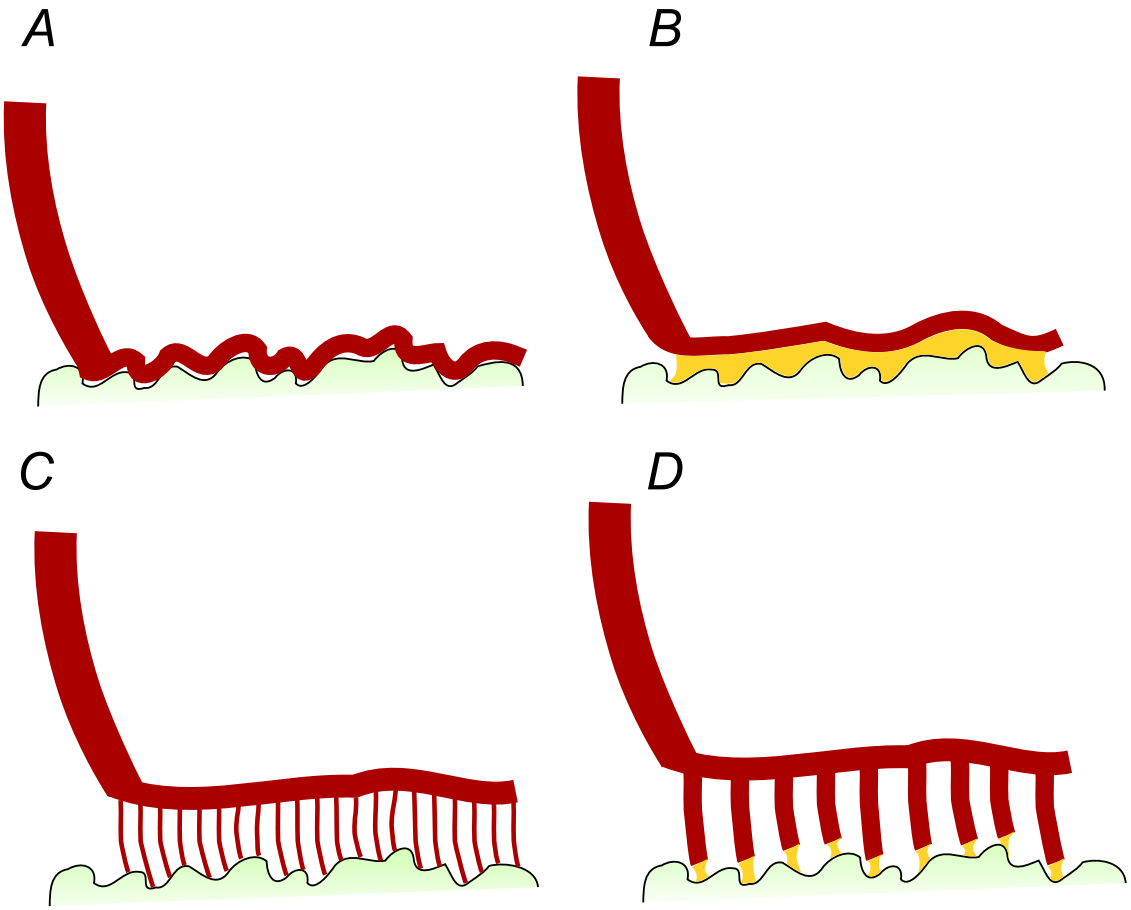

Figure 1.4.: Representative schematics showing a 'smooth' (A, B) and 'hairy' (C, D) adhesive pad in contact with an arbitrary rough surface. The specific case where the pad also secretes an adhesive fluid (yellow) is shown in B and D.

layer, stronger will be the adhesion contribution for both these kinds of forces. Insects like ladybugs do in fact secrete a very tiny amount of oily fluid, roughly one femtoliter per seta, in order to maximise adhesion[76]. But why use a secretion in the first place, since a dry contact should in principle have a relatively larger adhesion due to van der Waals force? A possible explanation to this is that for practical cases the secreted fluid in fact enhances adhesion by maximising the contact area between the leg and a surface. All surfaces, especially in a natural environment, have micro-scale roughness which would significantly reduce the real contact area if the pad were under a dry contact i.e. without any intermediary secretion. But in the presence of a secretion, the fluid would fill the gaps between the asperities of the rough surface (Figure 1.4). In this way, the secreted fluid enhances the real contact area and consequently also the adhesion of the pad relative to that of a dry contact. In this case, the adhesion is mediated by the fluid's interactions with the surface, where the fluid acts like a 'bridge' connecting the pad to the surface.

1.3.2. Adhesion underwater

Unlike terrestrial animals, marine animals such as octopuses, mussels, barnacles and cling fishes seem to rely on completely different strategies to adhere on underwater surfaces. In general, the presence of water imposes several challenges to adhesion even if the two contacting surfaces can stick quite well to one another in ambient air. Firstly, its difficult to completely drain out the intermediate water layer in order to establish a direct contact between the two adhering surfaces. Presence of the water layer significantly reduces the Hamaker constant leading to a low van der Waals adhesion. Secondly, water can erode an adhesive due to hydrolysis or swelling[92]. This is particularly a problem seen in many artificial adhesives, where, the water eventually causes a failure of adhesive contact. So how do marine animals solve this problem? Their adhesive organ design can be generally classified into two types: suction cups and glue-like adhesive proteins.

The suction cup design has been observed in several marine animals such as octopus, cling-fish[30], diving beetle[22] or midge larva[57]. Here, adhesion is achieved by generating a pressure difference between the water inside the cavity of a cup shaped structure and the surrounding water (Figure 1.5). Since water is in-compressible, deformation of the cup by muscular action is not compensated by a change in volume, which in turn creates a suction force due to the resultant pressure dif-

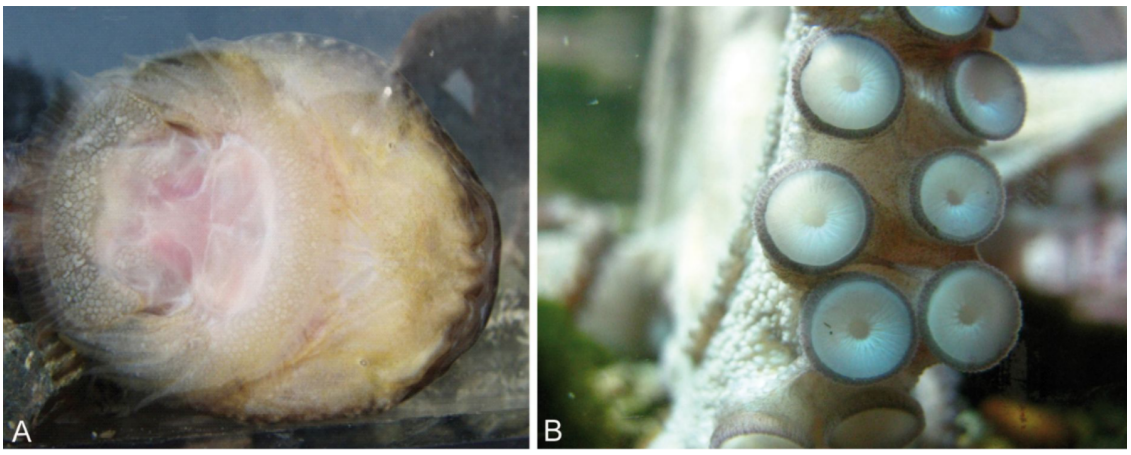

Figure 1.5.: Suction cups of a clingfish (A) and octopus (B) used as attachment organs to adhere to underwater surfaces[30]

ference. A similar muscular control can also help release the cup pressure, thus allowing the animal to easily attach and detach to an underwater surface during locomotion. In order to achieve strong adhesion, it is crucial that the rim of the suction cup is properly sealed so that the generated pressure difference can be maintained during contact. It has been observed that the suction cups of octopus or midge larve possess microscopic structures around the cup rim which could aid in the sealing of the cups, although the detailed mechanism of this process is still not completely understood[93].

On the other hand, there are several marine organisms such as mussels and barnacles that stay attached to an underwater surface by secreting some special proteins. In the case of mussels, the adhesive proteins mostly constitute 3,4-dihydroxy-L-phenylalanine (DOPA), where, the catechol group can make strong hydrogen bonds which can effectively displace water in order to bond with a hydrophilic surface such are silicate rocks[92]. A similar strategy is also employed by barnacles, where they rely on a network of adhesive nanofibers comprising of hydrophilic proteins that can bond very well to surfaces underwater[67]. In either case, the adhesive proteins here act like a glue to enable a nearly permanent underwater attachment. This makes practical sense for mussels and barnacles since they follow a sedentary lifestyle. But in order to feed on nutrients from the water more effectively, they tend to attach to rocks that experience high water currents. A strong underwater glue-like adhesive mechanism is thus essential for their normal biological function.

A particularly anomalous observation of underwater adhesion was reported in a

recent study by Hosoda and Gorb [47]. A terrestrial green dock beetles *Gastrophysa viridula* was found to attach to surfaces underwater by using such an air bubble. Their naturally hydrophobic tarsal hairs trap the bubble around the pads when being submerged underwater, which de-wets the surface on contact. It has been hypothesised that a combination of capillary forces due the air bubble and hair secretions within the de-wetted area results in its adhesion underwater. However, it remains unclear if an air bubble is necessary for adhesion and what, if any, contribution it has to adhesion. The oily tarsal adhesive fluid found in insects alone might be sufficient in creating the necessary capillary adhesion even without a bubble, given that the fluid remains on the hair tips when submerged. I will investigate this particular question in more detail in Chapter-3 of this dissertation.

1.3.3. Biomechanics of adhesion

Among the various designs of adhesive organs that I have discussed so far, a particularly fascinating case, which would also be a focus of my dissertation, is that of the hairy adhesive pads. Over the past two decades, an extensive study of this design seen in different animals have improved our understanding of its underlying biomechanical principles. In fact, the hairy pad design has also inspired the fabrication of artificial adhesives that have applications in bio-inspired climbing robots, pick-and-place operations and reusable adhesives[4]. So how does the hairy design improve the adhesion function? Firstly, an array of setae can bend and conform quite well to rough surfaces, as mentioned earlier. Secondly, they are more resilient to surface defects, since any loss of contact initiated by crack propagation is contained with the corresponding setal contact, and thus offers a much reliable adhesion. Thirdly, the setae in animals usually occur in different geometries that are typically asymmetric. For example, the setae of beetles can be discoidal, spatula shaped or pointed tips that are distributed throughout the pad depending on sex or species[14]. The setal geometry can significantly influence adhesion. Single seta force measurements had revealed that discoidal shaped seta show larger pull-off forces than spatula shaped or pointed setae[15]. In some cases such as in spiders or geckos, the setae can branch into even smaller fibrillar units. Such specific geometric design helps to not only enhance adhesion, but also allows the animal to modulate its adhesion during locomotion. Lastly, the hairy pad design seems to have also a self-cleaning property, making its adhesion resilient to dirt after re-

peated contacts during locomotion. The exact mechanism of this property is not entirely understood[35].

Arzt et. al.[3] pointed out a general scaling law that exists in the natural design of hairy pads seen across a range of species. By comparing the number density of the setal structures against the body mass (Figure 1.6), they showed that heavier the animal, denser is the setal array. This indicates that having a larger number of contact points per unit area (N) is more adhesive than having fewer contacts within the same area of a pad. This effect is generally termed as 'contact splitting'. Contact splitting effect can be explained by assuming a JKR contact (sphere to plane) between the setal tip and surface (equation 1.8). If the setal contact radius scales linearly with the setal diameter, then it can be shown that the net adhesion force of the array is proportional to $\sqrt{N}$, i.e. adhesion can improved by splitting a contact into smaller sub-contacts which highlights the design advantage of a hairy adhesive pad.

An energetic argument could also illustrate the superior adhesion of a hairy pad. The energy required to separate a pad from the surface is termed as *work of adhesion* (W_{adh}). During detachment, the elastic energy stored in the hair is dissipated, which would increase W_{adh} and thus enhance adhesion[53,77]. The size of the individual hairs is also an important parameter since it controls their resistance to contact defects. Based on a *cohesive zone model*, Hui et. al.[50] had identified two regimes of single hair detachment: 1) a *flaw sensitive* regime, where, for large hair radius, contact failure occurs due to crack propagation, initiated by a stress singularity at the edge of the hair, leading to low pull off stress; 2) a *flaw insensitive* regime, where, for small hair radius, the contact interface fails simultaneously, leading to high pull off stress.

A natural question that arises in the context of animal adhesion is: how do they effectively control their adhesion? Control of adhesion is a crucial part of the whole picture, without which the animal would be forever stuck to the same spot, essentially turning their 'superpower' into a liability! So, how do animals reversibly adhere to surfaces? Tian et. al.[90] had shown that the spatula-shaped setal tips of a gecko's toe allows it to modulate adhesion up to three orders of magnitude by laterally sliding and controlling the pulling angle to reorient the contacting setae. Here, the detachment of an individual seta was modelled based on Kendall's peeling theory[32,59], which predicts low adhesion at high peeling angles. Due to the

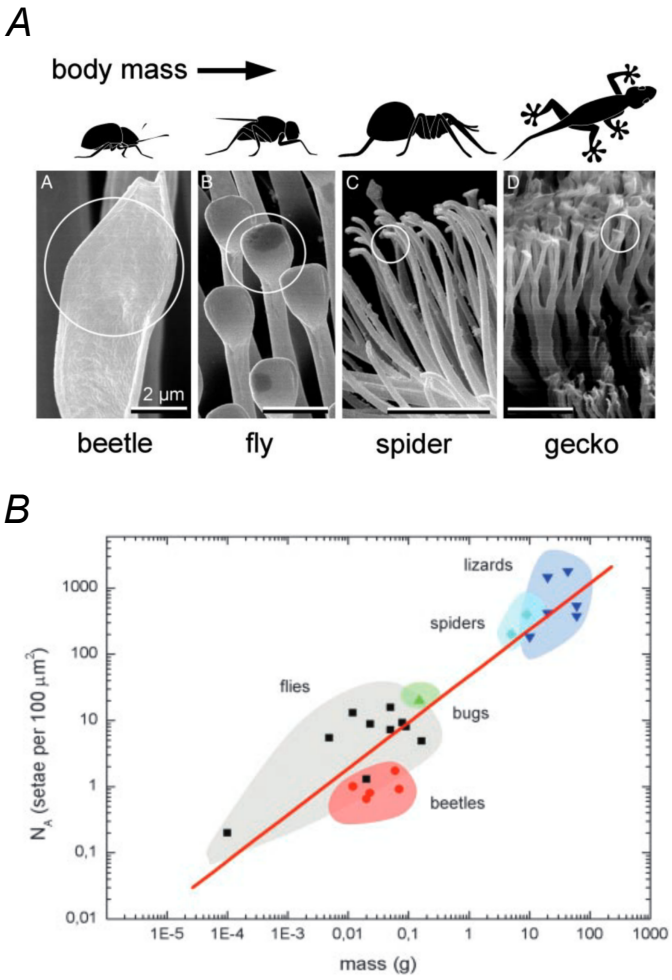

Figure 1.6.: A) Hairy adhesive pads of various animals, where the smaller sizes are seen for larger animals. B) The general scaling law of the number density of the setal array relative to the animal mass[3]

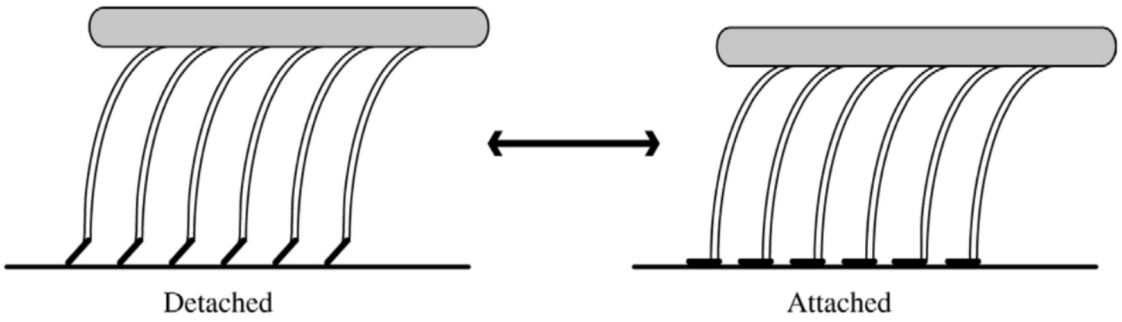

Figure 1.7.: The curved shape of the setae allow them to easily attach and detach to a surface[35]

asymmetric spatula-like shape of the setae, pulling the leg towards the gecko's body increases its setal contact area, while pushing it away from the body minimises its contact area. In this manner, the gecko can control its leg by simply incorporating a lateral shearing leg manoeuvre into its walking style on every step. Federle[35] has further argued that the curved shape of the individual seta can also help the pad to stay attached when pulled proximally and easily detached by elastic recoil when pushed distally (Figure 1.7). In summary, a low detachment force of a hairy adhesive pad can be achieved either by increasing the stress concentration by peeling the pad at high angles, or by laterally shearing the pad before pull-off, which requires the hairs to have an asymmetric geometry or curvature. The peeling strategy is also employed by insects having smooth adhesive pads, such as ants or stick insects, to easily detach their legs during locomotion.

2. Methods

In this chapter, I will describe some of techniques which were central to my research work. First, we will go through the design of a customised adhesion measurement setup which was essential for my experiments with ladybug beetles. Since this setup was developed in-house, we will look into it in detail so that it can serve as a reference for a prospective reader who would be interested to rebuild it from scratch in order to reproduce my results. Next, I will briefly summarise the working principle of Atomic Force Microscopy, which I used in Chapter 4 to develop a new method for surface tension characterisation. Finally, I introduce a simulation tool which was instrumental in the theoretical calculation of capillary force for the different scenarios involved in my research work from Chapter 3 and 4. Some of the other methods which were used to supplement my research such as macroscopic contact angle and surface tension measurements, scanning electron microscopy, and Python scripts used to automate certain data analysis calculations are described later in the corresponding chapters.

2.1. Adhesion measurement setup

A customised force measurement setup was built in order to enable my study of the adhesive properties of a ladybug's foot. In this regard, it was necessary for the setup to have some specific features:

1. A force sensor which can precisely measure vertical pull-off force the insect's leg, which are expected to be in the range of 50 to 1500 µN.
2. Optical microscopes which would help visualise the contact of the leg with a substrate. The microscope should have sufficient resolution in order to visualise a single adhesive pad of the insect, which is of the order of 200 µm, as well as the individual setae, which is of the order of 5-10 µm.

3. An automated positioning system that could allow pull-off experiments to be performed on the insect leg under specific speeds. The system should allow controlled motion in both vertical and lateral directions.
4. A synchronised control and acquisition of all the relevant data from the above three features.
5. Suitable holders such that the force measurements can be performed on live insects against different substrates in both air and underwater conditions.

Thus, a number of components needed to be integrated into a single setup to enable my adhesion experiments. A simplified schematic of the designed setup is shown in Figure 2.1. Let us go through each of them one by one.

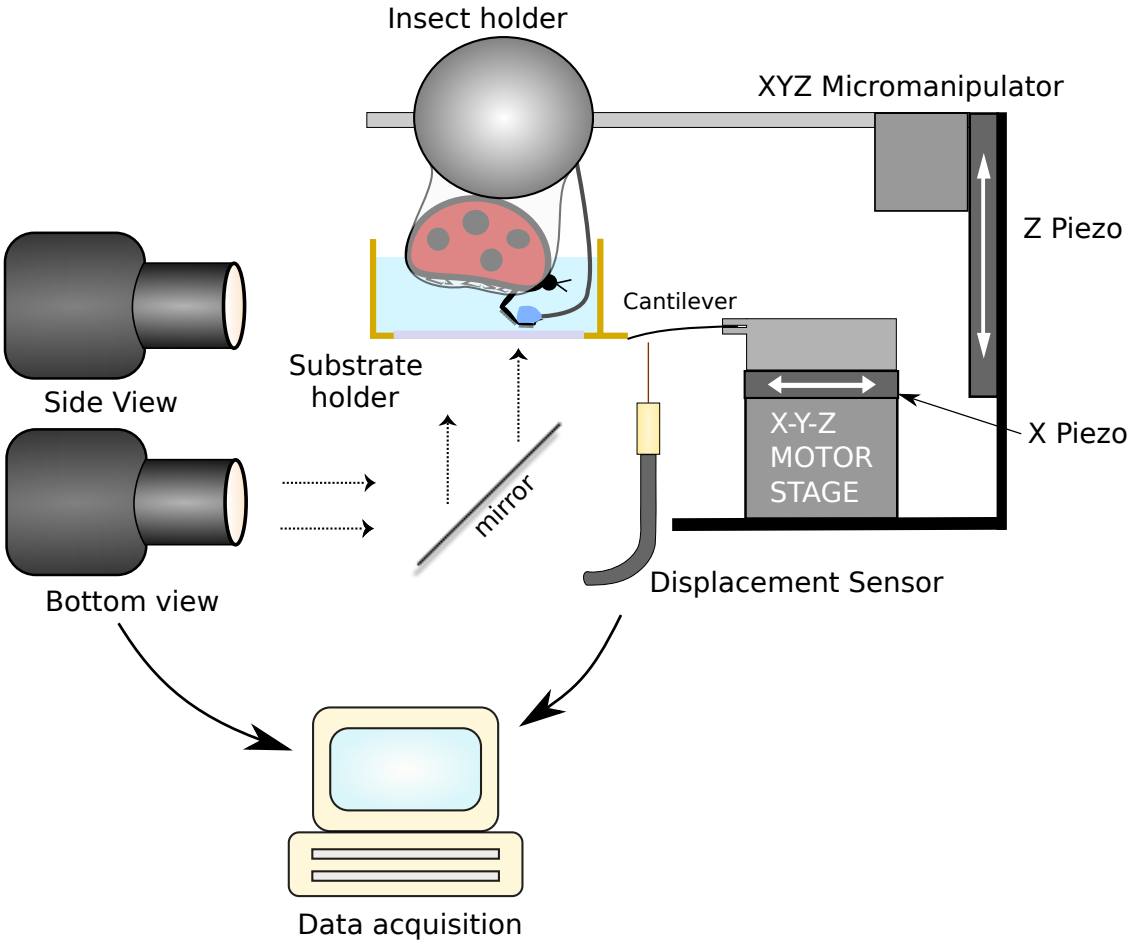

Figure 2.1.: Schematic of the custom made adhesion measurement setup

2.1.1. Force sensor

Typically force measurements are performed using commercially available strain gauge based load cells, which are available for a range of sensitivity and resolution. However, these load cells have several limitations. Firstly, they have a fixed force resolution which can not be easily altered as per necessity. Secondly, they are designed to be used within a specific load capacity. A trade-off thus exists where, lower the force resolution, lower will be the load capacity. Having a high capacity can be quite useful, since it would allow us mount additional sample holders to the load cell. Since I want to measure very small forces of the order of 100 µN in underwater conditions, it puts a significant limitation on the design of a sample holder that can hold a small pool of water.

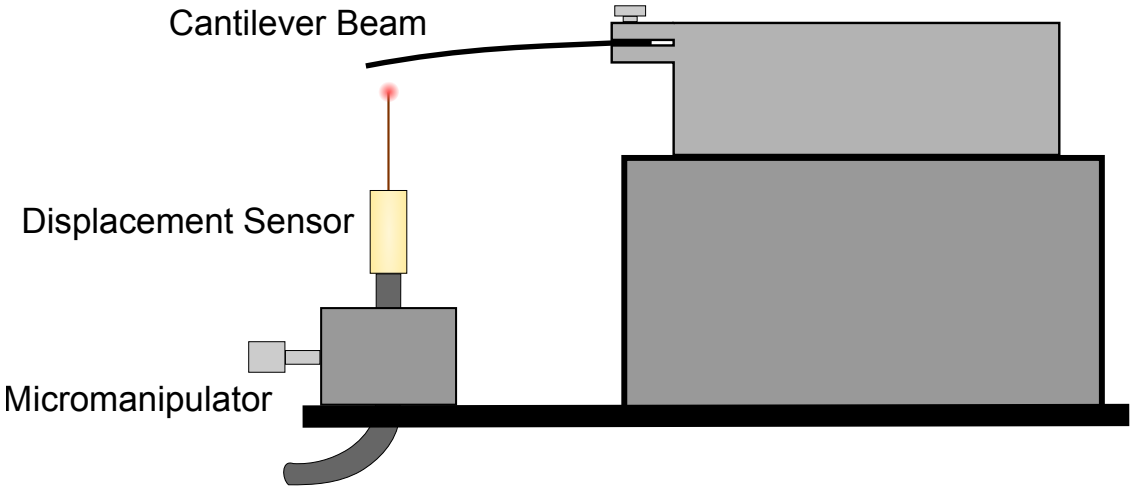

Figure 2.2.: Design of the force sensor

To overcome these limitations, I designed a force sensor by combining a metal cantilever with an optical displacement sensor (Figure 2.2). A force applied at the end of the cantilever would slightly bend it relative to its initial state. This deflection is measured by a displacement sensor (*Philtec D20, PHILTEC, Inc. USA*), positioned under the free end of the cantilever. The sensor emits a beam of infrared laser (λ=850 nm) and detects the light that is reflected back. The intensity of the reflected light, measured as a voltage, is correlated to the distance between the tip and the reflection spot. The typical response curve of the sensor (Figure 2.3) consists of two regimes: the *near-side* regime at small tip-surface distances, which shows about 10 times more measurement sensitivity compared to the *far-side* regime seen at large tip-sample distances. The sensor can thus be positioned to

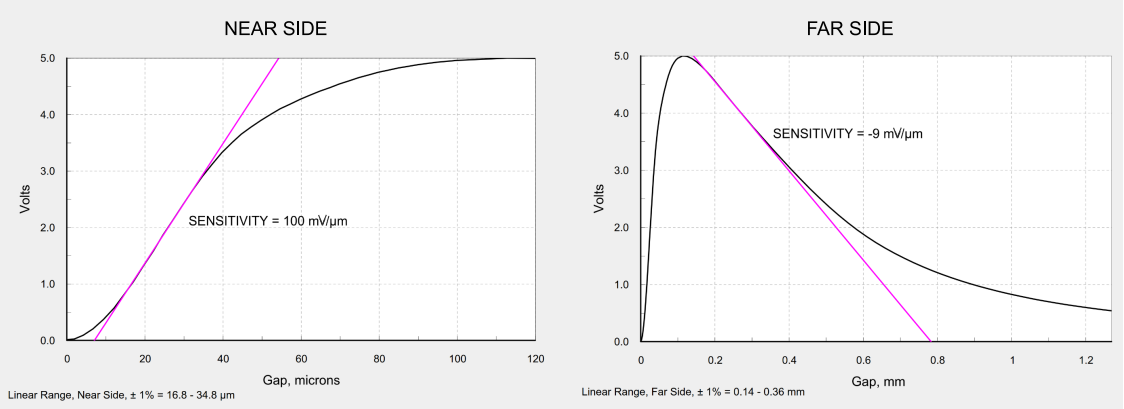

Figure 2.3.: Response curve of the displacement sensor (*Philtec D20*), showing the two regimes (*philtec.com*)

an appropriate regime depending on how much force sensitivity is necessary. A micro-manipulator Z-stage was used to precisely position the sensor tip relative to the cantilever. The sensor's signal-to-noise ratio was improved by gluing a small piece of gold-coated glass cover slide at the cantilever end, which consequently also improves the measurement resolution. Using the measured deflection of the cantilever, the force acting on its end can be calculated based on its spring constant value.

The spring constant could in principle be obtained from the dimensions and mass of the cantilever. However, a more accurate method to get this value is by performing a experimental calibration procedure using known weights. The method followed is as follows. First, the cantilever response curve (voltage vs distance) was measured by deflecting it with a pin that is moved precisely using a piezo nano-positioning stage (P-629.1CD, *Physik Instrumente, Germany*, resolution = 3 nm). Using the obtained response curve as a reference, the sensor tip was then positioned such that the voltage value lies approximately in the centre of the *near-side* or the *far-side* regime. A polynomial fitting was performed for the chosen regime so as to easily calculate the distance from an arbitrary voltage measurement in that regime. Then, an object of known weight was placed on the cantilever end and the resultant change in voltage value was recorded. The voltage change was translated into distance units using the above mentioned polynomial fit. The actual weight of the object was independently measured using a micro-balance and converted to force units (newtons). The above process was repeated for five different calibration weights, whose values lie within the range of the desired forces to be measured. A

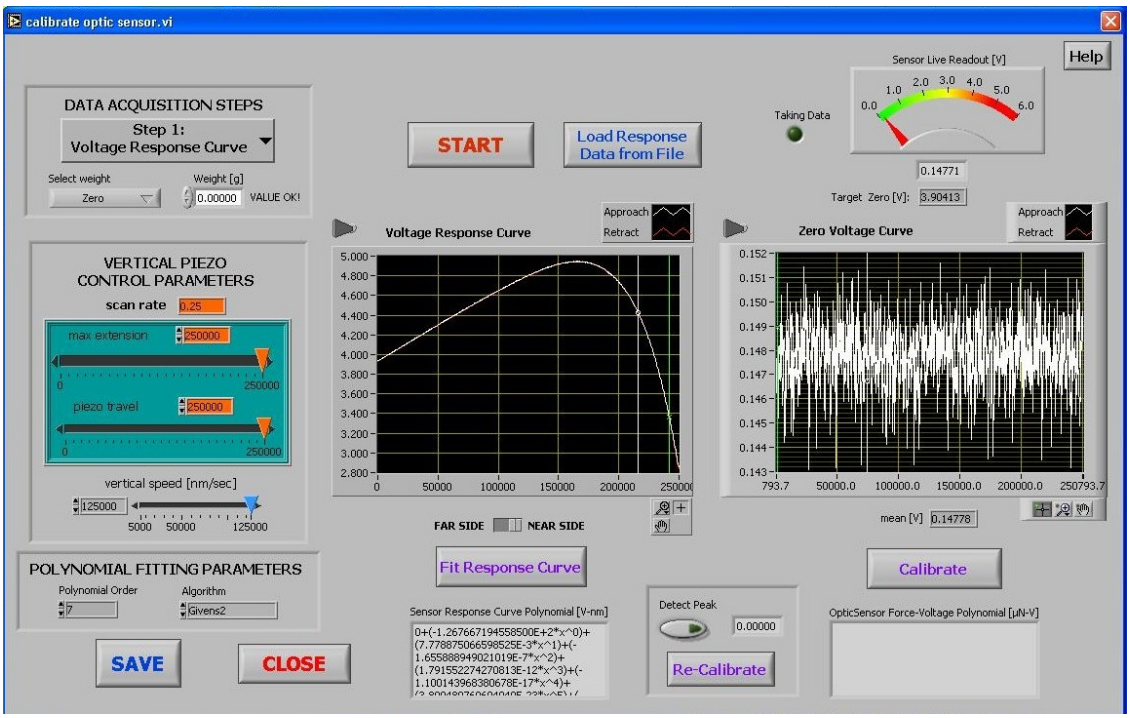

Figure 2.4.: LABVIEW program interface developed to calibrate the force sensor

linear fit was then performed for the five points of force-displacement data. The fitted linear equation gives us the force value for any value of cantilever deflection in the chosen regime, where the slope of the fitted equation is the cantilever spring constant. The entire calibration process was automated using a custom LABVIEW program (Figure 2.4).

The above described custom force sensor design allows us to easily overcome the previously mentioned limitations of a conventional load sensor. Here, the sensitivity of the force sensor is determined by two factors: 1) the chosen dimensions/material of the cantilever beam and 2) the operating regime of the displacement sensor. Both of these can be easily adjusted in order to measure a specific range of forces. Since the measurement is primarily performed optically without any sensitive parts in contact, the designed force sensor can be operated under high load capacity while maintaining its high force sensitivity. This allows one to glue relatively heavy sample holders to the end of the cantilever. Even though the holder would bend the cantilever significantly, the displacement sensor can be easily positioned below it to track its deflection relative to its initially bent state and thus measure forces with high sensitivity.

2.1.2. Optical components

An adhesion measurement involves bringing the insect's foot in contact with a particular surface and then subsequently retract it away from the surface until it loses contact. Since this measurement needs to be performed also in underwater conditions, a practical solution would be to bring the insect leg from the top and onto a substrate below that is immersed underwater. The contact process of the foot with the substrate can then be observed either from the side or from below, provided that the substrate is optically transparent. I used two microscopes equipped with cameras to monitor the contact process from both directions. A coaxial illuminated tube microscope (*Navitar, USA*) with 2× objective and a stereo-microscope with 1× objective (*Wild Heerbrugg, Switzerland*) fit with digital video cameras (*Blackfly S, FLIR, USA*, 2448 × 2048 px; *Basler ace U, Germany*, 1280 × 1024 px) were used to record the sample contact with the substrate from ventral and side views respectively. Here, a 45° mirror was used together with the tube microscope to enable ventral imaging of the substrate (Figure 2.5). A goniometer was used to adjust the substrate and mirror alignment with the ventral view optics to achieve total internal reflection. This helped me to obtain a good image contrast, where, the areas that make contact with the substrate could be identified by the darker intensity spots, where as, no contact was indicated by bright regions. Such an imaging mode was particularly useful to visualise the underwater contact, since any trapped bubble can be easily identified by its bright region in comparison to a relatively dark background resulting from the surrounding water.

2.1.3. Positioning stages

The insect's leg needs to moved in a controlled fashion during the adhesion measurement. Since the experiments will be performed on live insects, the leg needs to first be properly restrained in a fixed orientation. Then, the leg needs to be brought into contact with a flat surface and retracted vertically back up. The vertical motion here is performed by moving the entire insect with a Z-piezo stage, same as the one used to calibrate the force sensor, as mentioned in the previous section. A second X-piezo stage is also used in order to enable precise lateral movement of the substrate. This lateral motion control is essential in order to improve the contact of the leg with the substrate. The piezo stages allow precise movements without

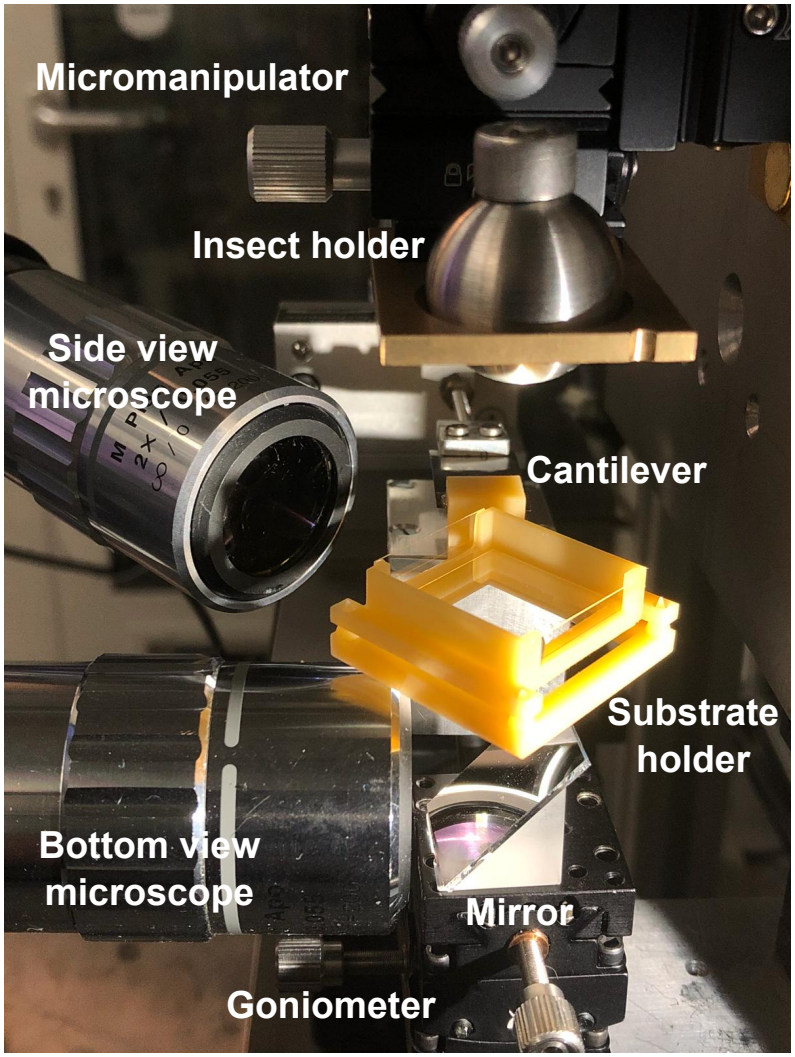

Figure 2.5.: Photograph of the setup, showing the microscopes used for side and bottom view imaging as well as the holders.

causing vibrations, but however have a very short travel range, less than a millimetre. Thus, the setup also used an XYZ motor stage (*OWIS GmbH, Germany*) in order to initially bring the the substrate and the insect foot in close proximity to one another. Once this initial position is adjusted, the setup would switch to using piezo stages in order to bring the insect's foot into contact with the substrate and thus perform force measurements vibration-free. The entire setup was also mounted on an active vibration isolation platform (*TS-140, Table Stable, Switzerland*) and under a closed hood to minimise any external mechanical noise.

2.1.4. Data acquisition and control

In order to perform an adhesion measurement successfully, the force sensor, the two microscope cameras and the two piezo stages need to be simultaneously controlled. This can be quite a complicated task if attempted manually by a single PhD student. So, I designed a custom LABVIEW program to completely automate the measurement process (Figure 2.6). An I/O board (*PCI-6035E, National Instruments*) connected to a computer was used to 1) move the piezo stage by send the necessary input voltage values, 2) read voltage value output from the displacement sensor, and 3) send a train of trigger pulse signal wave to the cameras in order to capture image frames at the specified rate. Here, the cameras were configured to capture an image frame only when it received a trigger signal. The above three functions were synchronised using by keeping all the input and output data in the buffer memory and using a second trigger pulse to initiate the control and acquisition. Here, the piezo stage was configured to respond to the rising edge of the trigger pulse, where as, the displacement sensor and cameras were configured to begin acquisition at falling edge of the trigger pulse. This was because the piezo elements responds to an input voltage only after a slight delay of 13 ms, which was measured using an oscilloscope. For perfect synchronisation between all components, this piezo delay can be accounted by setting the trigger pulse time period in its high state to be equal to the delay time. In this way, the force sensor and the cameras can be triggered to start data acquisition exactly at the moment when the piezo starts to move.

The LABVIEW program can be used to specifically design the adhesion measurement protocol. The Z and X piezo stages can be programmed to move, either sequentially or simultaneously, at any given input speed. An intermediate pause in

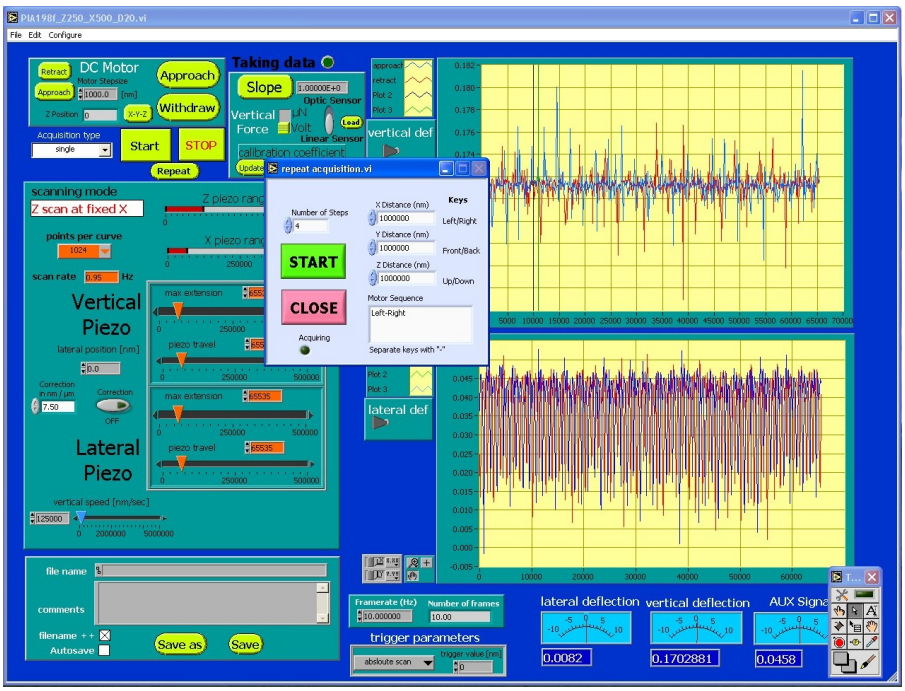

Figure 2.6.: LABVIEW program interface developed to control the adhesion setup and capture data

the motion can also be incorporated into this routine. Further, the program also make it possible to automatically repeat the measurement protocol on a new spot of the substrate. This was done by repositioning the substrate relative to the insect foot after an adhesion experiment by controlling the XYZ motor stage based on a specified input routine (direction sequence: Front/Back/Left/Right and motion distance).

2.1.5. Sample holders

Customised holders were needed to be designed in order to easily load the insect and the substrate into the setup for adhesion measurements. The insect was restrained onto a spherical steel ball by temporarily gluing its back onto the ball. A plate screwed to a XYZ micromanipulator was used to support the steel ball through an appropriately sized hole. The micromanipulator was in turn attached to the Z-piezo stage using magnets so that the initial position of the insect holder can be roughly adjusted manually. The advantage of using a spherical ball was so that the insect leg can be oriented almost parallel to the substrate below by rotating the ball through the hole. This was important so as to ensure that the adhesive

pad of the leg makes a nearly complete contact with the substrate during adhesion measurement.

For the case of the substrate holder, there were a couple of challenges. Firstly, the holder should be able to allow optical visualisation from the bottom and from the side. Secondly, the holder should hold a pool of water in order to perform underwater measurement on the substrate. Lastly, the holder should be easily interchangeable such that a new surface can be quickly loaded onto the setup. A custom 3D printed substrate holder was thus designed in order to solve these challenges (Figure 2.7). The substrate holder comprises of two pieces. The bottom piece is permanently glued to the end of the cantilever. The four pins on this piece are used to mechanically lock into the cavities located underneath the top piece. A standard glass cover slip (20 $\times$ 20 mm) was glued to the bottom hollow face of the top piece. Small pieces of glass cover slides were also glued to the side windows of this piece. This allowed me to capture the contact process both from ventral and side views (see setup image in Figure 2.5). Multiple top pieces of identical shape were printed and substrates of interest were glued to them. Since the top piece is only mechanically locked, it can be quickly removed from the bottom piece and in this manner, the substrate can be changed for subsequent measurements easily without the removing the insect from the top or going through any painstaking disassembly procedure after each measurement.

2.2. Atomic force microscopy

The working principle of Atomic Force Microscopy (AFM) shares many similarities with the adhesion measurement setup that I described in the previous section. The main difference is that forces involved in an AFM is at around 3 orders of magnitudes smaller, in the range of nanonewtons. Other than that, the basic design of the AFM is quite similar. It typically consists of a tiny Silicon cantilever probe with a sharp tip on its end, fabricated using nanolithographic techniques. The sharp tip of the cantilever interacts with a sample surface causing it to deflect. This deflection is measured optically by shining a laser spot on the back of the cantilever and tracking the reflected beam falling onto a four quadrant photodiode. The position of the cantilever relative to sample surface is manipulated using piezo motion stages (Figure 2.8).

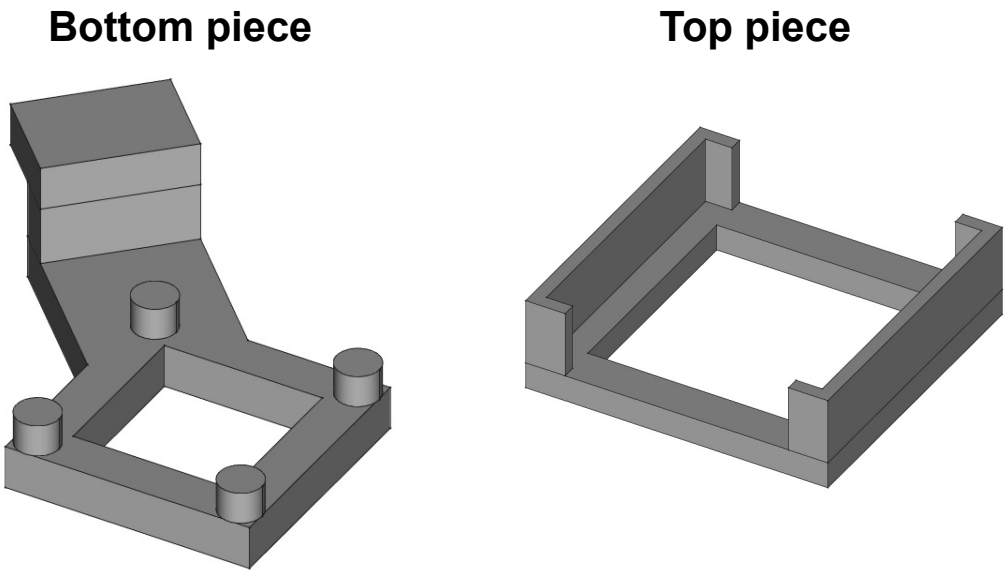

Figure 2.7.: Design model of the substrate holder used for 3D printing

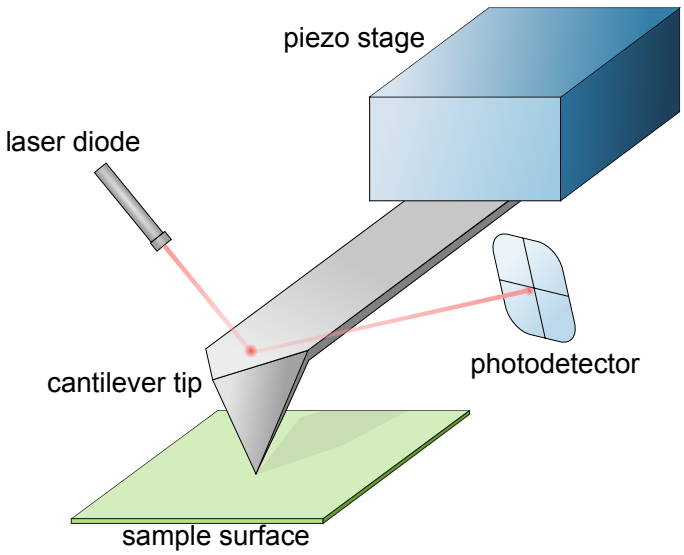

Figure 2.8.: Schematic of a general AFM setup

Typically AFM is used to obtain sub micrometer scale topographic images of surfaces. This is done by scanning the cantilever tip over a particular region of the surface line by line. The deflection of the cantilever at each point of the scanned region can be correlated to the topographic changes present on the surface. Thus, very high resolution topographic images can be obtained. There are several modes in which the AFM can be operated for imaging. A common method is the so called 'tapping mode' or 'intermittent contact mode'. Here, the cantilever is oscillated close to its resonance frequency with the help of a vibrating piezo element driven at a fixed amplitude and frequency. The amplitude of the cantilever oscillation would change when it interacts with a surface. But an electronic feedback loop is used to adjust the cantilever's vertical position relative to the surface such that its oscillation amplitude always remains constant during the image scan. The adjusted position values can be used to generate a topographic height image of the scanned surface. Another common method for imaging is the 'contact mode'. In this case, the cantilever tip is in contact with the surface. The tip is laterally moved while maintaining contact under a fixed load, i.e. the cantilever deflection is kept constant similar to before using a feedback loop by changing the z-position of the piezo stage. The position values will once again give us the height image of the sample. Apart from imaging, AFM can also be operated under 'force spectroscopy' mode to obtain force-distance curves at a specific point of the sample surface. This can be used to either measure adhesion or mechanical properties of the sample.

2.3. Surface Evolver

Surface Evolver is a free simulation tool developed by Kenneth A. Brakke[12] in order to solve for the equilibrium shape of liquid interfaces under a given condition. Liquid of a defined constant volume is initially assumed to be some arbitrary polyhedral shape. Appropriate boundary conditions are defined corresponding to each kind of interface or contact line that it could possibly make with the surrounding phases. Each interface is then assigned a corresponding interfacial energy value (which is identical to the interfacial tension). For the case of liquid-solid interfaces, a priori knowledge of contact angle could be used to calculate the interfacial energy with the help of Young-Dupré equation (equation 1.5). Any external force fields acting on the liquid, such as gravity, may also be additionally defined. Under these conditions, the equilibrium shape of the liquid interface is obtained by minimising the total

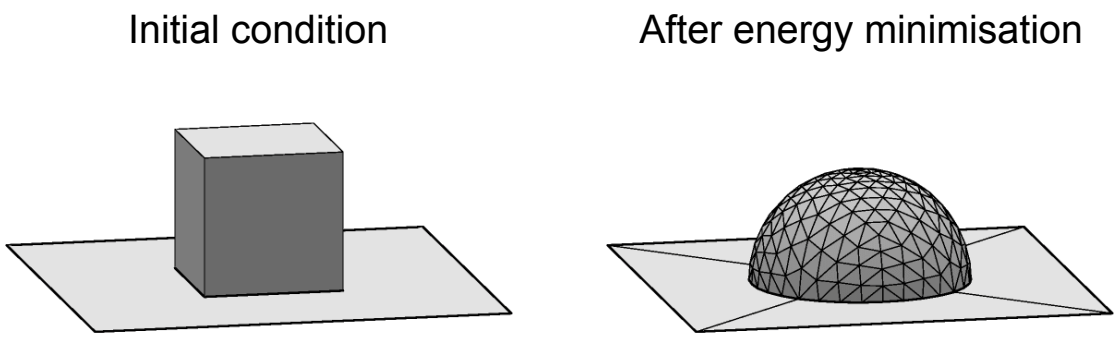

Figure 2.9.: Simulation snapshots of the initial and final geometry of a liquid drop laying on a flat surface, generated using Surface Evolver. Here, a liquid contact angle = 90° was assumed to calculate the liquid-surface interfacial energy.

energy of the system using the gradient descent method. A classic example of this software in action is to simulate the shape of a liquid drop laying on a flat surface (Figure 2.9). Here one would start with an initial cubic shape of a defined volume and assign appropriate surface energy values for each interface. On executing the energy minimisation steps, the cube transforms into a spherical cap shape, since for a given volume, a spherical geometry has the lowest surface area, and thus the minimum surface energy.

Just like most simulation tools, an appropriate routine needs to be written to effectively solve the minimisation problem without creating any singularities. A general procedure is to subdivide the interface into smaller triangular elements, perform energy minimisation for a few iterations, then repeat the refinement and minimisation over and over until the total energy of the system stagnates to a constant minimum value. Some additional mathematical tricks such as equiangulation or vertex averaging can be incorporated into the solution routine to avoid any of the facets to diverge towards an incorrect state.

In this dissertation, I use Surface Evolver primarily as a tool to calculate the capillary force between two surfaces resulting from an intermediate liquid bridge. This can be particularly useful if any of the contacting surfaces have an unusual geometry or boundary condition such as contact line pinning, where an analytical derivation of capillary force will not be trivial. In such cases, Surface Evolver can be used. First, the equilibrium shape of the liquid bridge under given boundary conditions is obtained. From the equilibrium shape, the capillary force can be easily calculated from equation 1.4.

In order to setup the simulation for a given problem, first we need to start with creating a data file. This file contains all the necessary information to initialise the problem and define all the necessary constraints and boundary conditions to be included for the energy minimisation. An important point to note here is that Surface Evolver is not at 3D software. While the liquid shapes obtained are indeed three dimensional, the software is only solving for two dimensional finite elements which together define a 3D interface. In many cases, it is also possible to completely eliminate a interface by replacing it with its contact line. This can be done for solid-liquid interfaces since the shape of the interface in this case does not change, but rather only the interfacial area changes. Such tricks to reduce the dimension can significantly save computation time but it also slightly complicates some of the initial definitions of the system. In order to do this correctly, the higher dimensional information needs to be transformed into an appropriate lower dimensional form by using Stoke's theorem or Divergence theorem, such that the effect of the higher dimensional terms are appropriately accounted for and thus be safely eliminated. This is especially important when one of the interfaces is in contact with a non-planar solid geometry, for example, where the corresponding boundary conditions needs to be defined properly such that the interfacial energies and liquid volume terms are corrected for. A detailed explanation on how to go about this as well as some common strategies to make such transformations can be found in the software's user guide.

3. Underwater adhesion in ladybug beetles

3.1. Summary

In 2012, a study by Hosoda and Gorb[47] reported that a terrestrial beetle can even adhere and walk underwater. The naturally hydrophobic hairs trap an air bubble around the pads, allowing the hairs to make contact to the substrate like in air. However, it remained unclear to what extent such an air bubble is necessary for underwater adhesion. Hosoda et. al. hypothesised in their study that the air bubble itself might help enhance the insect's underwater adhesion due to its capillary force. In this chapter, I will test this hypothesis. We know that ladybug beetles use hairy adhesive pads to stick to surfaces, where their hairy tips also secrete an oily fluid. To investigate the role of the trapped bubble, first, I measured the adhesive forces in individual legs of live but constrained ladybug beetles underwater in the presence and absence of a trapped bubble. I performed these tests on both a hydrophilic and hydrophobic surface since surface energy of the substrate can influence adhesion. Here, I used the male ladybug beetle *Coccinella septempunctata* as an animal model for my experiments, since they possess adhesive pads having mostly flat discoidal tipped hairs, which allow them to show superior adhesion on hard surfaces compared to females[44]. Second, I developed a simple theoretical model considering capillary forces to predict the net adhesion force of a hairy pad both in the presence and absence of a trapped bubble. Here, the bubble's individual contribution to the insect's adhesion was estimated. Using both my experimental and modelling results, I will show that the trapped air bubble has little to no impact on the beetle's underwater adhesion. Rather, it is the oily secretion of its pads that enable them to stick underwater due to capillary forces.

This chapter's content is adapted from my published research article[87]. The repor-

ted adhesion experiments, substrate preparation, theoretical simulations in Surface Evolver as well as related analysis were all performed by myself alone under the guidance of [redacted]. A crucial part of the experiments on ladybug beetles involved building a customised adhesion measurement setup (described in Chapter 2.1). This setup was designed and assembled with the combined effort of [redacted] and myself, together with the support of the mechanical workshop of the MPIP.

3.2. Experimental

Normal adhesion force measurements on a restrained leg in a live beetle were performed. I focused my study only on a single tarsal adhesive pad of the leg by carefully immobilizing it (described later) to prevent any dynamic influence of its claws or other tarsomeres/legs, which might otherwise exist under the beetle's natural walking conditions, influencing its adhesion. I characterised adhesion by the pull-off force during detachment, tested on smooth untreated and fluorinated glass surfaces representing hydrophilic and hydrophobic substrates respectively. When no water was present, I labelled the mode of contact as "*in air*". Underwater, measurements were done both in the presence and absence of a trapped air bubble ("*underwater: bubble*" and "*underwater: no bubble*", respectively) to investigate the air bubble's role in underwater adhesion. Adhesion forces for each of the labelled contact modes were compared for both substrates.

3.2.1. Materials and Methods

3.2.1.1. Insect preparation

Adult seven-spotted male ladybug beetles (*Coccinella septempuctata*) were purchased from Katz Biotech (Baruth, Germany). The beetles were housed in a plastic box filled with leaves, twigs and stones at room temperature and 60-80% relative humidity with natural daylight. They were fed with raisins, honey and water *ad libitum*. The beetles on average weighed 34 ± 4 mg and were used within three weeks of being housed under above conditions.

An individual beetle was first carefully anaesthetised using small amounts of CO_2 sublimating from a piece of dry ice and then glued with a small dollop of epoxy glue on its elytra to the underside of a heavy steel ball. The ball was held in a bracket which allowed free rotational movement of the ball in each direction, thus helping to align the suspended beetle over the substrate (see Fig. 3.1). The bracket with the ball and the beetle could be further positioned by manual micro-manipulators in all three axes before the experiments. The front left leg was carefully fixed at its tibia to a piece of soft solder wire coming off the steel ball using Blu Tack (Bostik Ltd., U.K.), allowing us to further align the leg to the substrate. Each leg of a male ladybug beetle has two hairy adhesive pads. For the test, I only allowed the distal pad to make a good contact with the substrate thus minimising partial or bad contact of the proximal pad. The distal pad was thus restrained by fixing its dorsal side to the wire using Blu Tack. The claws on the leg were also fixed to the wire using epoxy glue to prevent any further movement and to prevent the claws from touching the substrate (Fig. 3.1 top-left inset). Care was taken to ensure the glue does not contaminate the rest of the tarsomeres. A small piece of non-sticky Teflon tape helped to keep the other legs tucked close to the body and avoided any interference during the adhesion test. After the measurements, the beetle was freed by carefully removing the epoxy glue and Blu Tack from its claws and tibia using a pair of tweezers without harming it and set free.

3.2.1.2. Adhesion test

Adhesion measurements were performed on a custom force measurement setup, as was described in detail in Chapter 2 (Figure 3.1). I'll briefly summarise the setup design here. A fibre optic displacement sensor (*Philtec D20, PHILTEC, Inc. USA*) together with a steel bending beam (spring constant = 68.1 N m^{-1}) constituted the vertical force sensor. Beam deflection was calibrated using 4 different known weights (range: 2 - 90 mg) to get the corresponding force (resolution = 5 µN). A 3D printed substrate holder (22 × 22 × 8 mm) was glued to the end of the bending beam. The holder was designed to enable switching from one substrate to another without removing any glue. It also had transparent side walls which allowed us to fill it with water for the underwater experiments as well as observe the contact. The force sensor was mounted on a stage consisting of a X-piezo element, used for precise lateral movements (step size = 75 nm). Additionally, a separate Z-

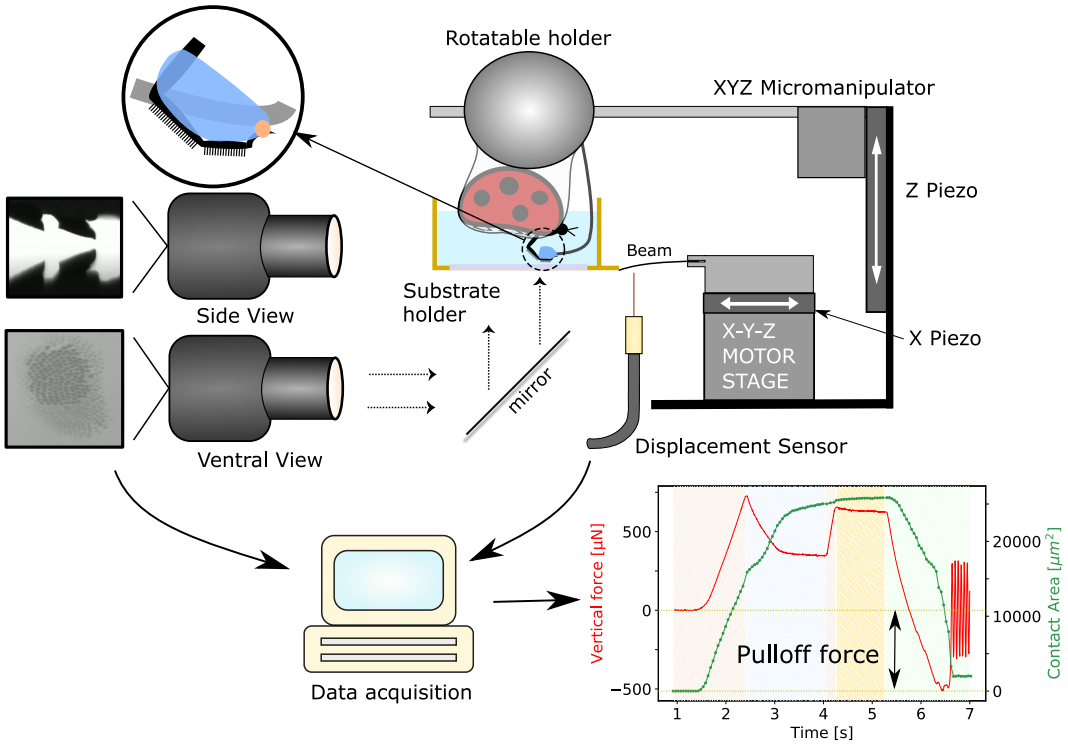

Figure 3.1.: Adhesion test setup (see text for details). Top-left inset shows a magnified cartoon of the beetle's leg constrained to a solder wire (grey) using Blu Tack (blue) and epoxy glue (orange). The recorded force data and contact area of a distal pad are shown in the bottom-right plot, in which, the shaded regions from left to right represent the distinct movement sequence: approach, lateral pull, approach, pause and retract, respectively. Negative force values represent attraction and the minimum force peak during the final retraction step is the adhesion force used for further analysis.

piezo element (P-629.1CD, *Physik Instrumente, Germany*, resolution = 3 nm), fixed upright, was used for vertical up-down motion, bringing the insect in contact with the substrate from the top. Coarse movements of the bottom stage were done using the XYZ motors (*OWIS GmbH, Germany*). A coaxial illuminated tube microscope (*Navitar, USA*) with 2× objective and a stereo-microscope with 1× objective (*Wild Heerbrugg, Switzerland*) fit with digital video cameras (*Blackfly S, FLIR, USA*, 2448 × 2048 px; *Basler ace U, Germany*, 1280 × 1024 px) were used to record the sample contact with the substrate from ventral and side views respectively. Pad contact area was visualised through the substrate under reflection mode with the help of co-axial illumination. A goniometer was used to adjust the substrate alignment with the ventral view optics to achieve total internal reflection. The data acquisition from the force sensor and cameras, together with the appropriate piezo motion steps were synchronised using a custom LABVIEW (*National Instruments, USA*) program. Force data was acquired at a sample rate of 984 Hz, averaged to 512 points per motion step for smoothing. Videos were recorded at 20 frames per second.

The vertical and lateral piezos were used simultaneously to perform approach-retract adhesion tests with the substrate to measure the pull-off force. However, instead of a simple down-up motion, an additional 100 µm lateral sliding motion in the proximal direction was introduced after the leg made contact, to ensure most of the hair tips align well with the substrate[14]. A further 10 µm compression step (approach) set all hairs in slight compression which helped maximize the hair contact with the surface. Next, a short pause (1 s) minimized any viscoelastic effects before finally retracting the leg away from the substrate. All approach, retract and lateral slide motion were done at a speed of 62.5 µm s^{-1}. Ventral view video recordings were used for contact area extraction while the side view imaging was used to aid in orienting the pad with the substrate before a test.

For underwater experiments, 1 ml Milli-Q water was pipetted into the substrate holder (roughly 3 mm water level). The beetle (roughly 5 mm long) was then partially submerged to allow underwater contact of the pad with the substrate (immersion time $\sim$ 15 mins). In order to achieve contact without a trapped air bubble, the water was first degassed separately in a vacuum chamber at 10 mbar pressure for 3 hours and then pipetted into the holder immediately. The beetle was subsequently immersed, where, the trapped air bubble within the pad dissolves into the degassed water in less than 5 mins, as verified by the ventral view contact

image. Before the experiments, the pad was brought into contact with the clean dry surface 10 times repeatedly (same motion protocol as described above) to ensure the hairs are free of any contaminating particles.

Five force measurements were subsequently performed, each on a fresh spot of the substrate, and were averaged to avoid pseudo-replication during data analysis. Experiments were repeated with distinct male beetles for each combination of contact mode ("*in air*", "*underwater: bubble*" and "*underwater: no bubble*") and substrate chemistry (hydrophilic and hydrophobic), using 5 beetles for each combination. Thus, 30 distinct beetles were used in total. After an experiment, the beetle was marked on its elytra and released back into the box to ensure the same beetle was not used for any subsequent adhesion tests.

3.2.1.3. Data analysis

Extraction of pull-off force from force data, image processing, plotting and statistical analysis were all performed in "*Buggee*", a software tool written in Python using open-source libraries for synchronous analysis of force data and video recordings (`https://github.com/PranavSudersan/Buggee`).

For measurements in air, the pull-off force was defined as the minimum negative force during the retraction step (bottom-right plot in Figure 3.1). For underwater measurements, an additional correction was necessary. When the beetle was partially submerged underwater, the water's contact with the beetle shifted, which influenced the force readout due to surface tension and buoyancy. This effect needed to be cancelled. Therefore, a "background" force data was recorded, following the exact motion protocol as a typical adhesion test, but where the submerged beetle makes no contact with the substrate. This background data was then subtracted from a typical force curve with substrate contact, by matching the time data, to correct for the external surface tension effects ($\sim$ 50 µN) for each individual beetle. The pull-off force was subsequently calculated from the minima as before.

Data sets were compared for statistical differences using two-way ANOVA analysis, with *contact mode* and *substrate chemistry* as the categorical variables and *adhesion force* as the dependant variable. Pairwise Student t-test were done for post-hoc analysis and their corresponding p-value and Common Language Effect Size (CLES) are reported. Shapiro-Wilk tests were done for each data set to verify

a normal distribution of its residuals and Levene's test was done to check for variance homogeneity, to validate the ANOVA assumptions. Bonferroni's correction was used to account for multiple comparison between groups.

3.2.1.4. Substrate preparation

Standard 20 mm wide glass cover-slips were used as the hydrophilic substrate. Glass was wiped with isopropanol, rinsed in water and dried under nitrogen flow before use. For the hydrophobic substrate, the glass cover slip was coated with a fluorosilane via chemical vapour deposition (CVD). First, the glass was cleaned using IPA. The surface was then plasma cleaned in an oxygen plasma chamber (*Femto, Diener Electronic GmbH, Germany*) for 10 min at 120 W. Next, 0.2 ml of Trichloro(1H,1H,2H,2H-perfluorooctyl) silane (PFOTS), procured from Sigma Aldrich, was put in a sealed chamber along with the the cleaned glass. The chamber was placed under 100 mbar pressure for 10 min for the CVD process. Finally, the substrate was annealed at 150 ℃ for 3 hours. Henceforth, I refer to the hydrophilic untreated glass substrate as simply *Glass* and the hydrophobic fluorinated glass substrate as *PFOTS*.

The surface chemistry was characterised by dynamic contact angle measurements, performed with a contact angle goniometer (*OCA 35, DataPhysics Instruments GmbH, Germany*). The substrate's wetting towards a polar (Milli-Q water) and a non-polar (n-hexadecane) liquid was tested. Advancing and receding contact angles were measured for a maximum drop volume of 10 µl and with 0.5 µl s^{-1} flow rate.

3.2.2. Results

3.2.2.1. Substrate characterisation

The surface chemistry of untreated glass (hydrophilic) and PFOTS-coated glass (hydrophobic) was characterised using dynamic contact angle measurements (Table 3.1). De-gassed water showed similar contact angle values as normal water.

Table 3.1.: Dynamic contact angles measurements on the different test substrates.

Substrate	Liquid	θ_A	θ_R
Glass	Water	63±5°	20±2°
	n-Hexadecane	<10°	<10°
PFOTS	Water	122±1°	93±2°
	n-Hexadecane	88±2°	56±5°

3.2.2.2. Insect adhesion

In air, adhesion forces of the distal pad of the ladybug beetles against glass and PFOTS were similar, i.e. no significant differences were detected (Figure 3.2). In contrast, the underwater adhesion on a PFOTS surface was significantly larger than on glass ($p < 0.001$). This stronger adhesion on PFOTS was observed both in the presence and absence of a trapped bubble. In both cases, the adhesion force reached similar values as in air. In contrast, on glass, adhesion underwater was significantly reduced when compared to dry conditions, irrespective of the presence of a trapped bubble ($p \leq 0.002$). In the presence of a bubble, underwater adhesion on glass was slightly higher (CLES = 0.84, $p = 0.07$).

Apart from the three depicted contact modes, I observed an additional fourth mode which occurred in roughly 25% of my underwater experiments (excluded from above analysis) using degassed water. In this scenario, the ventral view recordings show that none of the hairs appear to contact well with either glass or PFOTS substrate, unlike the other three contact modes. This "bad contact" scenario only happened underwater and shows no adhesion with either glass or PFOTS substrate. While it was not completely clear why such a contact occurs, there can be two possible reasons. First, the hairs could get bundled due to a small air bubble trapped within them which might not have completely dissolved away in the water. The presence of this air-water meniscus could thus lead to elasto-capillary bundling of the hairs, resulting in their disorientation. Second, a thin water layer at the substrate interface might not be drained out to allow the hairs to make contact with the substrate, resulting in a loss of adhesion.

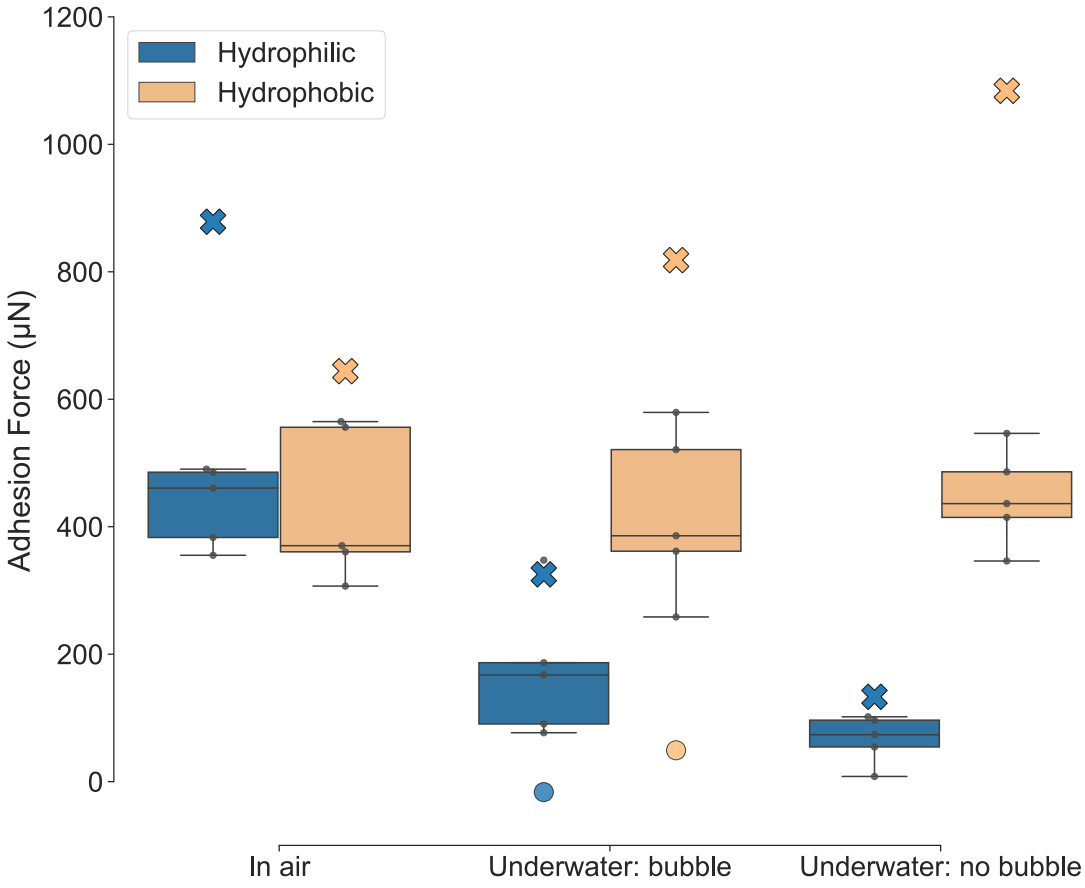

Figure 3.2.: Box-and-whisker plot showing adhesion force measurements of ladybug beetle's (*Coccinella septempuctata*) distal pad on untreated hydrophilic glass (blue) and hydrophobic PFOTS coated glass (cream) substrates in air and underwater conditions (n=5 per box). The small black markers show the underlying data points. The two modes of contact during underwater experiments are represented separately: "*bubble*" and "*no bubble*". Crosses represent theoretical predictions of adhesion force, while, circles represent the contribution of the bubble itself, calculated from the capillary bridge model (see text and Table 3.4). Two-way ANOVA test showed a significant effect of the *contact mode* ($p=0.001$, $F=9.596$, degrees of freedom=2) and *substrate* ($p<0.001$, $F=36.231$, degrees of freedom=1). Significant interaction between the above two categories was seen ($p=0.001$, $F=10.551$, degrees of freedom=2).

3.2.2.3. Statistical comparison

Two-way ANOVA test showed a significant effect of the *Contact mode* (p=0.001, F=9.596, degrees of freedom=2) and *Substrate* (p<0.001, F=36.231, degrees of freedom=1) categories on the single leg adhesion force measurements of the ladybug beetle (*Coccinella septempuctata*). Significant interaction between the above two categories was seen (p=0.001, F=10.551, degrees of freedom=2). Post-hoc analysis results are shown below (Table 3.2). The uncorrected p-values and Common Language Effect Size (CLES) were obtained from pair-wise Student t-test between A and B while keeping the third parameter fixed (degrees of freedom=8 for each pair). p-values showing statistically significant difference between A and B are in boldface. CLES represents the statistical proportion of samples under A with higher adhesion than under B. The condition for statistical significance is based on the Bonferroni-corrected critical p-value of 0.008.

Table 3.2.: Post-hoc t-test results for each combination of contact mode and substrate

Fixed variable	A	B	T	p-value	CLES
In air	PFOTS	Glass	-0.053	0.959	0.48
Underwater: bubble	PFOTS	Glass	3.292	0.011	0.96
Underwater: no bubble	PFOTS	Glass	10.044	0.0	1.0
PFOTS	In air	Underwater: bubble	0.133	0.897	0.48
PFOTS	In air	Underwater: no bubble	-0.224	0.828	0.48
PFOTS	Underwater: bubble	Underwater: no bubble	-0.37	0.721	0.44
Glass	In air	Underwater: bubble	4.688	0.002	1.0
Glass	In air	Underwater: no bubble	11.341	0.0	1.0
Glass	Underwater: bubble	Underwater: no bubble	2.086	0.07	0.84

The effect of substrate, contact mode, tilt angle, beetle identity and repetition number on the adhesion were analysed using a linear mixed-effect model (LMEM)

Table 3.3.: Linear mixed-effect model statistics

	Estimate	**Std. Error**	**z**	**p-value**
Intercept[1]	582.072	170.307	3.418	0.001
PFOTS	-110.642	206.268	-0.536	0.592
Underwater: bubble	-304.667	89.458	-3.406	0.001
Underwater: no bubble	-254.924	117.386	-2.172	0.03
Repetition number	7.723	6.703	1.152	0.249
Tilt angle	-5.649	7.088	-0.797	0.425

in Python. Here, each experimental data point was considered distinctly without averaging the repeats as before. Substrate, contact mode, tilt angle and repetition number were taken as fixed-effects, while, beetle identity was considered as the random-effect. Interaction between each of the fixed-effects were fitted using the random intercept model. Adhesion measurement on hydrophilic glass *in air* was taken as the reference. The resultant fixed-effects coefficient estimates, standard error, z-statistic and p-value are reported below (Table 3.3). The random-effect (beetle identity) showed an intercept standard deviation of 100.563 µN (std. error = 109.771)

3.2.2.4. Capillary force due to an air bubble

Capillary force of a single air bubble against a PFOTS-coated glass surface are compared for two different volumes (Figure 3.3). The volumes correspond to the expected range for the case of the trapped air bubble in a ladybug's pad. Here, the bubble was pinned to a micropatterned PDMS substrate on the top. Approach-retract tests were performed at 62.5 µm s^{-1} speed. The maximum adhesion force of any of the bubbles never exceeds 50 µN, significantly lower than the beetle's underwater adhesion to the same substrate ($>$ 400 µN). Thus, the bubble's contribution to adhesion in the "*underwater: bubble*" contact of a ladybug's pad should be negligible ($<$ 10 %).

[1] *adhesion on glass in air*

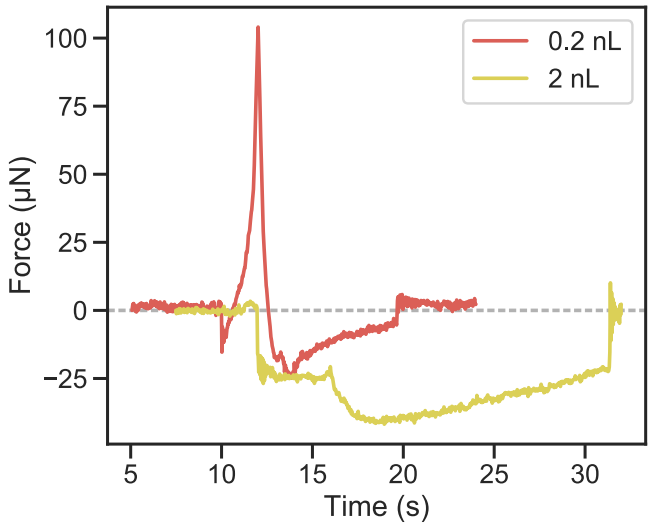

Figure 3.3.: Capillary force of the pinned bubble against a PFOTS-coated glass surface

3.3. Theory

3.3.1. Capillary Bridge Model

The male ladybug beetles used in my experiments are known to possess mostly discoidal hairs on their distal pad. Contact images show that these hair tips are approximately circular (eccentricity ~ 0.04), which could allow mechanical pinning of the secreted fluid around its perimeter. Based on this knowledge, I modelled the hairy pad as an array of N cylindrical rods of length, L, and diameter, D_h, fixed to a flat circular pad of diameter, D_p (Figure 3.4). The hairs and the pad were assumed to be perfectly rigid, for simplicity. The tip of each hair has a tarsal adhesive fluid of volume V_f, mediating contact with the substrate. The fluid is pinned to the circumference of the hair and forms a capillary bridge of height, d. Similar to my experiments, I considered three modes of contact for the pad: 1) *In air*, 2) *Underwater: no bubble* and 3) *Underwater: bubble*. In the third case, a bubble of volume, V_b, is trapped between the hairs and pinned to the pad circumference ("Cassie state").

To characterise the tarsal adhesive fluid and bubble volume, I defined two radii, s_f and s_b, respectively, by $V_f = \frac{4}{3}\pi s_f^3$ and $V_b = \frac{4}{3}\pi s_b^3$. Here, s_f and s_b are the radii

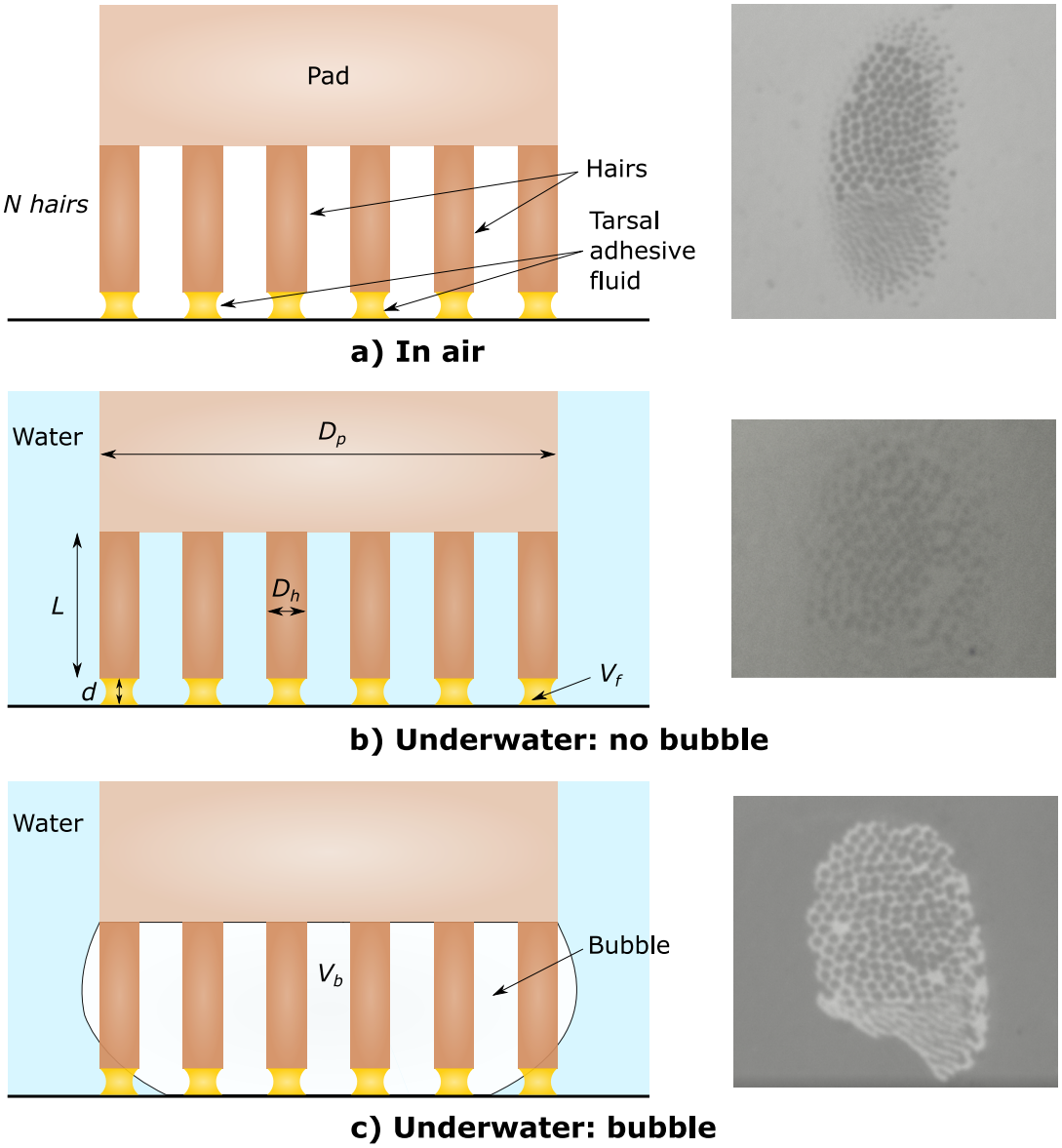

Figure 3.4.: The capillary bridge model of a hairy adhesive pad. The hairs make contact with the substrate (hydrophilic or hydrophobic) in three modes: a) *In air*, where the tarsal adhesive fluid bridges are surrounded by air; b) *Underwater: no bubble*, where the fluid bridges are fully surrounded by water; c) *Underwater: bubble*, where part of the fluid bridges are inside the bubble while others are outside in water (see text for details). The corresponding ventral view contact images of the beetle's pad seen during adhesion experiments are shown on the right.

of spheres with equivalent volumes. Fluid and bubble radii were assumed to scale proportional to their corresponding pinned contact diameter. I thus defined the size parameters, $\phi_f = D_h/(2s_f)$ and $\phi_b = D_p/(2s_b)$ for the fluid and bubble respectively, to conveniently scale their volumes relative to the hair and pad diameters they are pinned to. Larger values of ϕ_f (ϕ_b) represents a smaller volume of liquid (bubble) relative to the hair (pad) that it is pinned to.

The net force of the array, F_{net}, for cases 1 and 2 can be calculated as:

$$F_{net} = Nf \tag{3.1}$$

Here, f is the capillary force of a single fluid bridge at a distance, d, in air (f_{air}) or underwater (f_{water}).

For case 3, the net force is given by:

$$F_{net} = N_{in}f_{air} + N_{out}f_{water} + f_{bubble} \tag{3.2}$$

Here, N_{in} and N_{out} are the number of hairs inside and outside the bubble, respectively, f_{air} and f_{water} are the capillary forces of the fluid bridge inside and outside the bubble, respectively, and f_{bubble} is the capillary force contribution due to the bubble meniscus alone at distance $d + L$.

The capillary force, f, is the sum of two contributions: Laplace pressure and surface tension, as given by:

$$f = \Delta P_{laplace} A_{_{bottom}} + 2\pi R_{bottom}\gamma \sin\theta \tag{3.3}$$

Here, $\Delta P_{laplace}$ is the Laplace pressure of the equilibrium capillary bridge, θ is the contact angle, A_{bottom} is the contact area of the capillary bridge with the substrate at bottom and R_{bottom} is the corresponding radius of contact. Unlike previous analytical treatments[2,60], force versus distance for a single capillary bridge was calculated by Surface Evolver simulations[12,26], and used to obtain F_{net} as a function of d for each mode of contact. The adhesion force of the complete hairy pad system was then obtained from the minima of F_{net}, where negative force values represent attraction.

I considered f_{air} and f_{water} to be distinct terms because the capillary force by the tarsal adhesive fluid would be different in air and underwater due to its different

Table 3.4.: Fixed parameters corresponding to the pad's geometry, tarsal fluid and substrate wetting properties used in the capillary bridge model

Property	Value
Number of hairs, N	500
Hair diameter, D_h	4 µm
Pad diameter, D_p	200 µm
Hair length, L	40 µm
Water surface tension, γ_{wa}	72 mN m^{-1}
Tarsal fluid-air surface tension, γ_{fw}	27 mN m^{-1}
Tarsal fluid-water interfacial tension, γ_{fw}	55 mN m^{-1}
Tarsal fluid volume, V_f	4 fL
Bubble volume, V_b	1 nL
Hydrophilic substrate wetting	$\theta_{fa} = 6°$
	$\theta_{wa} = 20°$
Hydrophobic substrate wetting	$\theta_{fa} = 56°$
	$\theta_{wa} = 93°$

contact angle and interfacial tension in each case. Using the Young-Dupré equations for each case of fluid-air, fluid-water and water-air interface, one can derive the following relation for the contact angle of the tarsal adhesive fluid underwater:

$$\cos\theta_{fw} = \frac{\gamma_{fa}\cos\theta_{fa} - \gamma_{wa}\cos\theta_{wa}}{\gamma_{fw}} \tag{3.4}$$

Here, θ_{fw} and θ_{fa} are the contact angles of the tarsal adhesive fluid with the substrate in water and air respectively, θ_{wa} is the contact angle of water with the substrate in air, γ_{fa} is the surface tension of the tarsal adhesive fluid, γ_{wa} is the surface tension of water and γ_{fw} is the interfacial tension of the tarsal adhesive fluid with water.

Geometric parameters and interfacial properties were kept fixed for all model calculations (Table 3.4). Here, I assumed the tarsal adhesive fluid to have similar interfacial tension values as n-hexadecane[40]. Experimental receding contact angle values for n-hexadecane and water on untreated (hydrophilic) and fluorinated (hydrophobic) glass surface were used as θ_{fa} and θ_{wa}, respectively (Table S1). Hair and pad geometry, and tarsal fluid volume were assumed to be values typical for a ladybug's hairy pad[14,76].

First, I calculated force-distance curves for a single pinned liquid capillary bridge. Second, the effect of substrate on the force-distance curves of the hairy pad system

was compared for each mode of contact. The volume of the bubble would influence it's capillary force as well as the proportion of hairs that are inside or outside the bubble. Thus, I also looked at the effect of changing the bubble volume, $\hat{V}_b$, on the net underwater adhesion. Additionally, the influence of varying the hair diameter, D_h, on adhesion was studied for each case, to illustrate the 'contact splitting' effect[3].

3.3.2. Simulation method: Single capillary bridge

Capillary force due to a single adhesive fluid or bubble meniscus (termed "capillary bridge") was calculated by performing simulations in Surface Evolver[12], similar to the method described by de Souza et. al.[26]. A simple cubic geometry, mimicking the capillary bridge, of constant volume, V, was defined as the initial condition with an interfacial tension, γ, with the surrounding medium. Interfacial tension of the capillary bridge with the substrate is given by $\gamma \cos\theta$, where θ is the corresponding contact angle inside the bridge. For the case of a bubble meniscus, θ is defined w.r.t. the surrounding water, since θ can also directly characterise the substrate wettability. The capillary bridge spans a gap distance d between the top face and the substrate. The boundary conditions were set corresponding to a pinned contact line of diameter D on the top face and constant interfacial tension with the substrate on the bottom. All lengths were normalised relative to length $s = (3V/4\pi)^{1/3}$. An appropriate refinement and iteration routine was chosen by trial-and-error to get a stable converged solution corresponding to the minimum energy state of the capillary bridge surface. The normalised total capillary force, $\hat{f} = f/\gamma s$, is the sum of the Laplace pressure and surface tension contributions , where:

$$f = f_{laplace} + f_{surface\,tension} = \Delta P_{laplace} A_{bottom} + 2\pi R_{bottom} \gamma \sin\theta \qquad (3.5)$$

Here, $\Delta P_{laplace}$ is the Laplace pressure of the equilibrium capillary bridge, A_{bottom} is the contact area of the capillary bridge with the substrate at bottom and R_{bottom} is the corresponding radius of contact, all obtained from the simulation output for the equilibrium surface.

The gap distance d was varied step-wise and the capillary force was calculated each time to obtain force-distance curves for a particular choice of D and θ.

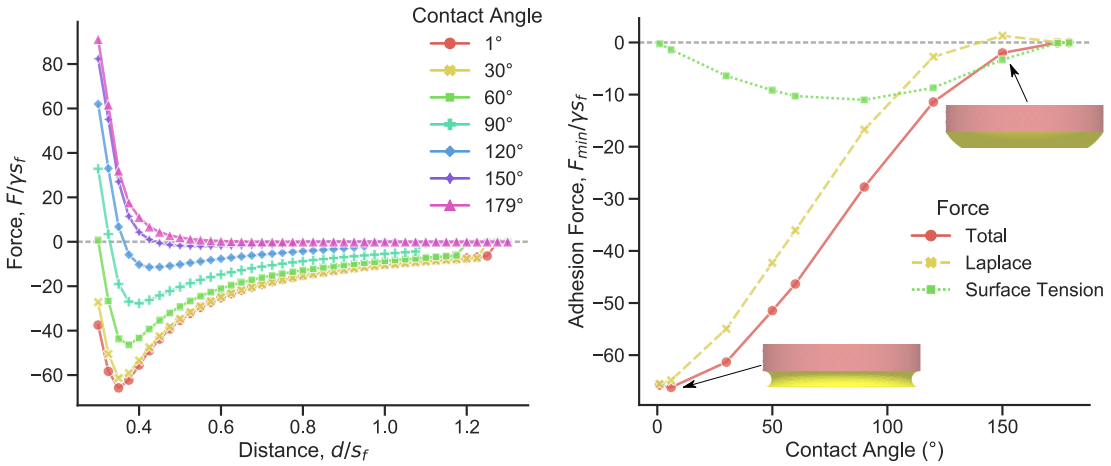

(a) Force-distance curves **(b)** Force contributions

Figure 3.5.: Simulation of normalised capillary force of a single liquid bridge in contact with a substrate and pinned to a circular perimeter on top. Fluid size parameter, $\phi_f = 2$. Negative force values represents attraction. a) Force-distance curves are shown for different contact angles of the liquid with the substrate. b) Adhesion forces, calculated from the minima of the corresponding force-distance curves, are plotted as a function of contact angle with the substrate, together with its Laplace and surface tension components. Simulation snapshots of the liquid meniscus corresponding to angles 6° and 150° are depicted.

3.3.3. Results

3.3.3.1. Capillary force of a single liquid bridge

Forces due to a single pinned capillary liquid bridge in contact with a substrate were obtained via Surface Evolver simulations (Figure 3.5). We see that, generally, the shape of the liquid meniscus determines the strength of its adhesion force. High adhesion ($>$ 60 % of maximum) is seen for contact angles less than $\sim$ 70° due to a net negative (convex) curvature of the meniscus, while low adhesion ($<$ 10 % of maximum) is seen for contact angles greater than $\sim$ 150° due to its net curvature being close to zero. The Laplace pressure contribution to the net adhesion force dominates for contact angles less than 100° (Figure 3.5b). Interestingly, its contribution to the adhesion force is mostly non-repulsive for contact angles greater than 90°. This is because, the low volume of the liquid and its pinned contact line prevents the meniscus from having a high positive (concave) curvature due to geometric constraints. Only for a contact angle of 150°, the liquid's curvature becomes positive, manifested in its slightly repulsive Laplace contribution. Surface

tension makes a significant contribution to the net force only for a small range of contact angles close to 90°. For contact angles greater than 150°, the net adhesion force approaches zero.

The force-distance curves show a general trend of repulsive forces at small distances, a minima at an intermediate distance corresponding to the adhesion force, and finally tending to zero force at large distances until the capillary bridge ruptures (Figure 3.5a). The repulsive force seen at small distances is a result of the pinned contact line on the top. A limited volume is available for the liquid to occupy when the gap distance is small, causing the meniscus shape to bulge outwards near the pinned contact line. This creates a net positive curvature, resulting in a positive Laplace pressure and thus repulsion. Without pinning, the capillary forces would have shown high attractive forces on a hydrophilic substrate[26]. It is reasonable to expect the contact line to be mechanically pinned around the rim of the discoidal-shaped hair tip. Since the male ladybug's pads are majorly composed of discoidal hairs, I proceed with this assumption to estimate the net adhesion force of the whole pad.

3.3.3.2. Single capillary bridge: Effect of volume

Surface Evolver simulation results showing the effect of volume on the maximum capillary force of a single fluid bridge. Since the fluid is pinned at the top to the same diameter, D, a smaller volume would result in high interfacial curvatures, which increases the capillary force due to the negative Laplace pressure. In this case, small contact angles lead to a greater increase in adhesion.

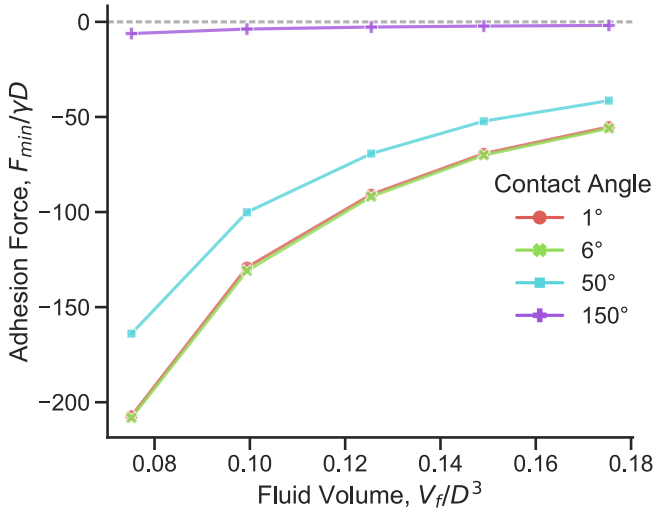

Figure 3.6.: Normalised maximum capillary force for a single bridge as a function of fluid volume

3.3.3.3. Adhesion of a hairy pad: Effect of the substrate

The force-distance curves of a hairy pad system on a hydrophilic and hydrophobic substrate are predicted based on the capillary bridge model and compared for the different contact modes (Figure 3.7). The forces in each case are calculated from equations (3.1) and (3.2) for fixed geometric and interfacial properties (Table 3.4).

On the hydrophilic substrate ($\theta_{wa} = 20°$), highest adhesion is seen when the hairs contact in air, while lowest adhesion occurs underwater without a trapped bubble. The presence of a bubble leads to intermediate force values. In contrast, on a hydrophobic substrate ($\theta_{wa} = 93°$), highest adhesion is seen for the underwater case without a trapped bubble, much larger than in air. When a bubble is present, the forces are only slightly larger than in air.

The observed trend in forces can be explained by how the tarsal adhesive fluid wets the surface in each case. On a hydrophilic substrate, the contact angle of the oily fluid is 6°, when surrounded by air (Table 3.4) and 138°, when surrounded by water (equation (3.4)). This results in the meniscus shape to have a net negative and slightly positive curvatures, respectively, resulting in strong adhesion in air and poor adhesion underwater. On a hydrophobic substrate however, the contact angles of the fluid in air and water are 56° and 70°, respectively. In both cases, the contact angles are low, resulting in strong adhesion in both media. Additionally,

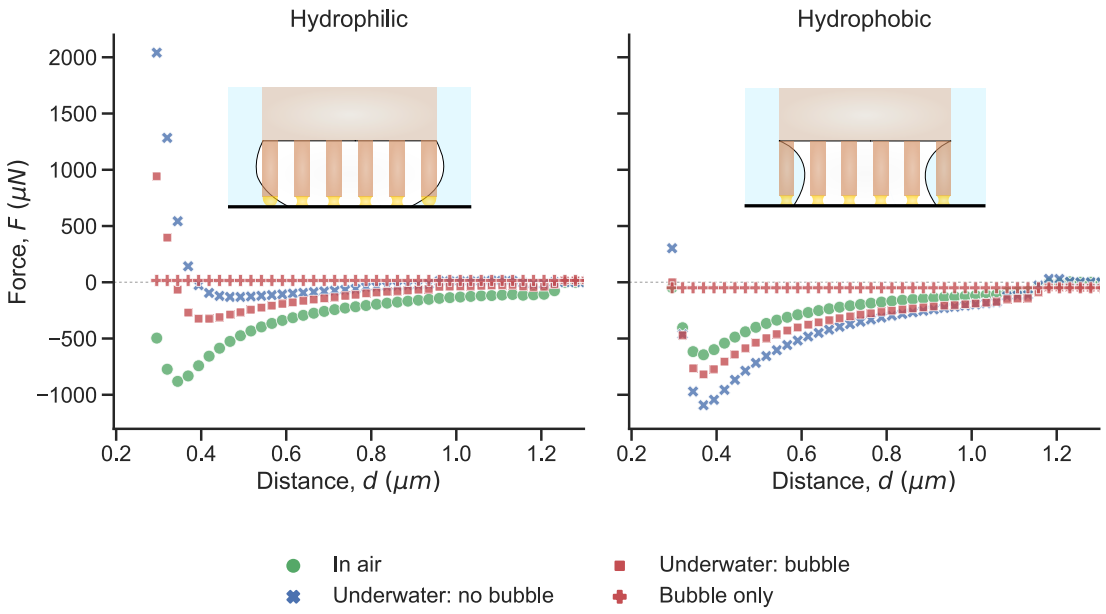

Figure 3.7.: Theoretical force-distance curves of a hairy pad on a hydrophilic and hydrophobic substrate in air and underwater conditions. A negative force value represents attraction. Forces are calculated from the capillary bridge model, with model parameters listed in Table 3.4. The bubble's contribution to the net force for an *underwater: bubble* contact is denoted by plus symbols. Insets represent the *underwater: bubble* contact for each substrate.

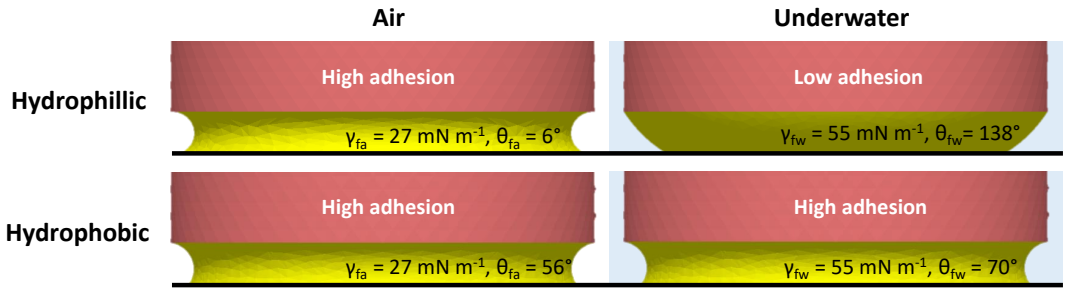

Figure 3.8.: Simulation snapshots of oil capillary meniscus in contact with untreated glass and PFOTS-coated glass in air and underwater conditions. The corresponding interfacial tension, γ, and contact angle, θ, used to predict the ladybug's adhesion are labelled for each case.

the interfacial tension of the oily fluid underwater (γ_{fw}) is twice that of in air (γ_{fa}). Thus, we see a higher capillary adhesion for the *underwater: no bubble* case when compared to *in air* (Figure 3.8). Note that since the hair diameter is kept fixed, the observed effects are not a result of changing contact area, but rather of the nature of capillary forces.

The net force in the *underwater: bubble* case mainly depends on the proportion of hairs inside and outside the bubble (equation (3.2)). For the given bubble volume, only part of the hairs make contact with the surface inside the bubble. Therefore, the force curve lies between *in air* and *underwater: no bubble* cases for both substrates.

I observed that the bubble itself does not contribute much to the net force on either substrate (Figure 3.7). Its contribution even is slightly repulsive on the hydrophilic substrate due to the positive curvature of the bubble, and slightly attractive on the hydrophobic substrate due to its negative curvature. This small contribution is manifested by the slightly higher adhesion for *underwater: bubble* relative to *in air* for the hydrophobic substrate, since all hairs are within the bubble in this case.

3.3.3.4. Adhesion of a hairy pad: Effect of the air bubble volume

The volume of the trapped air bubble can influence its capillary force contribution, as well as change the relative proportion of hairs inside and outside it. To investigate this, I varied the bubble volume, V_b, and compared the maximum adhesion force on both hydrophilic and hydrophobic substrates (Figure 3.9). The contribution of the

bubble to the net adhesion force is small regardless of its volume, when compared to the whole pad (less than 3 %). Further, opposite trends of adhesion are seen on the two substrates with changing V_b.

From the previous section, we know that on the hydrophilic substrate, fluid bridges outside the bubble show poor adhesion due to the positive curvature of their meniscus. Thus, decreasing V_b decreases the adhesion force due to a larger proportion of tarsal hairs being outside the bubble. In contrast, on the hydrophobic substrate, fluid bridges outside the bubble showed higher capillary forces, due to its low contact angle and high interfacial tension in water. Thus, adhesion force increases for a hydrophobic substrate as the bubble size decreases.

A smaller V_b resulted in increased, but small, attraction by the bubble on both types of substrates. For larger values of V_b however, the force trend for the whole pad mostly follows that of the bubble. This is because the bubble gets big enough to entrap all the hairs inside it (Figure 3.9 inset). Thus, the force contribution due to the fluid bridges remain unchanged, and only the bubble's contribution drives the slight variation in the pad's adhesion at high V_b. Once the bubble is small enough such that part of the fluid bridges start making contact in water, the force trend changes, with a steep decrease (increase) in adhesion force on hydrophilic (hydrophobic) substrate with decreasing bubble volume.

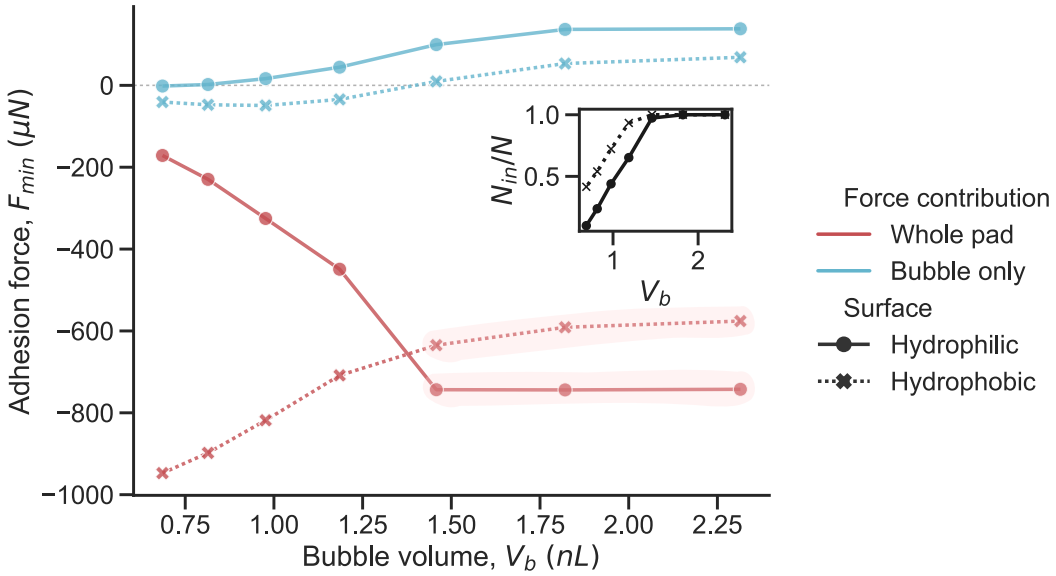

Figure 3.9.: Adhesion force of a hairy pad as a function of bubble volume, V_b, for the *underwater: bubble* contact mode. Adhesion forces are calculated from the minima of the respective force-distance curves. Negative force value represents attraction. The inset plot shows the corresponding fraction of hairs, N_{in}/N, making contact inside the bubble. Highlighted regions represent entrapment of all hairs within the bubble. Remaining model parameters are kept fixed, as listed in Table 3.4

3.3.3.5. Adhesion of a hairy pad: Effect of the hair tip diameter

The tarsal hairs on a ladybug's adhesive pad terminate in various shapes, such as 'discoidal' or 'pointed'. I studied this geometric effect on adhesion by changing the hair tip diameter, D_h (Figure 3.10). Here, I fix the total contact area to 6283 µm^2 (corresponding to Figure 3.7) and vary the number of hairs with D_h to illustrate the "contact splitting" effect. The tarsal adhesive fluid volume is assumed to scale relative to the hair diameter ($\phi_f = 2$). The pad diameter, hair length and bubble volume are kept fixed as per Table 3.4.

Adhesion force increases with decreasing D_h for both hydrophilic and hydrophobic substrates in all contact modes. This is consistent with the 'contact splitting' theory, which predicts higher adhesion when the contact is split into many small contact points[3]. Reducing the hair diameter results in two competing effects: 1) capillary force due to a single fluid bridge decreases due to its smaller size and 'self-similar' scaling assumption ($f \sim D_h$), which decreases the net force, and 2) total

number of fluid bridges increases since the total hair contact area is assumed to be fixed ($N \sim 1/D_h^2$), which increases the net force. The second effect dominates, resulting in a higher adhesion force as D_h decreases.

Similar to the trend in Figure 3.7, contact *in air* shows the highest adhesion force on a hydrophilic substrate for the given range of hair diameters, while on a hydrophobic substrate, *underwater: no bubble* shows highest adhesion. *Underwater: bubble* contact shows intermediate adhesion between *in air* and *underwater: no bubble* contact modes.

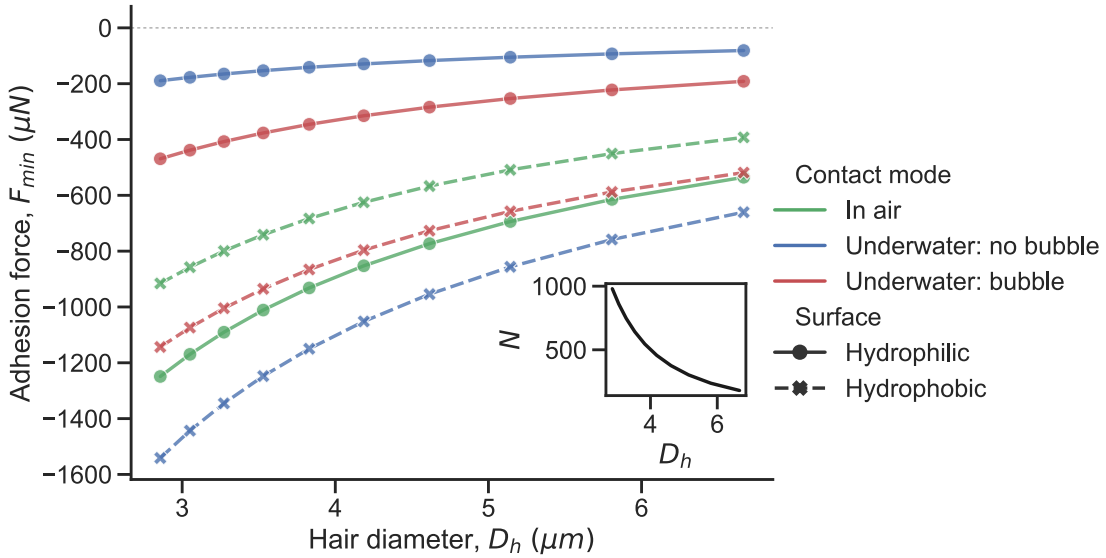

Figure 3.10.: Adhesion force of a hairy pad on a hydrophilic and hydrophobic substrate as a function of hair tip diameter, D_h. Volume of each fluid bridge, V_f, scales relative to D_h based on the parameter $\phi_f = 2$. Total contact area is kept fixed to 6283 µm^2 throughout. The number of hairs, N, varies with D_h, as shown in the inset plot. Adhesion forces are calculated from the minima of the respective force-distance curves, based on the capillary bridge model. A negative value represents attraction. Remaining model parameters are kept fixed, as listed in Table 3.4

3.3.3.6. Capillary Bridge Model: Effect of hair diameter at constant fluid volume

Here, instead of scaling the fluid volume relative to the hair diameter, I now assume a fixed total fluid volume distributed equally among the N hairs. Total fluid volume, $V_{total} = NV_f = 2000$. Hair diameter is varied while keeping the total hair contact

area constant. Length is in arbitrary units. Forces increase at a much smaller rate on decreasing diameter when compared to the case with self-similar scaling of fluid volume (Figure 8 in main text).

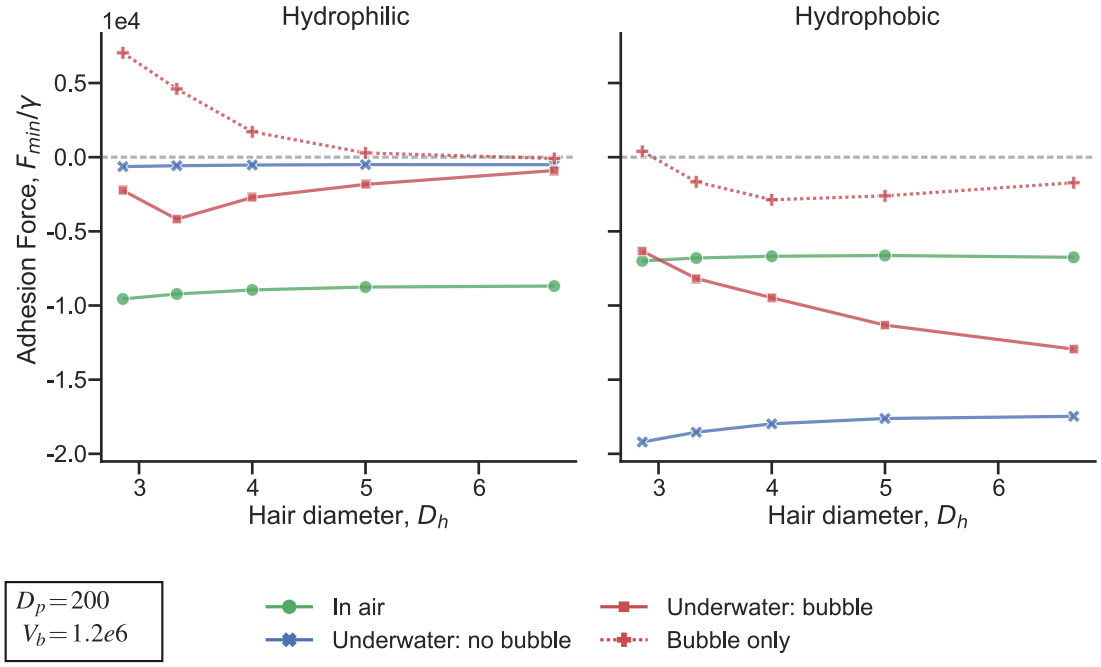

Figure 3.11.: Normalised adhesion force of hairy pad system on a hydrophilic and hydrophobic substrate as a function of hair diameter (D_h), calculated from the capillary bridge model. The total adhesive fluid volume is fixed to 2000. Adhesion forces are calculated from minima of the respective force-distance curves. Negative force value represents attraction. The bubble's contribution to the net force for an *underwater: bubble* contact is denoted by plus symbols. Bubble volume and pad diameter are kept fixed. All lengths are scaled relative to D_p.

3.3.3.7. Capillary bridge model: Sensitivity analysis

Sensitivity analysis was performed using the one-at-a-time (OAT) method. Dimensionless model parameters were initially set to correspond to the ladybug's case, as given by, contact area fraction ($\alpha = ND_h^2/D_p^2 = 0.1$), pad to hair diameter ratio ($D_p/D_h = 50$), hair aspect ratio ($L/D_h = 10$), water surface tension ratio ($\gamma_{wa}/\gamma_{fa} = 3$), tarsal fluid-water interfacial tension ratio ($\gamma_{fw}/\gamma_{fa} = 2$), tarsal fluid size parameter ($\phi_f = 2$), bubble size parameter ($\phi_b = 1.6$). Substrate contact angles were kept fixed (same as in main text). Each parameter was varied within a particular range, one at a time, and the corresponding adhesion forces *in air* (F_a),

underwater: no bubble (F_w) and *underwater: bubble* (F_b) were calculated. Linear least square regression was performed to quantify the relative change in adhesion for each contact mode with respect to the varied parameter. Here, F_w/F_a and F_b/F_a were taken to be the model output. Slope and R^2 values for each case are reported below (Table 3.5). Slope with absolute values greater than 0.5 are highlighted in bold.

Table 3.5.: Sensitivity analysis

Param.	**Range**	**Substrate**	**F_w/F_a**		**F_b/F_a**	
			slope	**R^2**	**slope**	**R^2**
α	0.05 - 0.3	Hydrophilic	3.03E-18	1.52E-03	2.30E-01	7.72E-01
		Hydrophobic	-9.69E-17	3.03E-03	**-9.40E-01**	7.72E-01
D_p/D_h	30 - 60	Hydrophilic	-8.83E-20	1.48E-01	1.28E-02	9.73E-01
		Hydrophobic	-5.65E-18	1.48E-01	-1.51E-02	9.82E-01
L/D_h	8- 15	Hydrophilic	0.00E+00	0.00E+00	-5.27E-02	9.11E-01
		Hydrophobic	0.00E+00	0.00E+00	5.41E-02	8.66E-01
γ_{wa}/γ_{fa}	2.5 - 3.5	Hydrophilic	-2.01E-01	8.57E-01	-2.43E-01	9.43E-01
		Hydrophobic	4.11E-02	1.00E+00	6.87E-02	1.00E+00
γ_{fw}/γ_{fa}	1.5 - 2.5	Hydrophilic	2.01E-01	8.62E-01	1.90E-01	8.94E-01
		Hydrophobic	**5.56E-01**	1.00E+00	1.57E-01	1.00E+00
ϕ_f	1.7 - 2.2	Hydrophilic	1.29E-02	4.52E-01	6.18E-02	7.94E-02
		Hydrophobic	7.67E-02	9.84E-01	-3.06E-01	9.66E-01
ϕ_b	1.2 - 1.8	Hydrophilic	0.00E+00	0.00E+00	**-1.14E+00**	8.85E-01
		Hydrophobic	0.00E+00	0.00E+00	**1.46E+00**	9.78E-01

3.4. Discussion

3.4.1. Role of bubble

My experiments demonstrate that the ladybug beetle can attach underwater to a hydrophobic substrate even without a bubble trapped around its tarsal hairs. A previous study[47] proposed that an air bubble is necessary for underwater attachment in terrestrial beetles. This is, however, only true for hydrophilic substrates, where a trapped air bubble can facilitate underwater adhesion due to the hairs making contact in a de-wetted environment. For a hydrophobic substrate, the adhesion is similar regardless of whether the contact occurs in air or underwater conditions, with or without a trapped bubble. My theoretical calculations further show that

the bubble by itself has a negligible capillary contribution (less than 3%) to the net underwater adhesion of the pad. Direct force measurement of a single similarly sized bubble making contact with a hydrophobic substrate shows a maximum adhesion less than 50 µN, which further validates that the bubble's contribution is insignificant (Figure 3.3).

3.4.2. Origin of underwater adhesion

Predictions of the ladybug's adhesion from the capillary bridge model agree qualitatively with my experimental results (Figure 3.2). In underwater conditions without a trapped air bubble, adhesion to a hydrophobic substrate is significantly larger than to a hydrophilic substrate. This is explained by the different interfacial tension of the oily tarsal secretion and its contact angles with the substrates in air and underwater, which determines the capillary adhesive force in each case (Figure 3.8). However, the experiments do not show the predicted ~ 1.7 times increase in underwater adhesion relative to that in air on the hydrophobic PFOTS-coated surface. This discrepancy could be due to my assumptions of the oily fluid's interfacial properties, which are not known for the ladybug beetle. Sensitivity analysis of the model does in fact show that the relative adhesion underwater when compared to that in air is sensitive to the fluid's interfacial tension values in air and water. Direct measurement of the fluid's interfacial properties is thus essential to better predict the insect's adhesion, and will be a subject of future studies. Further, due to surface inhomogeneities, not all the hairs might be able to completely drain the interfacial water layer, in order for the tarsal adhesive fluid to make direct contact with the substrate. This can further reduce underwater adhesion, in comparison to my theoretical predictions which assumes a perfect contact of all hairs' terminals.

3.4.3. Validity of model

In the model, I assume that all the hairs detach simultaneously to give a theoretical maximum achievable adhesion force. In my experiments, however, not all hairs make a perfect contact with the substrate despite my best efforts to align the pad parallel to the surface. Furthermore, during detachment, the constrained pad typically peels off from its proximal to distal end rather than detach simultaneously. My model also assumes the hairs to be stiff and of similar geometry,

unlike the male beetle's pad which has a distribution of flat or pointed tipped soft hairs. Thus, it is not surprising that the model overestimates the adhesion forces. However, when comparing the adhesion in air and underwater, the effect of pad orientation, peeling, hair geometry or elasticity on adhesion should be similar for both cases, and thus, can be reasonably ignored. The model predictions are in the same order of magnitude as experiments, and the qualitative trend is consistent for both hydrophilic and hydrophobic substrates in air and underwater. Further, sensitivity analysis of the model showed that the relative underwater adhesion when compared to that in air was insensitive to the hair or pad geometrical parameters, which validates the applicability of the model for my choice of parameters. Interfacial tension influenced the relative adhesion for *underwater: no bubble* case, while, contact area and bubble volume influenced the relative adhesion for *underwater: bubble* case, as expected.

3.4.4. Role of tarsal secretions

My study provides further validation that capillary forces govern the ladybug's adhesion and van der Waals contributions, if any, must be negligible. Further, the capillary forces can even enable ladybug attachment underwater depending on the substrate chemistry. When underwater, without a trapped bubble, the pads adhere strongly to a hydrophobic substrate, but poorly to a hydrophilic substrate, even though the pad shows similarly strong adhesion to both substrates in air. This effect can be explained by capillary forces and the wetting properties of the fluid. My preliminary chemical composition analysis of a beetle's tarsal secretions before and after immersing its leg underwater (unpublished data) suggests that the tarsal adhesive fluid do not get washed away when underwater. Therefore, the fluid should be able to form capillary bridges and help mediate adhesion even when underwater.

The presence of interfacial water was expected to cause adhesion loss during underwater contact. However, we see that, underwater adhesion is possible even for a hydrophilic surface without a trapped bubble (Figure 3.2). This suggests the possible role of interfacial water drainage dynamics on adhesion. The experimental adhesion values lie close to the theoretical predictions, which suggests that the interfacial water is drained out within the time-scale of contact ($\sim$ 4 s). The tarsal fluid would then form capillary bridges in direct contact with the surface and enable adhesion. The details of this drainage mechanism during capillary mediated

underwater adhesion would be interesting to look at in a future study.

3.4.5. Similar effect in other animals

To some extent, the findings could be extended to other animals relying on oily secretions for adhesion. For example, ants are known to possess smooth adhesive pads which secrete a fluid containing oily substances[36]. It has been reported that some ants show similar adhesion on hydrophobic substrates under wet and dry conditions[84], similar to what we see in a ladybug. This observation can again be explained by a capillary model as before, where, the wetting and interfacial tension of the ants' secretion could mediate their underwater adhesion to hydrophobic substrates. Previous experiments on geckos revealed that they can attach well to fluoropolymer substrates (such as PTFE) when underwater, while they show little adhesion to the same substrate in air[82,83]. Geckos are thought to rely on van der Waals forces via dry contact with the substrate[7], although observations of phospholipid footprints left behind walking geckos[48] could change that picture. A recent study has in fact presented evidence for the importance of polar interactions in gecko adhesion mediated by this phospholipid layer[80]. This calls for a reinterpretation of previously reported gecko adhesion data by considering the influence of the phospholipid layer. In principle, a capillary model could be used to describe the adhesion mediated by this layer, by assuming that the phospholipid compound is mobile with liquid-like properties. Since geckos adhere poorly to PTFE (surface energy ~ 20 mN m^{-1}), one can speculate that the phospholipid material has a higher surface energy, and consequently makes a higher contact angle with PTFE in air. Let us assume the phosopholipid substance to be a fluid similar to oil with γ_{fa}= 30 mN m^{-1} and γ_{fw}= 42 mN m^{-1} such that its contact angle with PTFE is 80°. Equation 3.4 then gives us an underwater contact angle of 70° for the phospholipid fluid. Thus, on a PTFE surface, the capillary bridge model can predict a higher adhesion underwater than in air due to its lower contact angle and higher interfacial energy underwater. Based on similar assumptions, I predict the net adhesion force for the gecko on different substrates (Figure 3.12). The adhesion force predictions are in good qualitative agreement with the whole animal experimental shear force values reported for the gecko, with the trend of higher adhesion in air than underwater for glass, similar adhesion in air and underwater for PMMA/OTS-SAM and lower adhesion in air than underwater for PTFE. We, thus, propose that the

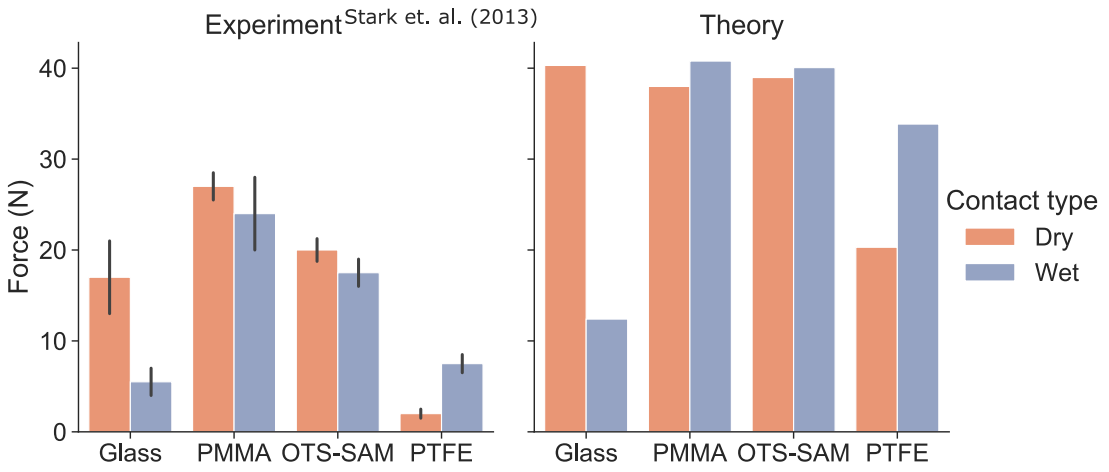

Figure 3.12.: Whole animal adhesion force of geckos on various substrates. Experimental shear adhesion values are reproduced from Stark et al. [82]. Normal adhesion forces for each gecko toe are theoretically estimated from the capillary bridge model, with hair diameter = 400 nm, toe diameter = 4 mm, phospholipid fluid volume = 4.19x10^{-3} fL and 10% hair coverage. "*Underwater: no bubble*" contact mode is assumed for the "Wet" case. Net adhesion force is calculated by assuming 5 toes on each leg and 4 legs in total on a gecko. Interfacial tension of the phospholipid layer (PL) in air and water are assumed to be 30 mN m^{-1} and 42 mN m^{-1} respectively. PL contact angles with glass, PMMA, OTS-SAM and PTFE are assumed to be 6°, 10°, 20° and 80° respectively. The corresponding water contact angles are 50°, 85°, 94° and 97° respectively, as reported in Stark et al. [82].

underwater experiments performed on geckos[82,83] indicate a capillary contribution to gecko adhesion. Previous studies on gecko adhesion have attributed capillary effects to be a result of water monolayers adsorbed from ambient humid air onto the spatuale hair tips[49,60,72]. I however emphasize that the capillary contribution in gecko adhesion could instead be a result of its setal phospholipid layer rather than water. The previously reported influence of humidity on gecko adhesion[49] could possibly be an effect of change in surface tension of the oily phospholipid layer at different humidity, which will in-turn influence the capillary adhesion force. Further work is however necessary to understand the details of the mechanism by which the phospholipid layer mediates gecko adhesion.

3.4.6. Limitations and outlook

I have so far limited my analysis to only smooth substrates. Of course insects have to cope with all kinds of surfaces including rough ones. Previous studies[33] have shown that substrate roughness is a more dominant parameter than substrate chemistry in controlling ladybug beetle traction force. Here, the length scale of surface roughness relative to the tarsal fluid thickness would be important in the formation of stable capillary bridges. Further, the presence of air plastron between the roughness asperities can influence the nature of contact when underwater. Future work will explore how roughness can impact the net capillary force also in wet and submerged conditions. In my study, I have only considered normal adhesive forces, but insects like beetles in general rely on friction or shear forces during locomotion. Friction force usually correlates directly with the normal force, which is probably why previously reported shear adhesion forces of the dock beetle[47] follow a similar qualitative trend as my normal adhesion force measurements on the ladybug beetle in both air and underwater conditions. However, the details of the interplay between friction and normal adhesion forces in animals is an open question and is beyond the scope of my study.

My work can contribute to potential applications in the design of bio-inspired materials to achieve underwater adhesion via capillary bridges. Introduced bubbles can possibly be used to control underwater adhesion by changing the relative proportion of the arrays inside and outside the bubble. A suitable choice of an adhesion-mediating fluid can be made tailored to the substrate and environment of application to form capillary bridges with optimal adhesion performance in bio-inspired fibrillar adhesive systems.

3.5. Conclusion

Ladybug beetles rely primarily on their oily fluid secretion at the tarsal hair tips to adhere to surfaces in both air and underwater conditions. The beetles can attach underwater on a hydrophobic substrate even without a trapped air bubble within its hairy pad, although it loses this ability on a hydrophilic substrate. This is explained theoretically by the different contact angle and interfacial tension of the secreted fluid in air and underwater conditions. Further, the bubble itself has a negligible capillary contribution (less than 3%) to the total force. The trapped bubble can

promote adhesion only on a hydrophilic substrate by providing an air medium to the adhesive fluid bridges inside it. Oil wettability, thus, primarily controls the insect's adhesion in any given condition. My work here highlights how a fluid-mediated strategy can help achieve strong adhesion even underwater. A similar argument also explains previously reported underwater adhesion force measurements in geckos[82], which suggests the possibility of capillary contributions to gecko adhesion mediated by an oil-like phospholipid layer. My results inspire the necessity to characterise the insect's secretions, since their interfacial and wetting behaviour against a particular substrate is the primary driver of the insect's adhesion, even when underwater.

4. Surface tension measurement of micro-droplets

4.1. Summary

My results from the previous chapter showed that it is quite important to understand the wetting characteristics of an insect's foot secretions. In this regard, surface tension is an important property to be quantified. One could easily measure liquid surface tension using commercially available tensiometers (e.g. Wilhelmy plate method), or by optical imaging (e.g. pendant drop method). However, such instruments are designed for bulk liquid volumes of the order of millilitres or higher. In order to perform similar measurements on extremely small sample volumes in the range of the insect's secretions (femtoliter scale), Atomic Force Microscopy (AFM) can be a promising tool. In this chapter, I report a new method to make surface tension characterisation of microscopic liquid drops by performing AFM measurements on them using standard pyramidal cantilever tips. In order to prevent the drop from being picked up by the cantilever tip during the measurement, the cantilevers were coated with a hydrophilic polyethyleneglycol-based polymer brush in a simple one-step process. Such a coating reduced its contact angle hysteresis for most liquids, while maintaining a relatively low contact angle with the tip. This ensures that a sufficiently high capillary force is exerted by the liquid to be detected by the AFM tip, and at the same time avoid contact line pinning which could result in the drop being picked up by the tip. Numerical simulations of a similarly sized liquid drop interacting with a pyramidal or conical geometry mimicking the geometry of the tip were then used to calculate surface tension from the experimentally measured force.

A significant portion of this chapter's contents will be a part of my future publication, currently under review[89]. In this work, AFM experiments on liquid droplets,

preparation of pegylated cantilever tips as well as Surface Evolver simulations for cone and pyramidal geometries and relevant Python scripts for data analysis were all conceived by myself under the guidance of [redacted]. Scanning electron microscopy images were taken with the help of [redacted] from MPIP. Some preliminary experiments using water droplets and polydimethylsiloxane-brush coated cantilever tips were performed with the assistance of [redacted] from MPIP and [redacted] from Technical University of Darmstadt.

4.2. Background

Effects of surface tension are ubiquitous in our everyday lives, whether it be the disintegration of a stream of water coming out of our shower head into smaller drops, formation of bubbles when we use soap, or sticking of sand particles on our wet feet during a fun beach holiday. It is a core concept in our present understanding of wetting phenomena, which emerged over the past few centuries, starting with da Vinci, in pursuit of explaining the counter-intuitive rise of water inside a thin capillary tube when partially immersed vertically on its surface[68]. Subsequent notable studies by von Segner, Young, Laplace and Gauss formalised our current understanding of such capillary action, where surface tension was introduced as the main liquid-dependant parameter in the model. One may intuitively imagine surface tension to be a net constant tension that liquid surfaces experience in all directions, analogous to the stretched rubber membrane of a balloon. This tension is a net consequence of an in-balance in the net interaction force experienced by molecules near the liquid interface[16].

Several measurement techniques have since been developed to measure surface tension of macroscopic liquids. A common strategy is to use an appropriate force measurement device to directly measure the tension on liquid surfaces. Here, the Wilhelmy plate method is a classic example[96], where the maximum force required to pull a thin plate vertically out of the liquid surface is measured. Surface tension can then be obtained by dividing the measured force with the wetted contact perimeter of the plate. On the other hand, methods such as the pendant drop method[1], spinning drop method[91] or oscillating drop method[10] rely on optical observations of the liquid drop shape under specific conditions to evaluate surface tension by

solving the Young-Laplace equation or the Rayleigh's equation[86].

While surface tension measurement of bulk liquids is simple using commercially available instruments based on the above techniques, they are, however, not suitable for microscopic measurements, where the available liquid sample volume is extremely low in the range of micrometer-sized droplets. Such small scale measurements can be especially useful to improve our understanding of some important natural phenomena, such as, how atmospheric aerosols impact climate change processes and human health[63], or, the nature of tiny secretions in the legs of certain insects which enable them to stick to most surfaces[39]. One of the first attempts in making such a measurement was by performing a Wilhelmy-like experiment with the use of Atomic Force Microscope (AFM). McGuiggan et. al.[70] attached a cylindrical quartz rod of roughly 100 µm to a tipless AFM cantilever probe, which was used to measure the liquid adhesion force and calculate surface tension. While their method gave reasonable values for low surface tension liquids such as tetradecane, the method, however, underestimated the values for water by 44% when compared to macroscopic results. This discrepancy was attributed to imperfections in the rod shape and water contamination. An improvement to the above method was reported by Yazdanpanah et. al.[99], where, a 'nanoneedle' of gallium-silver alloy was grown on the sharp tip at the end of a standard AFM cantilever. These nanoneedles (diameter ∼100 nm), have a more well-defined cylindrical geometry, which allowed for precise surface tension measurement of liquids, including water. An alternative approach was to track the droplet oscillations induced by either coalescence using optical tweezers[19] or while under flight when ejected through an ink-jet nozzle[43,71,81]. The droplet oscillations, whose resonance frequency modes depend on the liquid surface tension based on Rayleigh's theory[86], can then be analysed using high speed optical detectors. Similar experiments could also be performed on hemispheric sessile drops using an AFM by measuring the oscillations when a liquid interface comes in contact with a hydrophobic colloidal probe[69].

Based on the above review, AFM provides in principle a relatively easier way to measure surface tension of small droplets without the need to construct specific experimental setups. Further, AFM is quite versatile since even submicrometer sized droplets can be probed with high resolution, which is not possible using alternative optical methods. Presently, the 'nanoneedle' tip based method[94] shows the most promise, having been used by several groups to study surface tension of aerosol droplets, for example[62,63]. But, a clear drawback of this method is the need

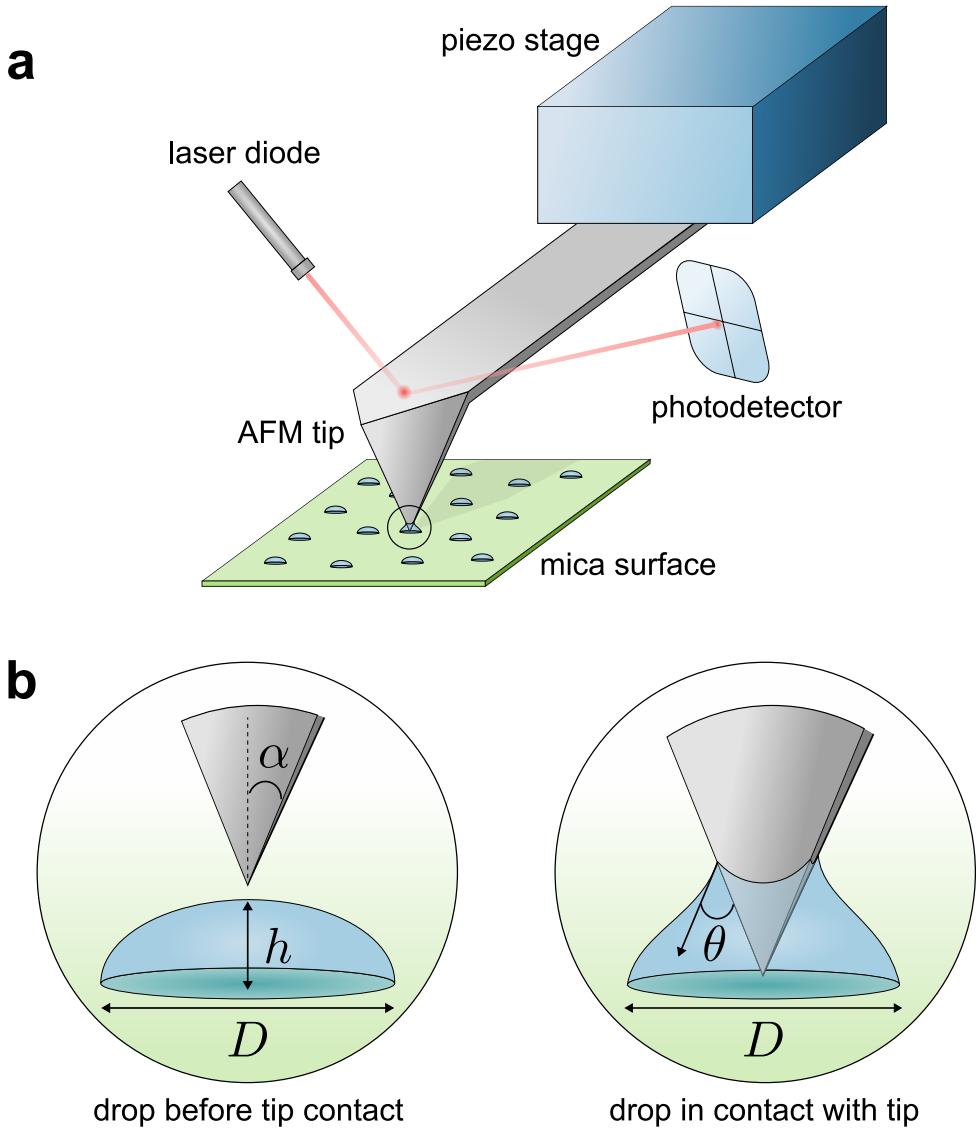

Figure 4.1.: a. Schematic of an AFM experiment on micro-droplets deposited on a mica surface. b. Magnified view showing the interaction process of the AFM tip with the liquid drop (circled region in a.). Initially, a liquid drop is pinned to the surface with contact diameter, D and height, h. During force measurement, the drop makes a contact angle, θ with the tip surface. The tip shown here has a regular square pyramidal geometry of half-angle, α.

to fabricate such nanoneedles precisely on the cantilever tip, which are not easy to prepare and would be expensive as a commercial product. Is there a way to circumvent the reliance towards such special tips and instead make similar measurements with standard pyramid shaped tips that are widely used for general AFM imaging?

Although it is possible to obtain AFM force-distance curves when a pyramid-shaped tip makes contact with a liquid droplet, there are however several challenges to calculate the desired surface tension value which is hidden within the measured force data. First, the theoretical capillary force interaction between a liquid drop and a pyramid shape can be precisely estimated only by numerical simulations, making the analysis procedure complicated[21]. Second, the surface properties and precise shape of the AFM tip significantly influences the measured force values. Small structural or chemical heterogeneities on the tip surface can lead to pinning of the liquid contact line, resulting in a different force response. In such cases, precise knowledge of liquid contact angle with the tip or point of contact line pinning is essential to make reliable numerical predictions. Fabié et. al.[34] showed that AFM force curves show a good agreement with simulations if the liquid contact line is assumed to remain pinned to the facets of a hydrophilic AFM tip at some fixed point. But for hydrophobic coated tips, the liquid contact line recedes at a certain contact angle and also undergoes pinning at multiple intermediate points when the tip is retracted away from the liquid. This complex dewetting process could not be precisely modelled and thus, it wasn't possible to obtain simulated force curves that follow the experimental curves. Hydrophilic tips may thus, in principle, be used to back-calculate surface tension of micro-droplets by fitting the obtained AFM force curves to simulation data. But an additional problem of such tips would be the continuous loss of drop volume whenever they make contact, which is an undesired side-effect of the contact line pinning as a result of large contact angle hysteresis that hydrophilic surfaces typically show. This continuous contamination of the hydrophilic tip during the measurement process would further complicate the analysis of force curves.

In order to enable the use of standard pyramidal AFM tips for surface tension measurements, it is essential to modify the tip surface such that it has a low contact angle hysteresis with any liquid that should be probed, i.e. to render the tips *amphiphobic*. This could, in principle, minimise any local pinning events or sticking of liquids when they are in contact with the tip during measurement, and thus, one could obtain force curves which closely follow the ideal theoretical scenario. While

hydrophobic coating with a fluoropolymer, for example, does reduce the hysteresis to a certain degree, they have poor anti-wetting properties to low surface tension liquids. Two common strategies to make surfaces amphiphobic is by coating them either with a nanostructured[101] or a lubricant[98] layer. Both these methods however wouldn't be suitable for our needs, since such amphiphobic layers are usually several micrometers thick which could change the tip shape, or could contaminate our sample liquids if we choose the lubricant-based coating method. Recently, it was shown that polymer brush coating can be used to obtain surfaces with very low contact angle hysteresis (less than 5°) due to the high chemical and physical homogeneity of the dense brush layer[23,64], which behaves similar to a thin lubricating liquid-like film. These polymer brushes have a nanometer-scale coating thickness, making them an ideal candidate for modifying tip surface.

In this work, I present a method to perform equilibrium surface tension measurement on micro-droplets with an AFM using standard pyramidal tips coated with a polymer brush. A simple one-step process was adapted from previously reported study[20] to obtain a hydrophilic polymer brush coating on the tip surface. The low contact angle hysteresis of the coated tip prevented liquid drops from sticking to the AFM tip despite being hydrophilic. Further, I used the *Surface Evolver* software[12] to numerically simulate the configuration of a liquid drop siting on a flat surface and interacting with a pyramid or cone shaped tip from above[21,34]. The simulated force-distance curves were compared with the experimental AFM data to calculate surface tension. My method attempts to simplify micro-scale surface tension measurements, and also help progress scientific understanding of the various processes governed by wetting phenomena on small scales.

4.3. Methods

4.3.1. Simulation scheme

The condition of a sessile liquid drop in contact with an AFM tip was simulated using *Surface Evolver* software[12]. The AFM tip was modelled to be either of a regular square pyramid or a cone geometry, with a half angle, α. The drop having a volume V of liquid with surface tension γ was assumed to remain pinned to the bottom surface, following an fixed circular contact line of diameter D. The apex

of the pyramid/cone tip was in contact with the substrate below at the centre of the drop. On the top, the drop had a constant contact angle, θ, with the AFM tip surface. Effects of gravity can safely be neglected, as droplet sizes are far below the capillary length. All lengths and forces involved were normalised w.r.t. h and γh, respectively, where h is the undisturbed height of the sessile drop without making contact with the tip (Figure 4.1 b). Gravity has a an insignificant effect on the micro-droplet shape here since the Bond number is very low. Hence, the sessile drop assumes the shape of a spherical cap and the drop volume relates to h through the analytic expression, $V = \pi h(3D^2/4 + h^2)/6$[95], which simplifies the volume normalisation. An appropriate solution routine was written in the software to "evolve" the shape of the liquid drop, starting from a polyhedron initial condition to its final equilibrium state by following successive mesh refinement and surface energy minimisation steps (script files available in the public GitHub repository `https://github.com/PranavSudersan/afm_pyramid`). In this case, the net vertical adhesion force, F_{adh}, between the tip and the liquid drop is given by:

$$F_{adh} = \Delta P_{Laplace} A_{top} + L_{top}\gamma \sin(\alpha - \theta)$$

Here, $\Delta P_{Laplace}$ is Laplace pressure difference, A_{top} is the contact area between the tip and the drop projected on the horizontal plane, and L_{top} is the perimeter of the contact line between the tip and the drop. Note that the van der Waals adhesion force between the tip and the substrate are negligible relative to the capillary force, and hence not considered. For comparison with simulation data, the above equation needs to be rewritten in the normalised inverted form:

$$\hat{\gamma} = \frac{\gamma h}{F_{adh}} = \frac{1}{\Delta \hat{P}_{Laplace} \hat{A}_{top} + \hat{L}_{top} \sin(\alpha - \theta)}$$

Here, $\Delta \hat{P}_{Laplace} = \Delta P_{Laplace} h/\gamma$, $\hat{A}_{top} = A_{top}/h^2$ and $\hat{L}_{top} = L_{top}/h$ are output parameters from the simulation, which were used to calculate the liquid surface tension, expressed in non-dimensional form as, $\hat{\gamma} = \gamma h/F_{adh}$. The simulations were iteratively repeated for a range of $\hat{D} = D/h$, θ and α values for both pyramid and cone geometries to obtain a map of non-dimensional surface tension values for a specific set of parameters. The contact angle, θ, was taken from experimentally measured values between the test liquid and a flat substrate of identical surface chemistry as the AFM tip. Since the tip is hydrophilic, θ was typically less than

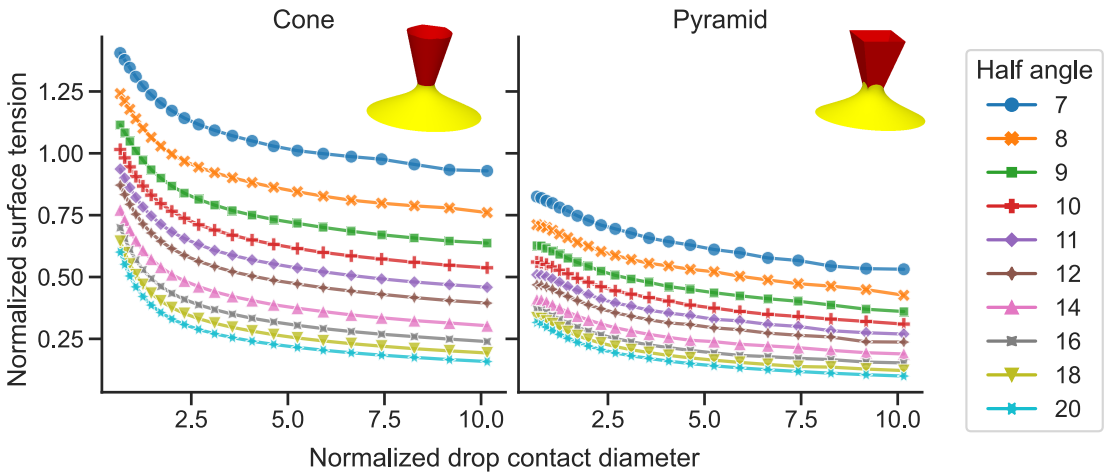

Figure 4.2.: Simulation curves showing normalised surface tension, $\hat{\gamma} = \gamma h/F_{adh}$ as a function of normalised drop contact diameter, $\hat{D} = D/h$ for cone (left) and regular square pyramid (right) tip geometries. Each curve corresponds to a specific tip half angle, α, as indicated by the different line colour and marker style. The curves correspond to a fixed tip-liquid contact angle, θ=30°. Insets show the simulation snapshots for the corresponding geometry at $\hat{D}$=5 and α=14.

30° (Figure 4.9). F_{adh}, D and h can be easily obtained by experimental AFM measurements while α can be measured by Scanning Electron Microscopy (SEM), as will be described in the subsequent sections. In this manner, the experimentally measured parameters can be utilised to calculate the liquid surface tension from the simulated $\hat{\gamma}$ values.

4.3.2. Wilhelmy plate method

Surface tension measurements were carried out on three test liquids: mineral oil (RTM-13, 75 cSt), glycerol, and ionic liquid (Trihexyltetradecylphosphonium bis (trifluoromethylsulfonyl)imide, >98%, IOLITEC GmbH, Germany). For bulk liquid measurements, I followed the Wilhelmy plate method using a commercial tensiometer (DCAT 11EC, DataPhysics Instruments GmbH, Germany) and a platinum-iridium plate of width 19.9 mm and thickness 0.2 mm. Before attaching the plate to the tensiometer's force sensor, it was rinsed in ethanol and subsequently burned with a butane torch until it glows red, thus removing any contaminants. 10 ml of test liquid was pipetted into a petri dish placed under the plate. The instrument's software control was used to bring the plate close to the liquid surface. The plate

was then partially dipped into and out of the liquid with a constant vertical speed of 0.1 mm/s while simultaneously recording the detected force values The maximum force measured while the plate is retracted out of the liquid was used together with the plate geometry values to calculate surface tension.

4.3.3. Cantilever coating

Cantilever tip model RFESPA-75 (spring constant∼3N/m, Bruker) was used for all AFM measurements. Polyethyleneglycol (PEG) chains were grafted on the cantilever tips by following the silanization method reported by Cha et. al.[20]. The cantilevers were first cleaned in an oxygen plasma chamber (Diener Electronic Femto) for 2 min at 48 W power, then subsequently placed in a solution mixture comprising 2 µL of 2-[methoxy(polyethyleneoxy)propyl] trimethoxysilane (90%, 6-9 PEG units, abcr GmbH, Germany), 8 µL hydrochloric acid (fuming, ≥37% assay, Sigma Aldrich) and 10 mL of toluene (≥99.8%, Fischer Scientific, UK). After 18 hours, the cantilevers were cleaned in an ethanol bath for 10 mins, to finally obtain PEG-brush coated hydrophilic cantilever tips. AFM experiments with the cantilever were subsequently performed within a few hours post coating. An identical cleaning and coating procedure was also performed on a flat Silicon wafer. Contact angle measurements (DataPhysics OCA 35 goniometer) of glycerol, mineral oil and ionic liquid (10 µL sample volume) were subsequently made on the resultant PEG-brush coated Silicon wafer. The measured contact angle values were used for surface tension calculation by the AFM method, as described later.

4.3.4. Droplet generation

Small micro-droplets were deposited on a freshly cleaved mica surface for AFM measurements. The droplet deposition was carried out with the help of a micropillar array of polydimethylsiloxane (PDMS) fabricated by a soft lithography procedure reported by Greiner et. al.[42]. In brief, an array of micropillars (diameter of 5 µm) was first prepared by curing a thin layer of SU8 photoresist under UV, which was used as the master template to subsequently prepare the PDMS pillar array in a two-step moulding process. The resultant PDMS array was then smeared with the test liquid, which was used to stamp small droplets on the mica surface. Drops with a size range of 5-25 µm contact diameter were obtained by following this method.

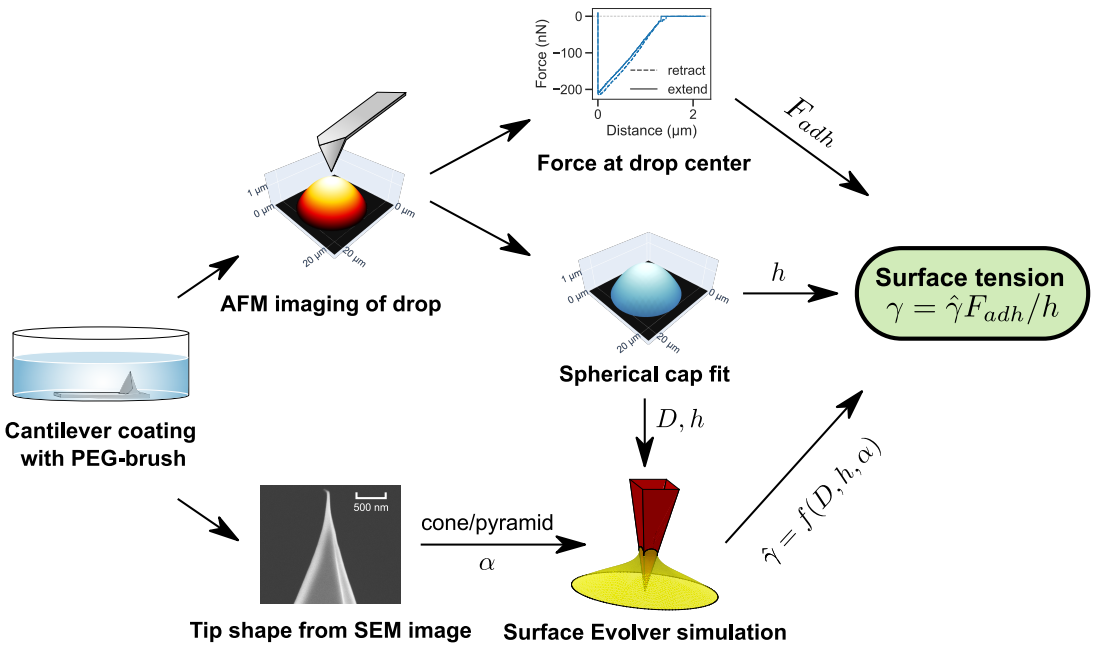

Figure 4.3.: Flowchart summarizing the procedure to measure surface tension. See text for detailed description.

4.3.5. AFM measurements

Measurements on micro-droplet liquids were performed using the JPK NanoWizard 3 AFM (Bruker) for mineral oil, glycerol and ionic liquid. A custom-made rubber gasket was fitted between the cantilever holder and mica surface during measurements to maintain the micro-droplets in a sealed environment and minimise evaporation. After loading the PEG-brush coated cantilever and the droplet carrying mica surface onto the AFM sample stage, the system was left for 60 mins to allow the droplets to equilibrate with the surrounding sealed chamber. Following the equilibration step, the droplets were imaged under intermittent contact mode (tapping mode). First, the cantilever tip was positioned close to a drop of interest with the aid of the AFM's inbuilt optical microscope. The cantilever deflection sensitivity and spring constant were then calibrated using the contact-free thermal noise calibration method[78], available within the AFM software. The cantilever was tuned to a driving frequency slightly below its resonance frequency with a specific target oscillation amplitude. Images were taken under high feedback gain and soft tapping conditions and appropriate scan line rate and area size were chosen to obtain good overlap between the height trace and retrace curves. For example, droplet

height images for glycerol were captured at a scan line rate of 0.7 Hz, scan area size of 22x22 µm with the cantilever tuned at a target amplitude of 40 nm (Figure 4.3). Since the droplet sizes were comparable to the scan area, high image resolution was unnecessary for analysis. All images were thus recorded at 128x128 pixel size to speed up the scanning process. Using the captured drop AFM image as a reference, the cantilever was precisely positioned to the centre of the drop by software control of the AFM's piezo motion stages and force spectroscopy measurements were done. Here, the cantilever tip approached and penetrated the drop, made contact with the mica surface and finally retracted back vertically out of the drop (Figure 4.1). Approach/retract speed was 0.1 µm/s. The approach/retract distance was set depending on the height of the drop, obtained from the previously captured drop image. The force trigger set-point was set to 10 nN in order to detect hard contact between the tip and the mica surface, which would then initiate the retraction cycle of the force curve. Force curves were recorded at 1000 Hz sample rate and repeated 3 times for each drop. After force measurements, the same scan area was imaged again to check for any possible loss of drop volume as a result of liquid contact with the tip or due to evaporation. Measurements were repeated with 2 independently coated cantilevers each for mineral oil, glycerol and ionic liquid, i.e. 6 cantilevers in total. For each cantilever, images and force curves of 8 drops were recorded. Thus, 16 drops were measured for every liquid.

4.3.6. Tip shape estimation

Since commercially available cantilever tips typically have tapered ends for better sharpness of the tip, the precise tip shape within the region making contact with the micro-droplet needed to be determined. Tips were imaged after droplet experiments from both front and side views using LEO Gemini 1530 Scanning Electron Microscope (1 nm point resolution, Zeiss, Germany). The cantilevers were mounted on the SEM sample holder with the help of carbon tape before imaging. The shape of the tip within 1 µm length scales close to the tip apex was specifically focused on. Tip angle was obtained by drawing straight lines following its two extreme lateral edges and measuring the angle between them using Inkscape graphics editor (Figure 4.4). The angle measured can differ depending on the region of the tip being considered, since the tip deviates from its ideal regular pyramid shape and gets sharper close to its apex. In order to simplify analysis, the tip shape was

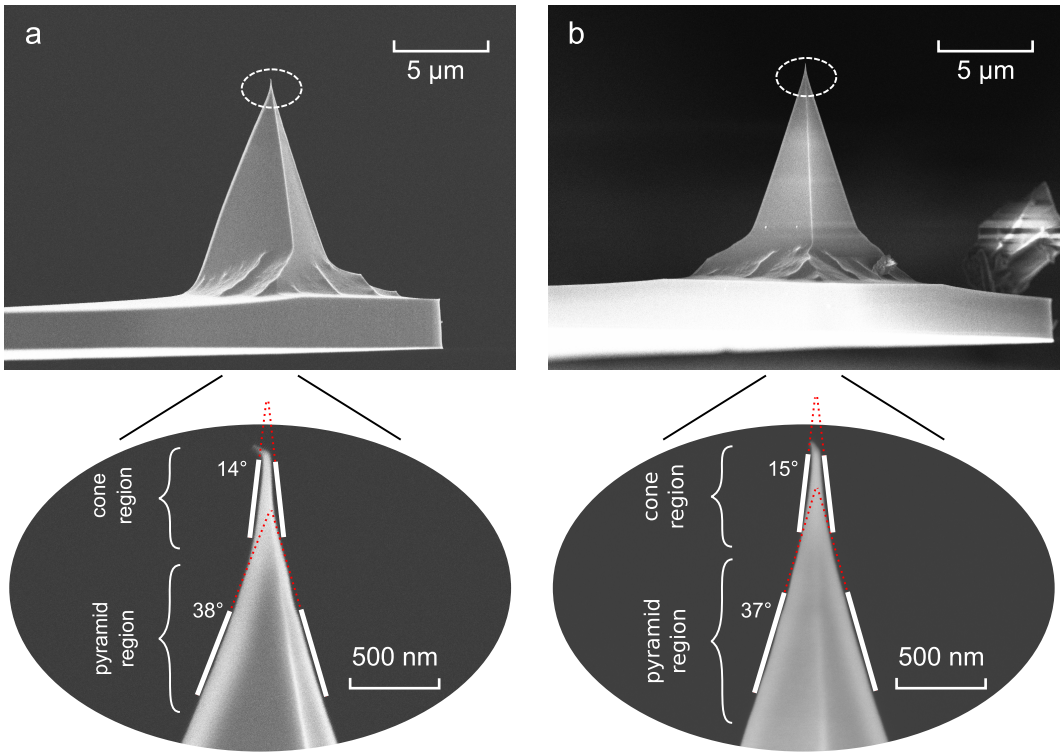

Figure 4.4.: SEM of cantilever tips (model: RFESPA-75) imaged from a) side view and b) front view. Insets show magnified images close to the tip apex (marked by the dashed ellipse), indicating a 'cone' or 'pyramid'-like tip geometry. The corresponding tip angles for each shape are marked (see text for details).

classified into two regions: 1) cone shaped very close to the apex, and 2) pyramid shaped far from the apex. A pair of lines were manually fitted on the edges for these two regions to obtain the corresponding tip angle. The above process was repeated for both front and side view images of the tip and the obtained tip angles were averaged for each shape. For the case of pyramid, the tip angles measured this way corresponds to the angle, α_{opp}, between its opposite lateral edges due to its orientation in the SEM images. Since my model defined the half-angle of the pyramid to be between its adjacent lateral edges, I use the geometric relation, $\alpha = 2\arctan\left[\left(1/\sqrt{2}\right)\tan\left(\alpha_{opp}/2\right)\right]$, to obtain the true value of α from α_{opp} measured via SEM. For RFESPA cantilever tips, the average cone half angle was $\approx$ 7°and the average pyramid half angle was $\approx$ 13°(obtained from above relation). Since our test liquid drop heights lie between the cone and pyramid regions, the exact tip shape to be considered for surface tension calculations can be ambiguous. Thus here, I consider both pyramid and cone geometries independently for further analysis.

4.3.7. Surface tension calculation

AFM measurements of drop shape and force-distance curves combined with knowledge of tip shape provides all the necessary ingredients to estimate the surface tension of the liquid drop. Here, I describe the general calculation procedure of combining experimental and simulation data to obtain surface tension (Figure 4.3):

1. The AFM height image data of each drop was fitted with a spherical cap shape. The fitted cap parameters were used to obtain the contact diameter, D, drop height, h, and volume, V.

2. The adhesion force, F_{adh}, was obtained from the minima of the retraction cycle of the force-distance curve which was measured for the corresponding drop.

3. The tip shape was considered to be both a pyramid and a cone. The corresponding tip half-angles, α, was taken to be half of the measured average angle obtained via SEM.

4. The normalised surface tension, $\hat{\gamma}$, was obtained from the simulation data using experimentally measured $\hat{D} = D/h$ and α values. Here, contact angle, θ, between the liquid and the tip was assumed based on macroscopic experi-

mental contact angle measurement of the liquid with a flat PEG-brush coated Silicon wafer substrate.

5. Finally, the surface tension was calculated in real units from the above $\hat{\gamma}$ value together with the experimentally measured F_{adh} and h values, using the relation $\gamma = \hat{\gamma} F_{adh}/h$.

The above procedure was automated in Python to directly calculate surface tension from the raw output data of JPK NanoWizard 3 AFM. Here, the 'measuredHeight' and 'vDeflection' channels of the data were used to obtain the resultant drop image and force-distance curve. The scripts used for the analysis are available in the public GitHub repository (normalized`https://github.com/PranavSudersan/afm_surface_tension`).

4.4. Discussion

4.4.1. Surface tension results

Surface tension of liquid micro-droplets obtained by AFM agree with the macroscopic measurements of the liquid using a commercial tensiometer (Figure 4.6 and Table 4.1). The precise nature of the tip shape to be considered for calculation is ambiguous, because the 'cone' and 'pyramid' regions of the tip roughly transitions at the same length scale as the drop height ($\approx$ 1 µm). Thus, the calculations were performed for both geometries. We see that the pyramid approximation gives a better estimate of surface tension for mineral oil and ionic liquid relative to their macroscopic values (<5% error). For glycerol, the cone and pyramid approximation respectively over and underestimates the surface tension within a 9% error relative to the tensiometer measurements.

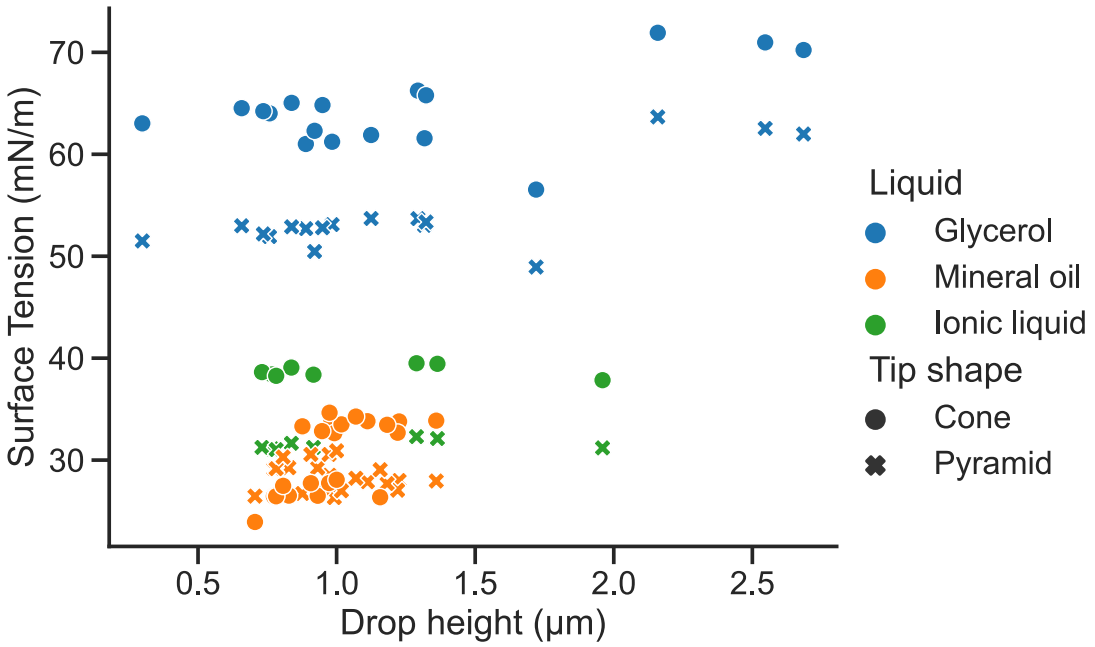

Figure 4.5.: Detailed measurement data of surface tension of several liquid droplets, calculated using the AFM method as described in the main text. Here, each point represents a measurement done on a unique liquid drop. Calculations based on cone and pyramid approximation of the tip shape are shown separately as circles and crosses respectively. Summarized results of the presented data are reported in Table 1 and Figure 4.6 of the main text.

4.4.2. Effect of tip shape

Overall, for both polar and non-polar liquids, the AFM method allows for surface tension measurement within a 10% error relative to expected values. Since the forces measured from an AFM typically has an error in the order of 5-10% due to uncertainty in spring constant determination, combined with my somewhat simplifying assumptions of the tip shape, the observed deviations are within the range expected. Simulations show a significant impact of tip half angle, α and tip shape (cone vs pyramid) on the calculated surface tension, due to the sensitive dependence of the tip characteristics on the capillary force (Figure 4.2). Thus, precise knowledge and modelling of the tip shape is crucial to obtain accurate values of surface tension. My results suggest that the pyramid shaped assumption of the tip shape could be a reasonable approximation for surface tension estimation within 10% error. The tip angles provided by the cantilever manufacturer (Bruker) correspond

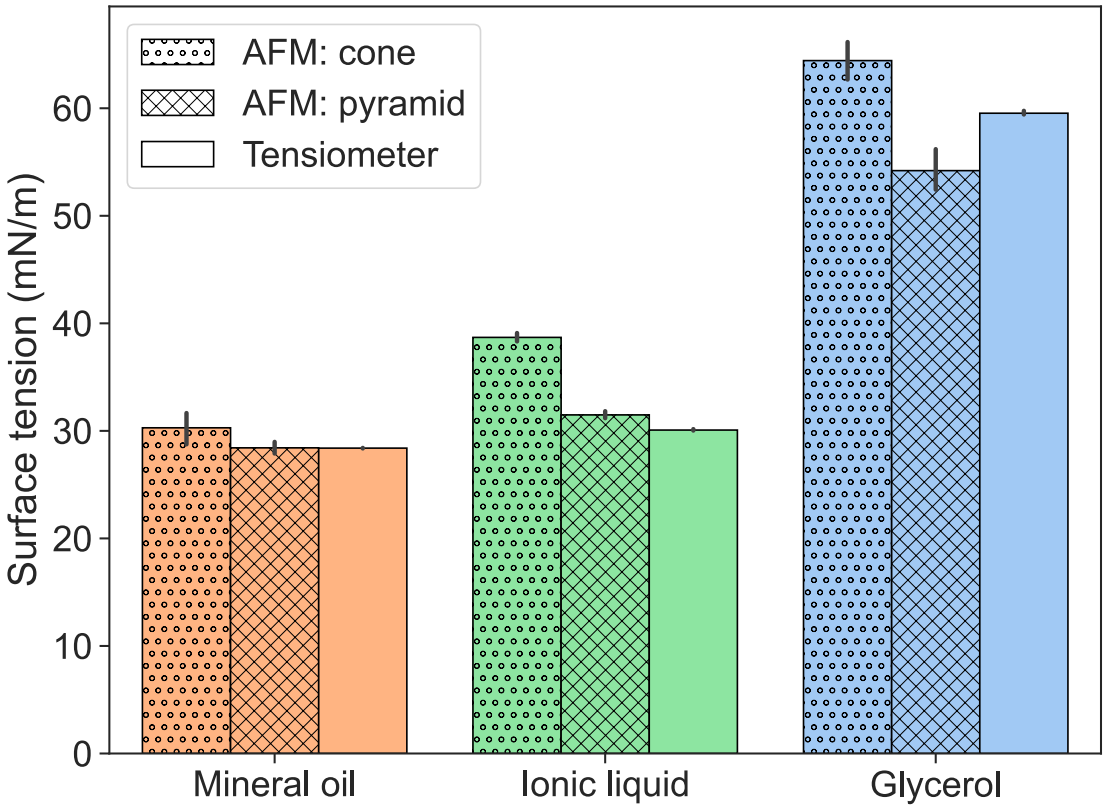

Figure 4.6.: Surface tension of various liquid micro-droplets measured using AFM as described in the present work (blue) are compared to bulk liquid measurements using a commercial tensiometer (orange). Detailed data points for individual drops are shown in Figure 4.5.

Table 4.1.: Summarised results showing the range of drop contact diameter, D, and drop volume, V, measured from AFM images. The assumed tip-liquid contact angle, θ, was used to calculate surface tension (γ_{AFM}) from AFM data for each tip shape, which are compared to macroscopic measurements ($\gamma_{Wilhelmy}$)

Liquid	D (μm)	V (fL)	θ	γ_{AFM}(mN/m)		
	[min-max]	[min-max]		Cone	Pyramid	(mN/m)
Mineral oil	9 - 17	30 - 132	10°	30.2±3.6	28.4±1.3	28.4±0.1
Ionic liquid	10 - 20	30 - 307	10°	38.6±0.5	31.4±0.4	30.1±0.1
Glycerol	5 - 25	3 - 331	30°	64.4±3.9	54.2±4.2	59.5±0.2

to the pyramid region rather than the cone region of the tip. My measurements of the tip angle ($\alpha_{opp} = 38.1 \pm 0.8°$) from SEM images, which were then used to obtain the true tip half-angle (α) for surface tension calculations, are within the value provided by the manufacturer (average $\alpha_{opp} = 37.5 \pm 2°$). Thus, one may rely on the tip angle reported in the cantilever specification sheet for further analysis, provided that the drop heights are larger than 500 nm. In this case, SEM imaging of the cantilever tip won't be necessary.

4.4.3. Role of PEG coating

The key to make the above measurements possible was the hydrophilic coating of the cantilever tip with PEG-brush. AFM force-distance curves taken at the centre of the drop confirm the quality of tip coating, as evidenced by the smooth and almost completely overlapping traces during approach and retract cycles (Figure 4.7). The low contact angle hysteresis of the coating not only minimises accumulation of liquid on the tip over repeated measurements, but also ensures that a nearly constant low contact angle is maintained between the tip and the liquid drop. This allows me to simulate the system relatively easily by assuming the ideal scenario of no contact line pinning. The low contact angle between the liquid drop and the tip also ensures a high capillary adhesion force, which minimised any errors in the force measurement due to the contribution of other attractive forces which could influence the net adhesion. For example, the van der Waals adhesion force of the tip with the hard substrate is typically less than 5 nN. This is significantly smaller than its capillary adhesion force with a liquid drop (>100 nN). Thus, van der Waals adhesion can be safely ignored. Alternative hydrophobic coated cantilevers based on polydimethylsiloxane brush[66] or fluorosilane did not work as well as a PEG-

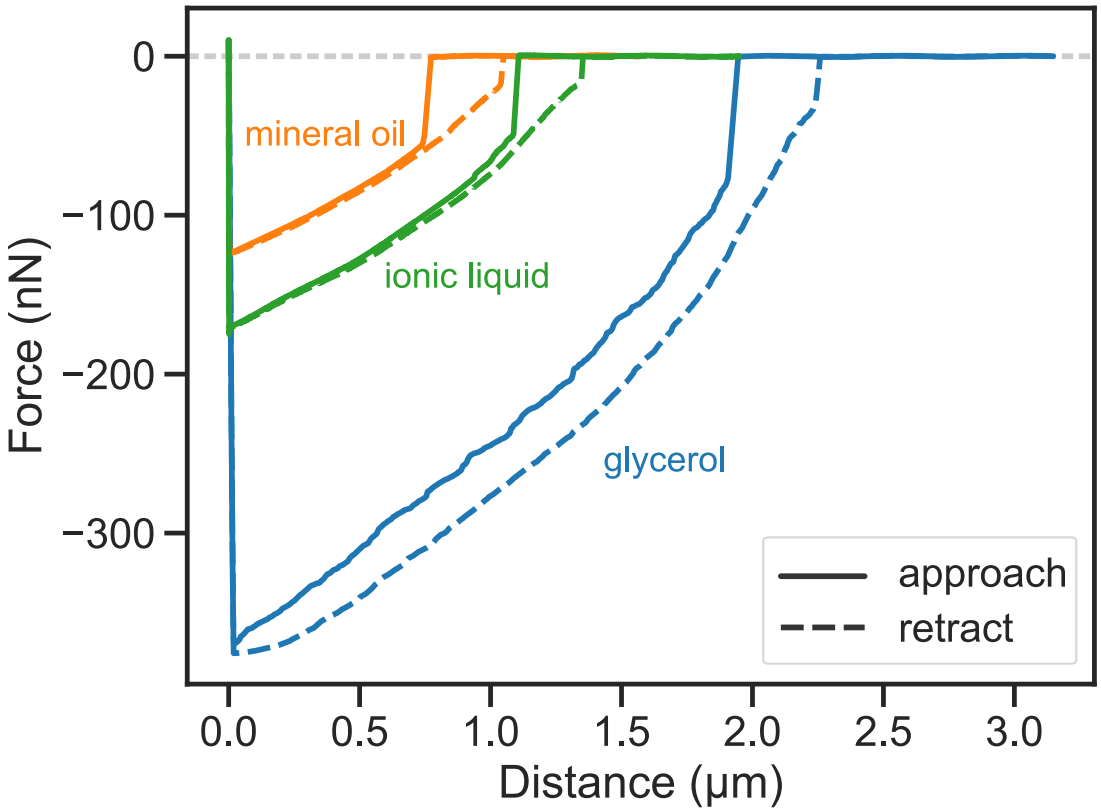

Figure 4.7.: Force-distance curves showing the interaction between a PEG-brush coated cantilever tip and a liquid droplet of mineral oil (orange), ionic liquid (green) and glycerol (blue), measured with an AFM.

brush coated cantilever due to their low capillary adhesion to liquids like glycerol and non-ideal AFM force curves resulting from contact line pinning (Figure 4.8).

4.4.4. Measurement with other coatings

Surface modification of the AFM cantilevers were performed to investigate the effectiveness of alternative coatings that are typically used to reduce the wettability of a surface. Here, I report PDMS-brush coated and fluorosilane coated cantilevers.

RFESPA cantilever tips were coated with PDMS-brush by chemical vapour deposition (CVD) method. 0.1 ml of dichlorodimethylsilane (Sigma-Aldrich) was placed in a sealed 1 Litre chamber together with the plasma treated cantilever tips for 10 minutes. The cantilevers were subsequently rinsed in toluene before AFM measurements. Similarly, fluorinated cantilever tips were also prepared by

CVD method, but under vacuum. A small cup containing 0.05 ml of 1H,1H,2H,H-perfluorooctyltrimethoxysilane (Sigma Aldrich) was placed in a 5 Litre vacuum chamber (< 100 mm Hg) for 10 minutes to fluorinate the tips by the CVD process. The tips were then heated to 150°C for 30 minutes before AFM experiments. Mineral oil and glycerol droplet preparation and subsequent AFM measurement protocol were followed exactly as described in the main text.

Force distance curves (Figure 4.8) indicate that mineral oil shows high capillary adhesion and little hysteresis when the tip is coated with PDMS-brush, which is a consequence of its low contact angle with the coated tip. Here, the approach and retract curves have a relatively smooth trend during drop contact, similar to my measurements with PEG-brush coated tips. However, for glycerol, the forces curves show a significantly non-ideal trend, with several local pinning events. The measured adhesion force in this case is also quite low, due to the large contact angle that glycerol has with the hydrophobic tip. A similar problem is also seen with the fluorinated tips, where even for mineral oil, the force curves show several pinning events as well as low adhesion. Thus hydrophobic coatings are not a good choice to obtain smooth force-distance curves with high adhesion on liquid droplets, which is necessary to reasonably model the tip-drop contact process for surface tension estimation.

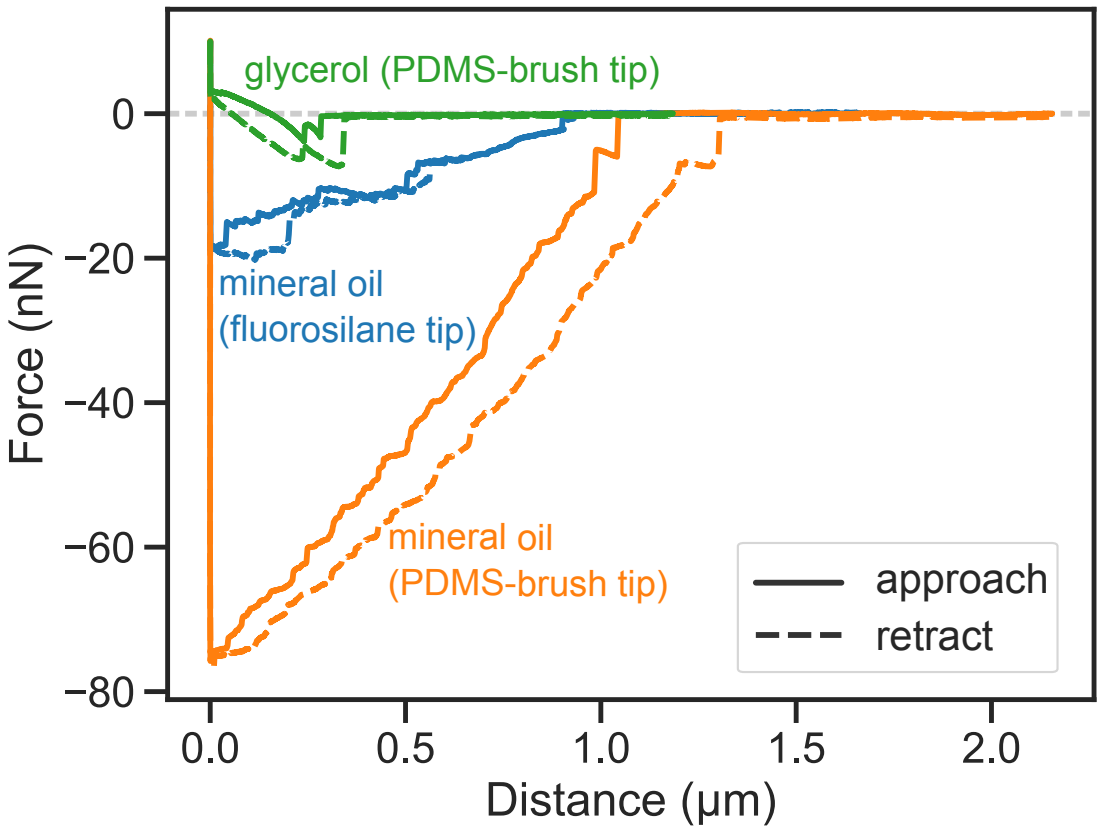

Figure 4.8.: AFM force-distance curves on liquid droplets using PDMS-brush or fluorosilane coated cantilever tips

4.4.5. Effect of tip-liquid contact angle

Macroscopic contact angle measurements on flat PEG-brush coated Silicon wafers show that mineral oil and ionic liquid spreads quite well on the coated surface, with a contact angle less than 10° (Figure 4.9). On the other hand, glycerol, which has a relatively high surface tension, showed a contact angle of ≈ 29°with the same surface. In this work, the surface tension calculations were performed by assuming the coated tip-liquid contact angle (θ) to be similar to these experimental measurements. However, our calculation method is sensitive to θ. For example, glycerol was assumed to have a θ of 30°, based on its macroscopic value, which resulted in a surface tension of 54.2±4.2 mN/m following the pyramid approximation (Table 4.1). On changing θ to 10°, the average surface tension value would however drop to 45.1±4.3 mN/m, which would correspond to a 16% measurement error relative

to its macroscopic value (Figure 4.10). In the case of mineral oil and ionic liquid, θ=10°gives a good prediction of surface tension (<2% error), since their actual contact angles are close to that value. Thus, knowledge of liquid contact angle with a PEG-brush coated flat surface is essential to improve the estimate of surface tension using AFM data.

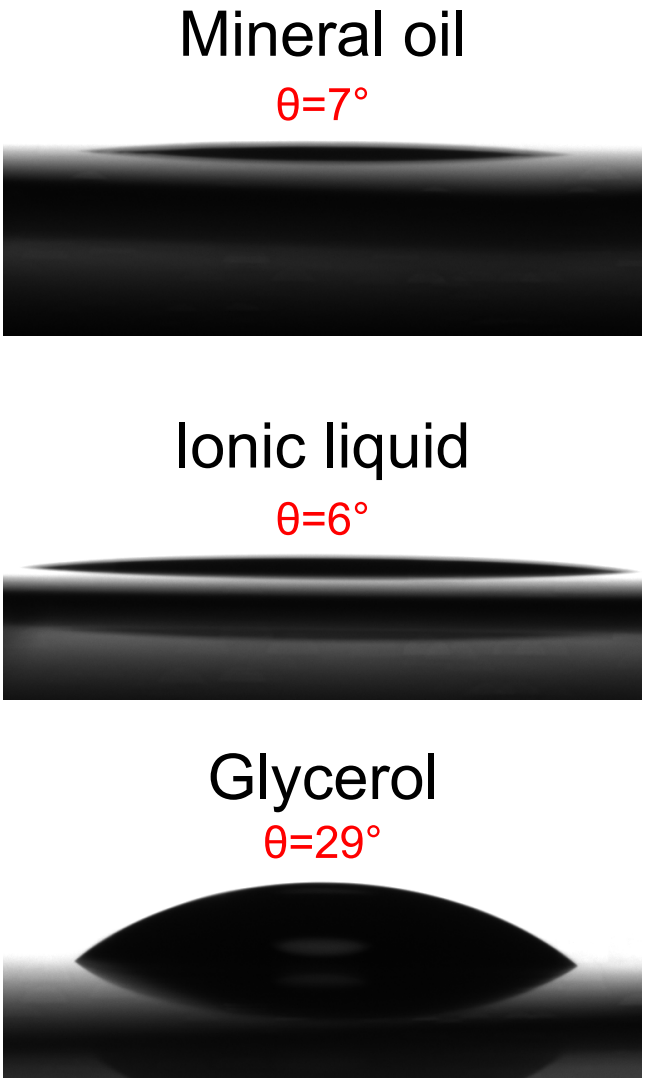

Figure 4.9.: Silicon wafer was coated with PEG-brush as described in the main text. Static liquid contact angles were measured for mineral oil, ionic liquid and glycerol.

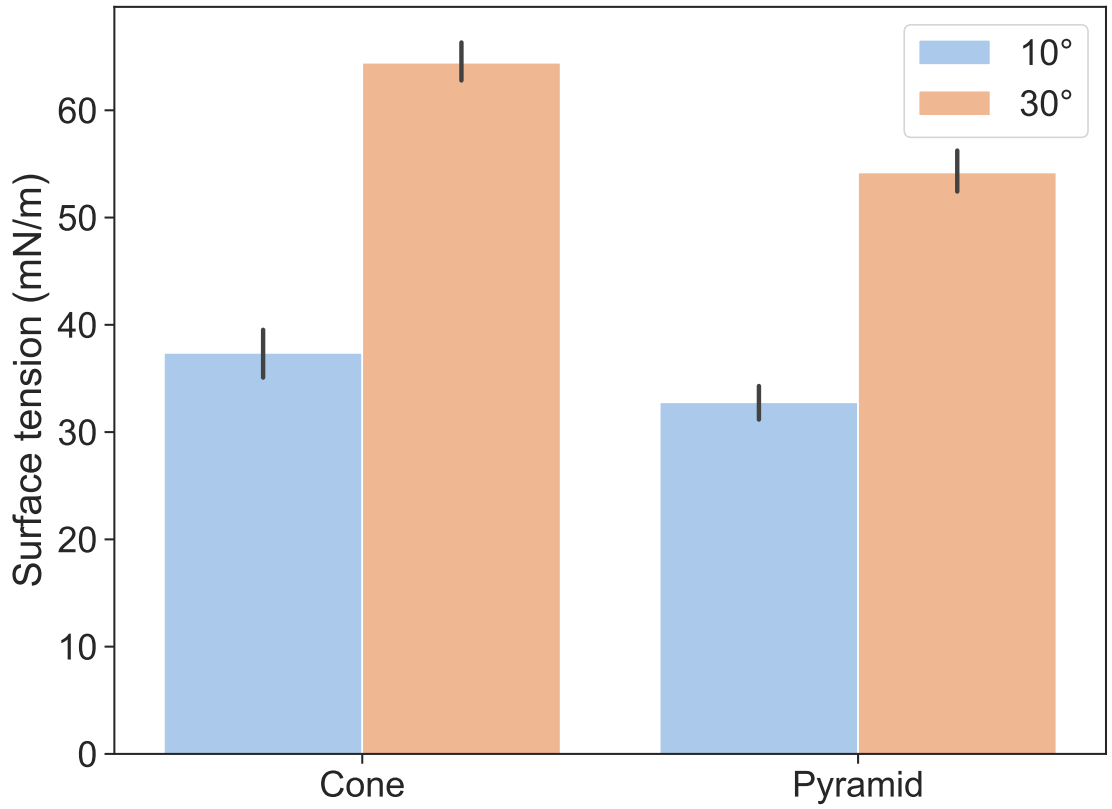

Figure 4.10.: Surface tension calculation for glycerol are shown by assuming a tip-liquid contact angle of 10°and 30°. The values are reported for both cone and pyramid tip approximations. Here, the tip is coated with PEG-brush.

4.4.6. Effect of evaporation

Micrometer-sized drops tend to evaporate fast, because of the increased vapour pressure due to their highly curved surface. To minimise evaporation I carried out my measurements in a sealed environment. Since the AFM imaging of a drop and its subsequent force measurement process can take up to 15 minutes in total, it is important to ensure that the drop does not significantly lose volume during this time. I tracked the drop evaporation by repeated AFM imaging and found less than 5% volume losses, confirming the stability of the drops during measurement (Figure 4.11). For more volatile liquids such as water, measurements need to performed under low temperature and saturated vapour conditions.

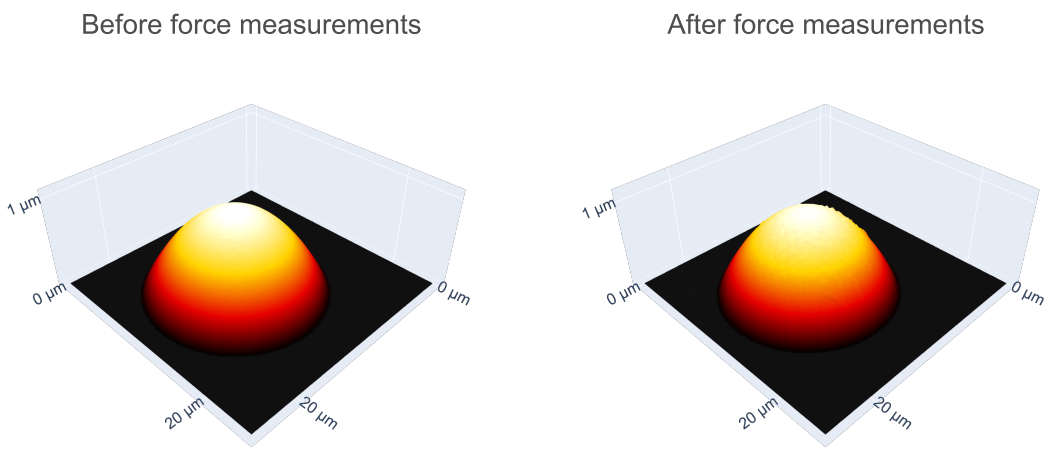

Figure 4.11.: Glycerol droplet was imaged before and after force measurements (≈10 mins apart) to track its evaporation. The drop volume does not change significantly during this time span, going from 119 fL to 114 fL (4.2% decrease). This corresponds to less than 0.1 mN/m change in calculated surface tension value. Thus, the droplet evaporation rate here can be assumed to not influence the AFM measurements.

4.4.7. Measurement on water droplets

Vapour pressure of a liquid depends on the curvature of its air-liquid interface due to the so-called Kelvin effect. This means that liquids like water become extremely volatile when they are in the form of a tiny microscopic droplet. Since the AFM measurement process takes roughly 15 minutes per scan area, it is important that the droplet does not significantly evaporate during such time scales. This may be achieved by proper control of the measurement environment, i.e., under a vapour-saturated and low temperature conditions. My attempts to perform AFM experiments on water drops using the JPK NanoWizard 4 AFM failed to give reasonable force curves (Figure 4.12). The laser spot on the cantilever head was too large that it locally heats the water drop during image scanning, even though the measurements were done under sealed saturated vapour conditions at 5°C. Further, my custom made cooling stage introduced unwanted mechanical noise into the system, overall rendering such measurements unfeasible for volatile liquids

like water.

On the other hand, my preliminary experiments using Cypher AFM (Asylum Research) gave a rather smooth and stable force curve for water droplet, showing very little hysteresis (Figure 4.12). Here, the Cypher AFM had a precisely engineered inbuilt sample chamber, where the temperature and humidity can be controlled under a sealed environment quite well without introducing noise. More importantly, the laser spot on the cantilever head was focused to a much smaller area in this particular AFM, which significantly minimised droplet evaporation during imaging and force measurements. Based on the measured force curve shown here, using the cone approximation of the tip shape, the surface tension of water was calculated to be ≈ 67 mN/m, quite close to the expected macroscopic value of 72 mN/m. Thus my reported method could potentially be extended to other volatile liquid droplets using an appropriate AFM instrument. A proper cooling system and a focused cantilever laser spot are essential for the system to inhibit droplet evaporation during measurements.

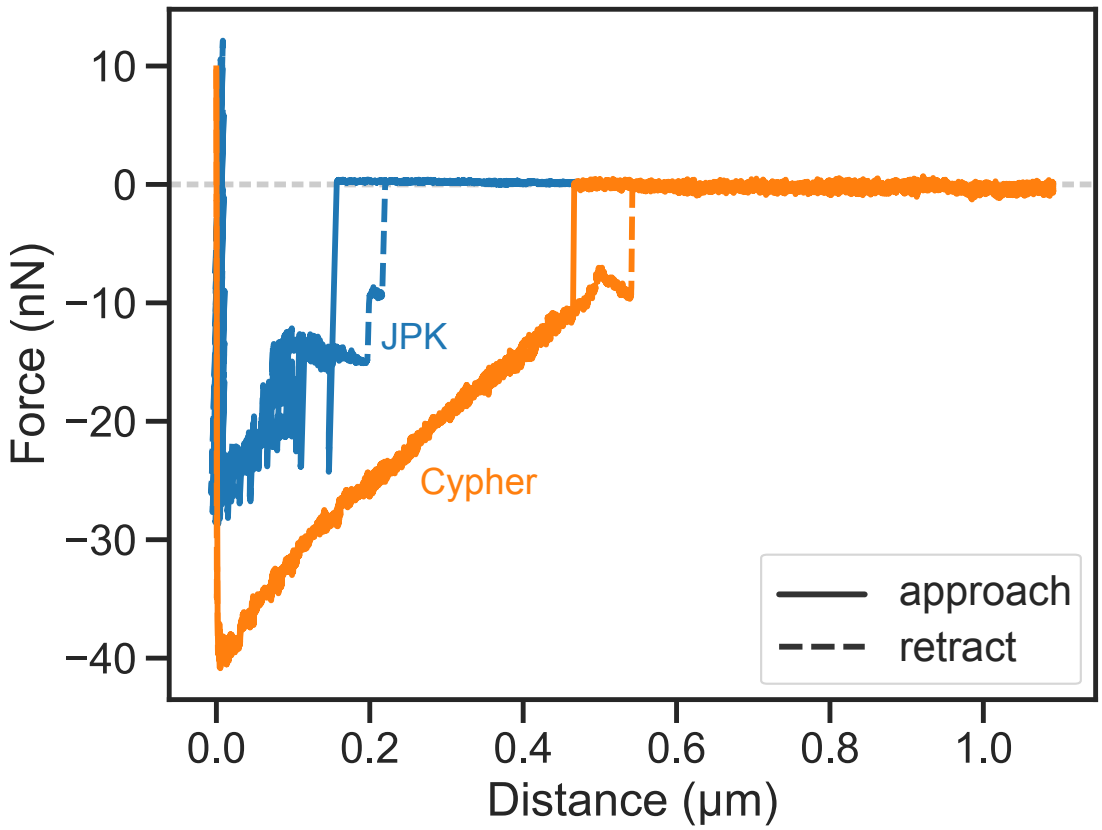

Figure 4.12.: AFM force-distance curves on water drops performed on the JPK NanoWizard 4 (Bruker) attached with a custom made sample stage cooling system (blue) and Cypher AFM (Asylum Research), which has an in-built cooling system (orange). Measurements were performed using AC200TS cantilever tips (9 N/m, 150 kHz) coated with PEG-brush.

4.4.8. Outlook

My method provides an alternative to previously reported AFM-based techniques to measure surface tension, which necessitated fabrication of specially defined tip geometries such as 'nanorods'[70] or 'nanoneedles'[99]. With such special tips, the calculation of surface tension from the measured capillary force is straightforward, since the cylindrical shape of the tip keeps the contact perimeter constant. However, fabrication of such special cantilever tips with uniform geometry is tricky and expensive. My method uses standard pyramidal tips which are used widely for general purpose AFM imaging. We need to coat the tips with a PEG-brush. This coating is, however, an easy and inexpensive one-step process, which does not

need special equipment or expertise. The relatively longer calculation procedure involved in my method has also been automated with open sourced Python scripts, making the method easily accessible to a general user.

4.5. Conclusion

In this chapter, I presented a method to measure surface tension of small liquid droplets with a volume in the order of femtoliters. Atomic Force Microscopy (AFM) was used to image the shape of liquid drops in tapping mode. In addition, AFM force distance curves were recorded with PEG-brush coated cantilever tips. Thanks to its low contact angle hysteresis, the PEG coating minimises liquid losses or pinning effects of the moving contact line over the tip, resulting in an ideal force response which could be modelled relatively easily. Further, the high surface energy of PEG allows a liquid drop to have a small contact angle with the tip, resulting in an improved measurement sensitivity due to the high capillary force. Simulations of the drop interacting with an approximated tip geometry were performed to calculate the surface tension from the experimentally measured drop adhesion force and drop shape parameters, obtained by AFM. Using the pyramidal tip approximation, the resultant surface tension values agree within a 10% error for a range of liquids when compared to macroscopic measurements using a commercial tensiometer.

5. Detachment mechanisms of hairy adhesive pads

5.1. Summary

In this chapter, I will return our focus back to the biomechanics of animal adhesion. We know that insects and some other animals can easily climb on most smooth surfaces with the help of specialised adhesive pads on their legs. But how do they control their leg's adhesion? Active locomotion can only be possible if the insect can also detach their legs easily by will after they are stuck to a surface. For the case of an animal with hairy adhesive pads, a rapid change from strong attachment to effortless detachment of the leg can be enabled by the asymmetric geometry of the tarsal hairs. Such a geometry could allow the animal to easily reorient the hairs of the pad so as to either enhance or reduce the total hair contact with the surface, and thus control adhesion. But are there some other tricks that such an animal can exploit for adhesion control? In this chapter, I will address this question by proposing some alternate mechanisms by which the hairy pad can be easily detached, even when the hairs possess no asymmetry. Here, I will examine the possible function of the tibia-tarsus leg joint and the claws. Based on a spring-based model, I consider three modes of detachment: vertically pulling the pad while maintaining either a 1) fixed or a 2) free joint, or by 3) flexing the pad about the claw. For each case, I numerically simulate the detachment process by considering each event of hair contact loss as well as the corresponding pull-off and elastic forces acting across the pad array. My proposed model illustrates the design advantage of such fibrillar adhesive systems, that not only provide strong adhesion, but also allow easy detachment, making them suitable as organs for fast locomotion and reliable hold.

The contents of this chapter is adapted from my published research article[88]. The

basic construct of the theoretical model was conceived by myself with the support of [redacted]. The derivation of model equations and the scripts used to simulate the model and generate relevant plots were written by myself.

5.2. Model

Similar to previously reported approaches[8,79], the fibrillar adhesive pad is assumed to be a one-dimensional array of N_t hairs, each behaving like a spring with spring constant, k_h, and natural length, $l_{h,0}$ (Figure 5.1). The array backing is assumed to be stiff. The pad is attached to a linearly deformable leg (tibia), assumed to be another spring with spring constant, k_l, and natural length, $l_{l,0}$. The leg is hinged to the array at a distance, s, from the right end of the array. The hinge, analogous to the tibia-tarsus leg joint of an insect, is at a vertical distance, d_s, from the surface. The hairs are spaced apart by a width, w, and the array is of length, $L = (N_t - 1)\, w$. The pad is oriented at an instantaneous angle, θ, while making contact with a flat smooth surface. Each hair can attain a maximum length, $l_{h,p}$, before pull-off, such that its pull-off force, $f_p = k_h\,(l_{h,p} - l_{h,0})$. F_{net} is the net normal force on the pad and M_{net} is the the net moment about the hinge, at a particular instant during the detachment process. I focus only on vertical detachment modes and thus lateral friction forces between the hairs and surface are not considered for my analysis.

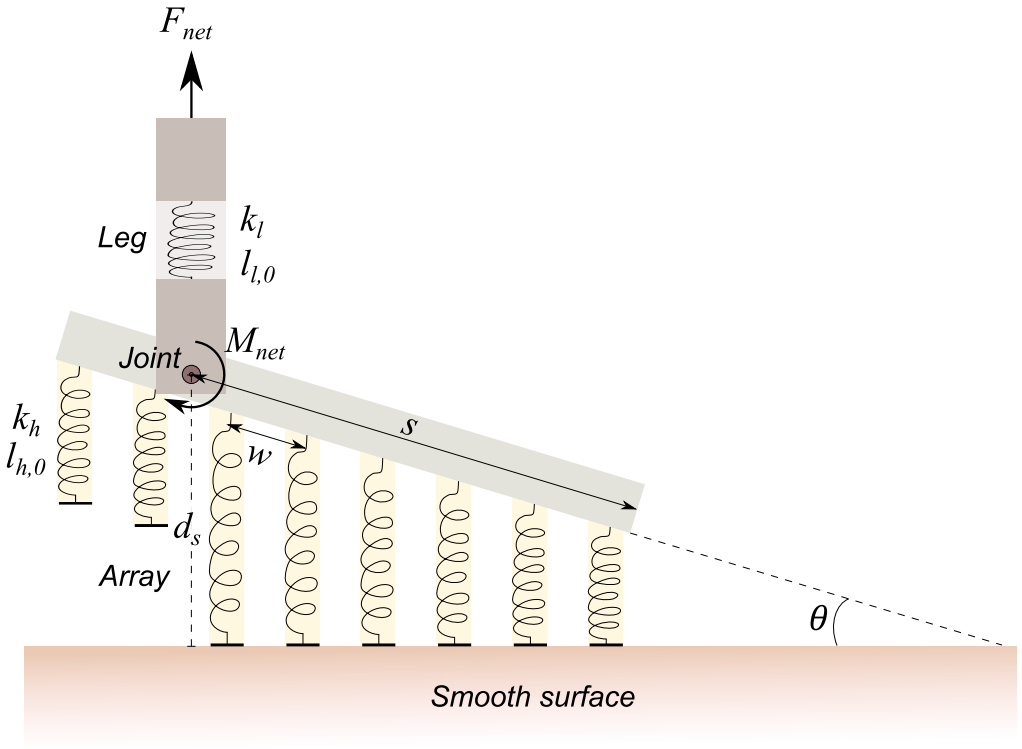

Figure 5.1.: Spring contact model of a fibrillar adhesive pad. The pad consists of an array of N_t hairs connected to a deformable leg at the joint. At a particular distance, d_s, n number of hairs are in contact and the array is oriented at a tilt angle, θ, with the surface.

Suppose at a particular instant (Figure 5.1), there are n hairs in contact with the surface. The centre of the region of the array in contact is at a vertical distance, d', from the surface. The net force on the whole array is,

$$F_{net} = \sum_{i=1}^{n} k_h \left(l_{h,i} - l_{h,0}\right)$$

$l_{h,i}$ is the length of the i^{th} hair, which is at a horizontal distance, x_i, from the centre of the contact region. By simple geometry, $l_{h,i} = d' - x_i \tan\theta$. Substituting $l_{h,i}$ in above and noting that $\sum_{i=1}^{n} x_i = 0$ by symmetry, we get:

$$F_{net} = nk_h \left(d' - l_{h,0}\right)$$

From geometry, d_s and d' is related as:

$$\frac{d_s}{\sin\theta} - \frac{d'}{\sin\theta} = s - \frac{(n-1)\,w}{2}$$

Substituting for d', the net force, F_{net}, on the pad as a function of distance, d_s, is:

$$F_{net} = nk_h \left[d_s - l_{h,0} - \left[s - \frac{(n-1)\,w}{2} \right] \sin\theta \right]$$

Simplifying, we get:

$$F_{net} = nk_h \left[d_s - l_{h,0} - \Psi \sin\theta \right] \tag{5.1}$$

where, $\Psi = s - \frac{n-1}{2} w$. For a particular value of n, equation (5.1) is valid until a certain distance, $d_{s,max}$, above which the left most hair will detach. Just before detachment, this hair will be at its maximum length, $l_{h,p}$. We can derive $d_{s,max}$ by considering the situation just before the left most hair is about to detach (Figure 5.1). This hair will be at its maximum length, $l_{h,p}$. Once again from geometry, we see that $d_{s,max}$ and $l_{h,p}$ is related as:

$$\frac{l_{h,p}}{\sin\theta} - \frac{d_{s,max}}{\sin\theta} = (n-1)\,w - s$$

Substituting $l_{h,p} = \frac{f_p}{k_h} + l_{h,0}$ in above and simplifying, we get:

$$d_{s,max} = l_{h,0} + \frac{f_p}{k_h} + \left[s - (n-1)\,w \right] \sin\theta \tag{5.2}$$

Equation (5.1) will be valid for $d_s \leq d_{s,max}$.

The maximum possible adhesion of the array would be the case when all hairs detach simultaneously ($\theta = 0°$):

$$F_{max} = N_t f_p \tag{5.3}$$

The net moment, M_{net}, about the joint can be similarly derived (see Appendix B):

The net moment about the joint due to the deformed hairs of the array is,

$$M_{net} = \sum_{i=1}^{n} \lambda_i k_h \left(l_{h,i} - l_{h,0} \right) \cos\theta$$

Here, $\lambda_i = s - \left(\frac{n-1}{2}w - \frac{x_i}{\cos\theta}\right)$ is the length of the lever arm between the i^{th} hair and the joint.

Substituting for $l_{h,i}$ and eliminating d' as before, we get:

$$M_{net} = \sum_{i=1}^{n} k_h \cos\theta \left[s - \left(\frac{n-1}{2}w - \frac{x_i}{\cos\theta}\right)\right] \left[d_s - \left(s - \frac{(n-1)\,w}{2}\right)\sin\theta - x_i \tan\theta - l_{h,0}\right]$$

To calculate $\sum_{i=1}^{n} x_i^2$, we follow:

$$\sum_{i=1}^{n} x_i^2 = 2\sum_{i=1}^{\frac{n}{2}} x_i^2 = 2\sum_{i=1}^{\frac{n}{2}} \left[w\cos\theta\left(i - \frac{1}{2}\right)^2\right] = 2w^2\cos^2\theta \left[\sum_{i=1}^{\frac{n}{2}} i^2 - \sum_{i=1}^{\frac{n}{2}} i - \sum_{i=1}^{\frac{n}{2}} \frac{1}{4}\right]$$

Using the identities $\sum_{i=1}^{N} i^2 = \frac{N(N+1)}{2}$ and $\sum_{i=1}^{N} i^2 = \frac{N(N+1)(2N+1)}{6}$ and simplifying, we get $\sum_{i=1}^{n} x_i^2 = n\left(\frac{n^2-1}{12}\right)w^2\cos^2\theta$. This, together with $\sum_{i=1}^{n} x_i = 0$ (by symmetry), the expression for M_{net} above can be simplified to get:

$$M_{net} = nk_h\cos\theta \left[(d_s - l_{h,0})\left[s - \frac{(n-1)\,w}{2}\right] - \left\{\left[s - \frac{(n-1)\,w}{2}\right]^2 + \frac{n^2-1}{12}w^2\right\}\sin\theta\right]$$

Expressing the above in a simplified form by substituting for Ψ, we finally get:

$$M_{net} = nk_h\cos\theta \left[(d_s - l_{h,0})\,\Psi - \left\{\Psi^2 + \frac{n^2-1}{12}w^2\right\}\sin\theta\right] \tag{5.4}$$

Let us now consider the scenario where even the leg above the joint can undergo elastic stretching together with the hairs. When a hair detaches from the surface, the leg undergoes an elastic recoil due to the stored elastic energy. Suppose the leg relaxes upward by a recoil length, Δl, at the point of the joint. For n hairs in contact, when a hair detaches, the array's tilt angle will change from initial θ_b to θ_a as a result of joint rotation. The i^{th} hair of the array thus deforms by Δl_i, which by geometry, is derived as:

$$\Delta l_i = \Delta l + iw\,(\tan\theta_a - \tan\theta_b) \tag{5.5}$$

The force balance before and after a hair detaches is thus given respectively by:

$$\sum_{i=1}^{n} k_h \left(l_{h,i} - l_{h,0}\right) = k_l \left(l_l - l_{l,0}\right)$$
$$\sum_{i=1}^{n-1} k_h \left(l_{h,i} + \Delta l_i - l_{h,0}\right) = k_l \left(l_l - \Delta l - l_{l,0}\right)$$

Solving the above two equations with equation 5.5 for Δl, we get:

$$\Delta l = \frac{f_p - k_h w (n/2)(n-1) \left(\tan\theta_a - \tan\theta_b\right)}{k_h \left(n-1\right) + k_l} \tag{5.6}$$

Thus, d_s shifts by Δl in equations 5.1 and 5.4 at each event of hair detachment (i.e. when $d_s = d_{s,max}$).

I express the forces and distances in non-dimensional forms, as below:

$$\hat{f}_p = \frac{f_p}{k_h w}, \quad \hat{F}_{net} = \frac{F_{net}}{k_h w}, \quad \hat{d}_s = \frac{d_s - l_{h,0}}{w}, \quad \hat{s} = \frac{s}{L}$$

Here, $\hat{f}_p$ is a parameter which encapsulates the hair's adhesion force, stiffness and array density. Unless specified, positive force values represent attraction by convention. Python scripts were written to solve the above equations under specific detachment conditions (available in the public repository `https://github.com/PranavSudersan/paper-effect_of_tilt/blob/main/codes/Fibrillar%20adhesion%20-%20Effect%20of%20tilt.ipynb`)

5.3. Detachment mechanisms

I consider three tentative scenarios to detach the adhesive pad from a surface: 1) *Fixed pull*, where the pad is pulled vertically up while keeping a fixed joint; 2) *Free pull,* where the pad is pulled vertically up while keeping the joint free to allow rotation of the array; 3) *Flex*, where the pad is hinged to an external point (claw-hinge), and detached in a rotary fashion, emulating the claw function in insects. To investigate each case in detail, let us assume a pad to be a one-dimensional analogue of a dock beetle's adhesive pad[14,15] with $N_t = 25$ hairs and $\hat{f}_p = 0.1$ (see discussion on *detachment pathways* for details) attached to a stiff leg (or tibia) with $k_l \to \infty$. The situation of a soft leg with $k_l/k_h = 10$ is also considered for the first two cases involving vertical detachment.

5.3.1. Fixed pull

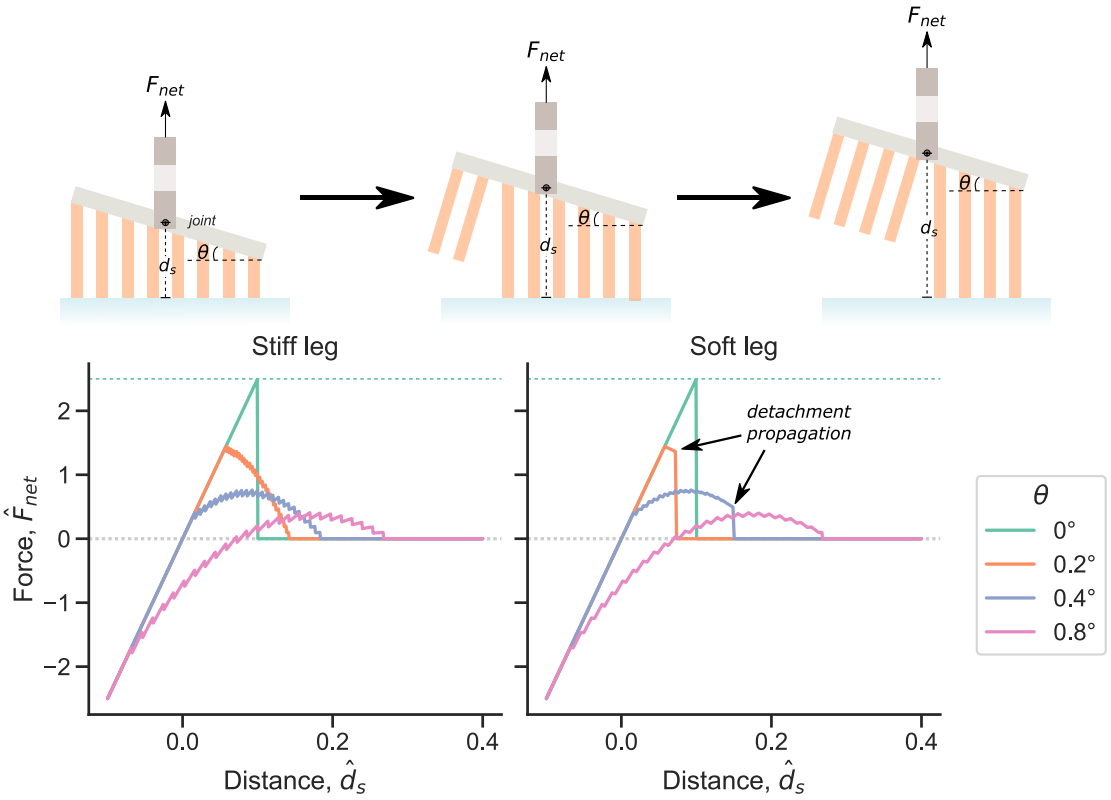

Figure 5.2.: Detachment by *Fixed Pull*. Force-distance curves for a fibrillar adhesive pad, pulled vertically upwards with a fixed joint. The tilt angle, θ, of the array is kept fixed during detachment. The leg (tibia) is either stiff ($k_l \to \infty$) or soft ($k_l/k_h = 10$). Positive force values represent attraction between the array and the surface. The green dashed line represents the maximum possible adhesion for the pad. All values are normalised to dimensionless forms, as described in text.

The fibrillar adhesive pad can be detached by pulling it vertically upwards while maintaining a constant tilt angle, θ, with the surface. This can be achieved if the joint is kept fixed. Equations 5.1, 5.2 and 5.3 can be used to get the resulting force-distance curves for such a scenario. To summarise the numerical procedure in brief, I start with an initial $n = 25$ hairs. F_{net} is then calculated for increasing d_s, until $d_s = d_{s,max}$, upon which n value is decremented by 1. The above process is repeated for increasing d_s until $n = 0$, indicating complete detachment. For the case of the soft leg, on each instance when n is decremented, d_s is increased by an additional Δl value (equation 5.6) in order to account for the recoil effect of the

leg.

Increasing the tilt of the pad decreases its maximum force or adhesion (Figure 5.2). Tilting the pad causes an inhomogeneous deformation of hairs, where, on one end they are stretched, while, on the other end they are compressed. The balance of the respective attractive and repulsive elastic forces of the hairs ultimately results in a decrease in the net force. The tilted orientation also causes the individual hairs to detach distinctly rather than simultaneously, further reducing the maximum adhesion of the array. I term this effect of loss in adhesion due to a non-uniform hair deformation across the array as *elastic weakening*. When there is no tilt ($\theta = 0°$), all the hairs undergo identical deformation and ultimately detach simultaneously after a distance, $\hat{d}_s = 0.1$. Here, no *elastic weakening* occurs and the pad shows the maximum possible adhesion.

For the case of a stiff leg (tibia), we see that at small distances, all hairs of the pad are in contact with the surface, resulting in a linear force response. On further pulling, the hairs will start to detach sequentially from left to right, indicated by a characteristic saw-tooth jitter in the force curves. The pad with a higher tilt angle initiates hair detachment first, in comparison to a pad with a lower tilt.

For the case of a soft leg (tibia), we observe a similar effect of tilt angle on the force curves as before. The maximum adhesion force at a particular tilt is the same as that for the stiff leg. The saw-tooth jitter are however minimised due to the leg's deformation, leading to a dampened force response. Interestingly, the force abruptly drops to zero for the angles 0.2° and 0.4°. This is an effect of the elastic recoil of the leg while each hair loses contact during the detachment process (equation (5.6)). The length difference between the detached hair just before it breaks contact and its adjacent hair is $w \sin\theta$. If the leg's recoil length, $\Delta l > w \sin\theta$, the adjacent hair will be stretched more than its maximum length ($l_{h,p}$), and thus will also detach, leading to further recoil of the leg. Equation (5.6) shows that Δl increases with every subsequent loss of hair contact if θ is kept constant (i.e. $\theta_b = \theta_a$). This implies that, once initiated, the leg's recoil will always be large enough to detach every remaining hair, resulting in a spontaneous propagation of the detachment front until the pad completely breaks contact with the surface. This is consistent with a recent report of catastrophic failure, due to a similar recoil effect of the measurement system, seen in micro-fibrillar adhesives with a narrow variance of individual fibril adhesive strengths[45].

5.3.2. Free pull

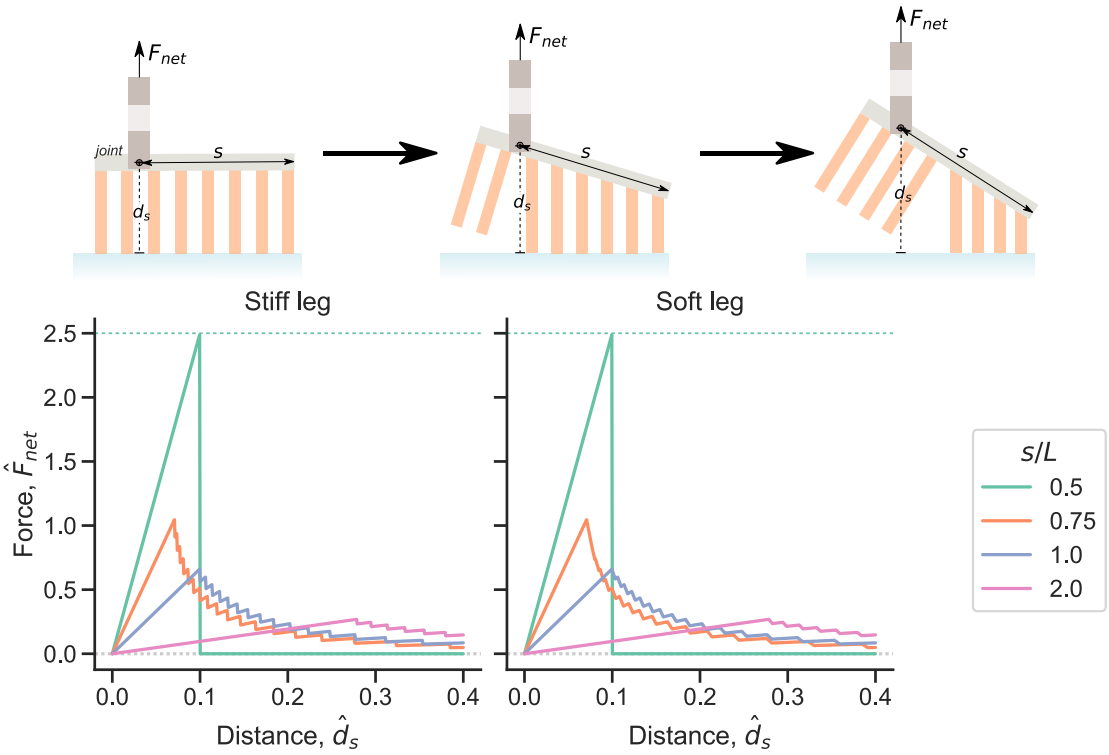

Figure 5.3.: Detachment by *Free Pull*. Force-distance curves for a fibrillar adhesive pad, pulled vertically upwards with a free joint. s is the distance between the joint and the right end of the array and L is the array length. The free joint allows further tilting of the array during the vertical pull. The leg (tibia) is either stiff ($k_l \to \infty$) or soft ($k_l/k_h = 10$). Positive force values represent attraction. The green dashed line represents the maximum possible adhesion for the pad. All values are normalised to dimensionless forms, as described in text.

Similar to the previous case, I once again consider the situation where the adhesive pad is pulled vertically upwards for detachment. However now, the joint is assumed to be freely movable. In this case, the array will reorient itself to maintain a zero net moment about the joint during the entire detachment process. At any given instant, the tilt angle, θ, can be found by setting M_{net} to zero in equation (5.4) to get:

$$\theta\left(\hat{d}_s, n\right) = \arcsin\left[\frac{\left(\hat{s} - \frac{n-1}{2}\right)\hat{d}_s}{\left(\hat{s} - \frac{n-1}{2}\right)^2 + \frac{n^2-1}{12}}\right] \tag{5.7}$$

Using the above relation together with equations 5.1, 5.2 and 5.3, we can find force-distance curves during a free vertical pull of the adhesive pad. A similar numerical procedure as *fixed pull* is followed here. Since the position of the joint will influence the net moment, I use the ratio, s/L, to study its effect on the detachment forces.

Maximum adhesion is seen when the joint is positioned at the centre of the array, i.e. $s/L = 0.5$ (Figure 5.3). Here, the net moment due to the hairs is balanced by symmetry and the array remains parallel to the substrate until all hairs detach simultaneously at $\hat{d}_s = 0.1$. Shifting the position of the joint further away from the array centre leads to lower forces or adhesion. The resulting moment imbalance will tilt the array, which reduces the net force due to the *elastic weakening* effect, as described in the previous section. Higher s/L increases the net moment to be balanced, leading to a higher tilt of the array and thus lower net force.

The force curves look qualitatively different compared to the previous case of *fixed pull*. A sharp maxima is seen, coinciding with the point when the first hair detaches. Beyond this, the force starts to decrease sharply and once again shows the characteristic saw-tooth jitter as the subsequent hairs detach in sequence. Nearly identical trend is seen for both a stiff and a soft leg (tibia). The elastic recoil of the leg does slightly reduce the amplitude of the jitter for the soft leg case. However, no abrupt drop in the force is seen like before. As the hairs detach, the array gets tilted more and more (i.e. $\theta_b < \theta_a$), making it less likely for the recoil length, Δl, to exceed $w \sin \theta_a$ and detach the next adjacent hair. Thus here, we don't see any propagation of the detachment front when the leg is soft.

5.3.3. Flex

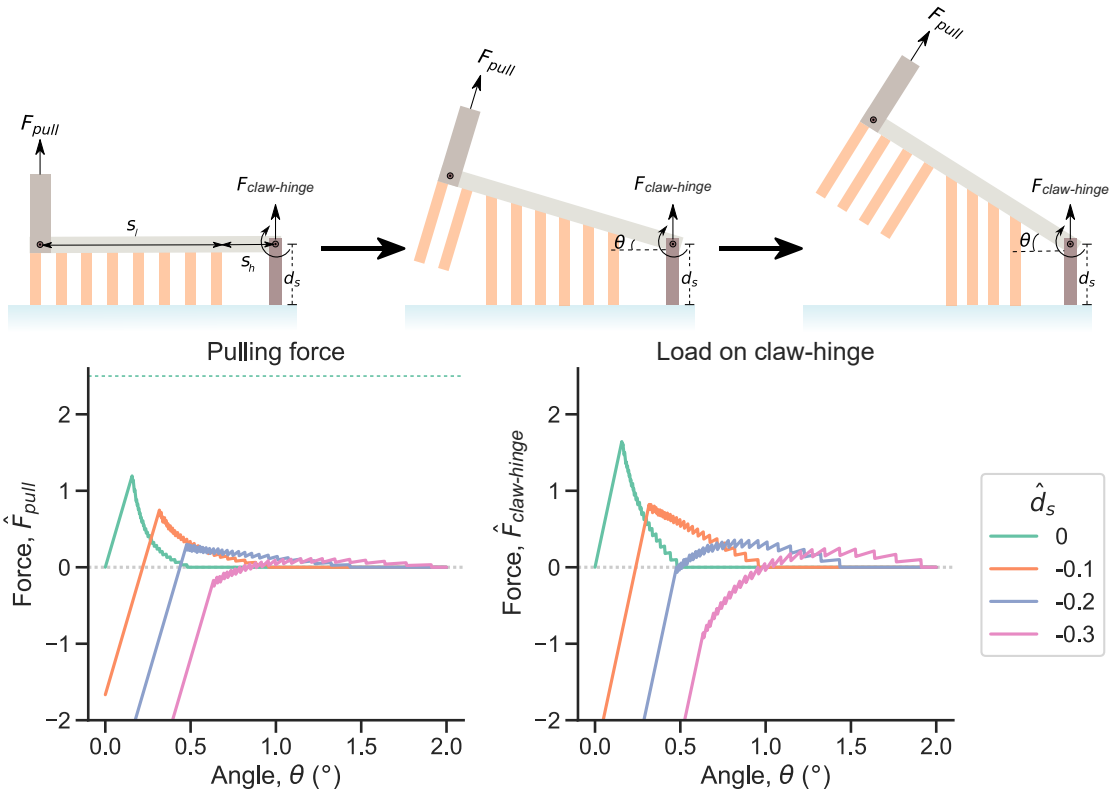

Figure 5.4.: Detachment by *Flex*. Force curves for a fibrillar adhesive pad detached by flexing it about the claw. $\hat{F}_{pull} = \frac{F_{pull}}{k_h w}$ is the normalised pulling force necessary to apply the moment about the claw-hinge for detachment, $\hat{F}_{hinge} = \frac{F_{hinge}}{k_h w}$ is the normalised reaction force on the claw-hinge, $\hat{d}_s = \frac{d_s - l_{h,0}}{w}$ is the normalised vertical distance of the claw-hinge from the surface. Here, $s_l/L = 1$ and $s_h/w = 10$. The green dashed line represents the maximum possible adhesion for the pad.

Instead of a vertical pull, the adhesive pad can also be detached by rotating it about the claw-hinge, located outside the array. Such a mode of detachment will be driven by a moment applied by the leg (tibia) to rotate the pad around the claw-hinge until all the hairs lose contact. Let s_h be the distance between the claw-hinge and the right end of the array; s_l be the distance between the joint and the right end of the array. The joint is assumed to be fixed here. To illustrate the mechanism, let us fix $s_l/L = 1$ (here, $L = 24w$) and $s_h/w = 10$ and vary the vertical claw-hinge distance, d_s. At any particular instant, the pulling force applied by the leg, $F_{pull} = M_{net}/(s_l + s_h)$, where M_{net} is obtained by setting $s = -s_h$ in equation (5.4).

Equation (5.1) will give us the reaction force acting on the claw-hinge, $F_{claw-hinge}$.

Decreasing the vertical claw-hinge distance reduces the pulling force necessary to undergo detachment by flexing (Figure 5.4). One can imagine that initially, when the array is parallel to the surface, a lower value of d_s means the hairs are in a more compressed state. When the pad is subsequently rotated around the claw-hinge, the tilted array will once again lead to an *elastic weakening* effect due to the inhomogeneous deformation of hairs. This results in a decrease in the net moment and thus lower F_{pull} for smaller values of d_s. F_{pull} can be further reduced of course by increasing the lever arm $(s_l + s_h)$.

Detachment by flexing requires that the claw remains fixed and stable during the process. We see that generally, the normal load, acting on the hinge, $F_{claw-hinge}$, follows a similar trend as F_{pull} (Figure 5.4). For low values of d_s, $F_{claw-hinge}$ goes to negative values, implying that the claw should stick well with the surface, perhaps by mechanical interlocking, to resist this negative load. As the detachment progresses however, the array starts to exert a positive load on the claw.

5.4. Discussion

In order to characterise how a particular detachment mechanism influences the adhesion of the pad, I introduce a parameter, *reduction factor*, defined as:

$$r = \frac{N_t f_p}{F_{adh}} \tag{5.8}$$

Here, F_{adh} is the adhesion force required to detach the pad from the surface following a given mechanism and $N_t f_p$ is the maximum possible adhesion of the pad (equation (5.3)). Reduction factor, r, represents the extent to which the adhesion can be reduced by choosing the mode of detachment. A large value of r implies that adhesion can be reduced by a greater factor, and this mode is more suitable to easily detach.

5.4.1. Effect of $\hat{f}_p$:

The dimensionless parameter, $\hat{f}_p = \frac{f_p}{k_h w}$, governs the strength and compliance of the array, where, high values represent a dense array of strongly adhering soft hairs.

Let us consider the case of an adhesive pad with $N_t = 25$ hairs and look at how $\hat{f}_p$ influences the reduction factor under each mode of detachment (Figure 5.5).

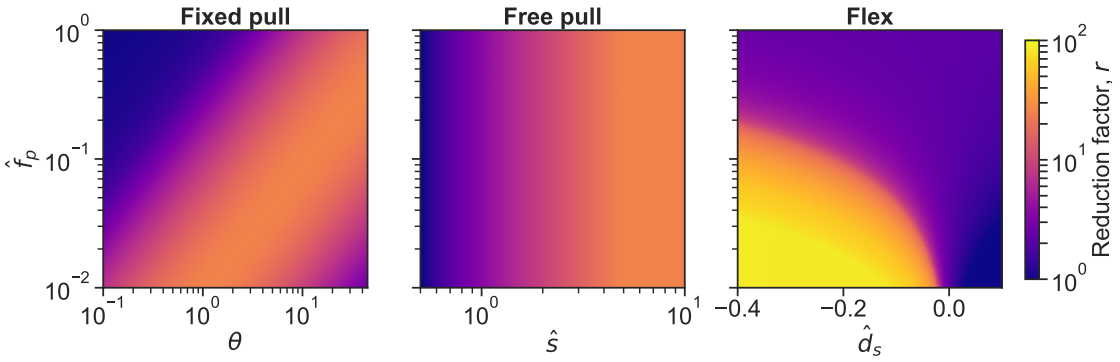

Figure 5.5.: Effect of $\hat{f}_p$ on reduction factor. Colour plots showing the effect of the dimensionless parameter, $\hat{f}_p$, on the reduction factor for each mode of detachment. Here, I fix the number of hairs, $N_t = 25$. The dimensionless parameters $\hat{d}_s = \frac{d_s - l_{h,0}}{w}$ and $\hat{s} = \frac{s}{L}$, as described in text.

When detachment follows the *fixed pull* method (Figure 5.5), for a constant $\hat{f}_p$, the reduction factor increases with increasing tilt angle, θ, and then decreases, showing a maximum r of 25 at an intermediate θ. Higher values of $\hat{f}_p$ shifts this maximum point to higher values of θ. This trend relates to the *elastic weakening* effect discussed before. Smaller values of θ bring a proportion of hairs under compression, reducing the adhesion and thus increasing r. On further tilting the array, eventually the proportion of stretched hairs will overcome the ones under compression, which ultimately reduces r at high θ. When the individual hairs show strong adhesion (i.e. for high $\hat{f}_p$), a greater tilt is necessary to bring the net adhesion of the array down.

For the case of detachment via *free pull*, $\hat{f}_p$ has no influence on the reduction factor. On the other hand, shifting the position of the joint further away from the array (i.e. high s/L) results in large values of r. In this scenario, the higher moment exerted by the array leads to a higher tilt, and thus increases the reduction factor via *elastic weakening*, saturating to the maximum value of 25.

For detachment by *flexing*, the reduction factor increases for higher initial compression of hairs (low $\hat{d}_s$). The pad notably shows a much higher reduction factor at low values of $\hat{f}_p$ and $\hat{d}_s$, with values as high as 100. Since this mode of detachment is driven by moment, the pulling force necessary to provide the moment can be

decreased without any limit simply by having a long lever arm ($\hat{s}_l$), i.e., with the joint positioned farther away from the array. In contrast, for the previous cases of *free pull* and *fixed pull*, the reduction factor is capped to the maximum number of hairs in the array ($N_t = 25$). Here, *elastic weakening* can only reduce the array's adhesion force from N_t hairs down to a single hair at most.

5.4.2. Effect of N_t:

Let us now fix $\hat{f}_p = 0.1$ and investigate the influence of the number of hairs, N_t, on the reduction factor (Figure 5.6). The colour plots show that high N_t increases r irrespective of the mode of detachment. Under a tilted state, more hairs are compressed when N_t is high, which reduces the net adhesion. This highlights another advantage of having a split contact design found in many biological systems. A design comprising of a large number of hairs not only enhances the adhesion due to scaling effects[55], but could also offer a better control over adhesion, making it quite suitable for reversible attachment and detachment during locomotion. The specific trends of reduction factor for each mode of detachment can be understood by similar arguments of *elastic weakening*, as discussed in the previous section.

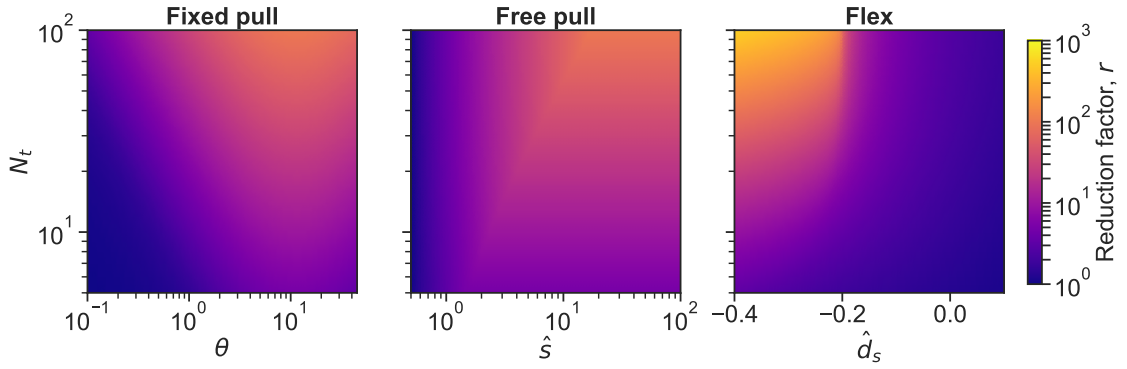

Figure 5.6.: Effect of N_t on reduction factor. Colour plots showing the effect of the number of hairs, N_t, on the reduction factor for each mode of detachment. Here, I fix the dimensionless parameter, $\hat{f}_p = 0.1$. The dimensionless parameters $\hat{d}_s = \frac{d_s - l_{h,0}}{w}$ and $\hat{s} = \frac{s}{L}$, as described in text.

Figures 5.5 and 5.6 can be combined into a single set of colour plots by defining a new dimensionless parameter, $\chi = \hat{f}_p N_t = \frac{f_p N_t}{k_h w}$ (Figure 5.7). Overall, we see that *flex* mode of detachment shows the highest reduction factor among the three modes, with the optimal value of $\chi \sim 1$.

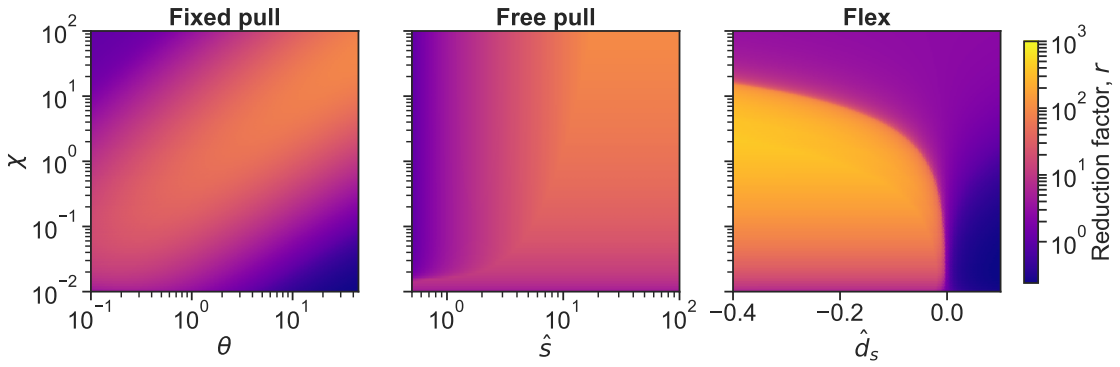

Figure 5.7.: Effect of χ on reduction factor. Here, I define a unified dimensionless design parameter $\chi = \frac{f_p N_t}{k_h w}$, combining $\hat{f}_p$ and N_t into a single number. The dimensionless parameters $\hat{d}_s = \frac{d_s - l_{h,0}}{w}$ and $\hat{s} = \frac{s}{L}$, as described in text.

5.4.3. Detachment pathways:

Based on the three modes of detachment discussed in the previous sections, one can think of several strategies to detach fibrillar adhesive pads from the surface. To illustrate this, let us consider the adhesive system of a dock beetle. The beetle is known to have 3 sets of hairy tarsal adhesive pads in each of their legs, each possessing hairs of different geometries. To keep my analysis simple, I will assume each leg to have only two adhesive pads, with identical hairs of mushroom-shaped geometry. The distal and proximal pads possess roughly 500 and 1000 hairs, respectively[14]. Assuming the pads to be rectangular arrays of 20×25 and 40×25 hairs, I can model this as a one-dimensional system of 20 and 40 *effective hairs*, respectively, by combining the hairs along the width. Based on reported measurements[15], the beetle's *effective hair* is thus considered to have an effective pull-off force, $f_p = 0.5 \times 25 = 12.5$ µN and effective spring constant, $k_h = 0.5 \times 25 = 12.5$ N m^{-1}. The beetle's hairs are approximately $l_{h,0} = 40$ µm long, spaced $w = 10$ µm apart. At end of the tarsal segments, there is a claw, around 200 µm long, and the leg (tibia) is connected roughly at the end of the proximal tarsal pad. This will put $\hat{s}_h = 20$ and $s_l/L = 1$, measured relative to the right end of the distal pad. The beetle's leg is assumed to possess two joints which could serve as a hinge for rotation during detachment (H_1 and H_2 in Figure 5.8 inset). The claw can be used as an external hinge (H_3) by flexing the tarsal pad around it.

Based on the above assumptions, we can come up with force-distance curves to detach the beetle's leg via various pathways (Figure 5.8). First, let us assume the

joint H_2 to be fixed, such that both the distal and proximal pads can be combined to behave like a single long pad with $N_t = 60$ hairs. Path 1 shows the case where the pad shows maximum possible adhesion. Here, the combined pad is vertically pulled upwards while keeping the array perfectly parallel to the surface. If this combined pad is detached by keeping H_1 fixed and maintaining a tilt of 1° with the surface (path 2), the forces dramatically reduces, with around 10 times reduction in the adhesion compared to path 1. We can also detach the pad by switching between the different mechanisms. Path 3 shows one such example, where, initially the leg is pulled vertically up while keeping H_1 fixed, stretching the hairs similar to path 1. On reaching point a, H_1 is set free, which results in a sudden drop in force due to the excess moment by the stretched hairs, tilting the array. Beyond this, the force curve follows the *free pull* mechanism, with ~ 3.5 times reduction in adhesion. An alternate strategy of switching between mechanisms would be to first apply a load on the pad (path 4) and compress the hairs until point b. Beyond this point, the claw can be used as a hinge to detach the pad via flexing it around H_3, which once again reduces the adhesion force. Now, if we assume the joint H_2 to be free such that the two pads can behave distinctly, we can consider the scenario where the proximal pad is flexed around the distal pad at H_2 while keeping H_1 fixed (path 5). After the proximal pad has completely detached, H_1 can be freed up at point c to detach the distal pad via *free pull* with very little force. This pathway results in a ~ 5 times reduction in adhesion.

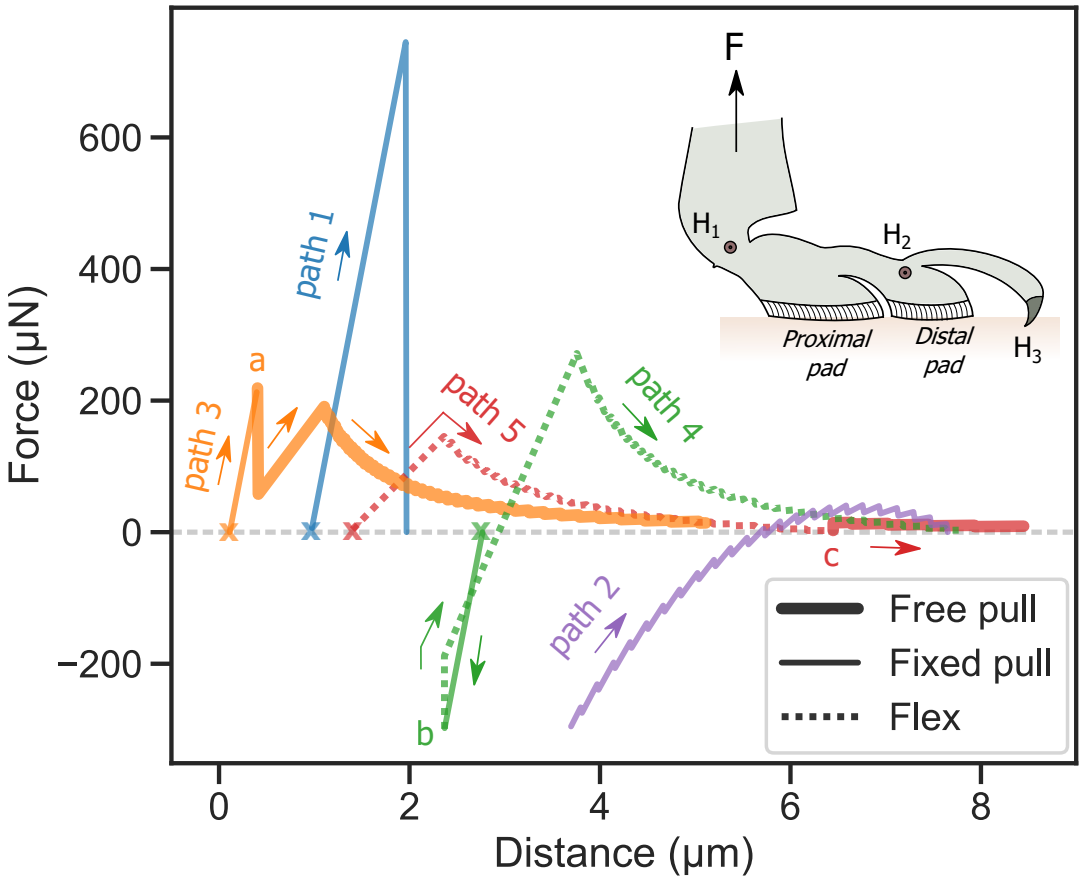

Figure 5.8.: Beetle leg detachment pathways. Force curves showing the theoretical detachment pathways possible for a dock beetle's leg, as function of distance between the pad and the surface. The curves are offset laterally for clarity. Colours represent the distinct detachment pathways, labelled as path 1 to 5, with arrows indicating the direction of retraction. Points a, b and c indicate instances of switching between the different detachment mechanisms for paths 3, 4 and 5 respectively (see text for details). The different line style denotes the specific detachment mechanism followed by any region of the pathway. The inset schematic shows the assumed locations of the different joints or hinges (H_1, H_2 and H_3) employed by the leg.

The above analysis illustrates how the design of the beetle's hairy adhesive pads is suitable for modulating its adhesion. Effective control and release of its joints can help the insect to reduce the pad's adhesion, allowing it to detach with little effort. High reduction in adhesion is seen when the pad is tilted relative to the surface during detachment, as a result of *elastic weakening*. To the best of my knowledge, there is no direct experimental evidence that beetles or any other an-

imal can modulate its adhesion by taking advantage of this effect. Considering that hair deformation occurs at length scales below 10 µm, direct observation of this effect on running beetles would be challenging. A recent study on PDMS micro-pillar arrays, however, does indeed show a strong reduction in the adhesion force due to slight misalignments with the surface[11]. Based on previously reported microscopic investigation of freely walking dock beetles[38], I argue that the following experimental observations provide support to my proposed model: 1) The detachment was shown to follow a three-dimensional twist of the leg, which suggests a complex inhomogeneous deformation of hairs across the array, leading to *elastic weakening*, which is suited for easy detachment. Similar twisting action during detachment was also observed in flies[73] and has been used to easily detach mushroom-shaped artificial adhesive arrays[56]. 2) The beetle can at times instantaneously detach all its legs and drop itself while upside down. This could be explained by the beetle freeing up its joints and using just its body weight to provide the necessary force to detach all its legs via *free pull* (similar to path 3 above). Lateral video recordings showed that in this scenario, claws were the last to detach when a leg loses contact with the surface, which also indicates a *flex* mode of detachment (similar to path 5). 3) Only a fraction of the beetle's pads made contact with the surface during locomotion, which indicates that the pads should naturally be in a slightly tilted state. This not only reduces the contact area, but also non-uniformly deforms the hairs, both leading to a reduction in adhesion for easy detachment. 4) Contact images showed that the array *peels* from the proximal to distal direction during detachment. However, the beetle's hairs are attached to a relatively stiff backing[75], so it wouldn't be able to *peel* its array, since peeling, strictly speaking, depends on the elastic contribution of a thin flexible backing as it bends during the process[59]. Rather, the *peeling* observed in the beetle's case should be a result of the pad detaching from the surface in a tilted orientation, causing the hairs to distinctly detach in sequence. 5) The time scale of detachment was reported to be an order of magnitude shorter than the attachment time scale, which could be a result of the elastic recoil of the leg causing a spontaneous propagation of the detachment front (Figure 5.2).

There exists a limit to how much the pad can tilt, depending on its geometry and material properties. Suppose the hair has a maximum linear elastic strain limit, ε_m, and natural length, $l_{h,0}$. Based on Figure 5.1, if the right most hair is compressed to its elastic limit, one can derive from simple geometry, that, the corresponding

maximum limit in tilt angle is given by:

$$\theta_{limit} = \arctan \frac{l_{h,0}\varepsilon_m}{(N_t - 1)\, w}$$

θ_{limit} will limit the reduction factor for each of the detachment mechanisms presented. Longer hairs can result in a lateral collapse or bundling of hairs, imposing an additional constraint on θ_{limit}. Large deformation of hairs can also lead to buckling, which will further limit the reduction in adhesion due to the smaller effective modulus. Buckling could also, interestingly, promote easier detachment in the *free pull* mode. When the compressed hairs at one end of the array buckle, there would be an excess clockwise moment in the array system (Figure 5.3). This excess moment could subsequently drive the detachment of the remaining hairs. In the case of biological systems, the ability of an insect to provide the load necessary to tilt and compress its hairy adhesive pad against the surface would further introduce limitations to follow any of the detachment modes discussed here. All things considered, the geometry and elastic properties of the individual hairs are crucial parameters to consider in the design of an optimal array system which shows reversible adhesion via *elastic weakening*.

My analysis had been limited to normal forces during detachment. A similar analysis considering the energy required to detach the array will however not yield any *elastic weakening* effect. Since I had assumed a purely elastic system, the initial and final energy of the system would be the same regardless of the mode of detachment, and thus the work of adhesion would remain identical in all scenarios. The reduction of adhesion force is however advantageous since an insect wouldn't then need a strong muscular to system to detach its legs, which are typically capable of attachment forces several times its body weight[31].

5.5. Conclusion

Controlled detachment of a fibrillar system similar to an insect's tarsal hairy adhesive pads can be achieved by either 1) pulling the pad while maintaining a constant tilt angle, 2) pulling the pad while maintaining a free tibia-tarsus leg joint or 3) flexing the pad around the claw. In all three scenarios, an inhomogeneous deformation of hairs across the array results in significant reductions in the net adhesion

due to an elastic effect. Strategic control of the joint's mobility or claw can allow the leg to easily switch between the above mechanisms, thus providing a simple way to reduce adhesion as per necessity. The presence of a deformable leg can further trigger a spontaneous propagation of hair detachment due to the leg's elastic recoil, making it suitable for fast detachment. Arrays with low $\hat{f}_p$ and large number of hairs, with a hair geometry that allows for large deformations while avoiding buckling and lateral bundling represent the optimal design conditions to maximise the range of control over adhesion. The proposed model has been compared with previously reported experimental observations of leg detachment in dock beetles and highlights possible role of the joint and claws to enable reversible adhesion. Similar strategies could potentially be adopted in the design of bio-inspired artificial fibrillar adhesives to easily switch the adhesion state without the need of asymmetric structures.

6. Summary and outlook

My doctoral research work began with a goal to understand the fundamental mechanisms by which some insects such as ladybug beetles can stick to surfaces when underwater. Hosoda and Gorb[47] who reported the first known observation of this insect's special ability hypothesised that an air bubble trapped by the hairy adhesive pad of the beetle was responsible for its underwater adhesion, since the air bubble could exert a certain attractive capillary force between the leg and the surface. In chapter 3, I tested this hypothesis by performing controlled adhesion measurements on a constrained leg of live ladybug beetles while they are submerged underwater. I showed that the trapped bubble, rather, did not appear to have a significant role on its adhesion. Even in the absence of any bubble, its leg showed a strong adhesion to flat hydrophobic surfaces. On the other hand, underwater adhesion on a hydrophilic surface was found to be quite weak, irrespective of whether a bubble was present or not. My experiments thus eliminated the possibility that a trapped air bubble could contribute in the beetle's attachment when submerged underwater. So then what is the real cause of its underwater adhesion? A hint towards answering this question would be that the insect actually also secretes a small amount oily fluid at the tips of its setae. This oily secretion can have quite different interfacial tension or contact angle values with a surface, depending on if the secreted fluid is surrounded by air or water. This implies that its capillary force could be quite different, depending on the surrounding medium and the substrate surface energy. I thus developed a simple theoretical model to estimate the net adhesion of a single adhesive pad resulting from capillary force due to the secretions. The calculated adhesion forces based on this model followed the same trend as the experimentally obtained values for both hydrophilic and hydrophobic surfaces, with or without a trapped air bubble on its leg. The model also showed that, had there been an air bubble trapped around the setal array, its contribution would be relatively negligible when compared to the total force contribution due to the secretions. In this manner, by using a combination of experiments and theory,

I showed that the underwater adhesion in ladybug beetles is primarily governed by the capillary force and wetting properties of its oily secretions.

My results from this work also motivated me to develop a method that would allow surface tension characterisation of the insect's secretions. This can be particularly challenging since the insect secretes a very tiny volume of fluid in the order of a few femtoliters. Thus, any form of characterisations require alternate microscopic techniques. In chapter 4, I described a possible method to make such experiments possible by using Atomic Force Microscopy (AFM). Adhesion force measurements can be performed with the AFM over microscopic liquid droplets deposited on a clean surface. The obtained adhesion values was then compared with a theoretical estimate using numerical simulations in order to back calculate the liquid surface tension. I found that a key experimental trick to enable such AFM measurements was by coating the cantilever probes with a thin layer of polyethylene glycol-based polymer brush. Such a coating prevents the liquid drop from sticking to the AFM tip, since polymer brushes show a very low contact angle hysteresis ($<5°$) to most liquids while simultaneously also having a hydrophilic surface chemistry. The presented method would allow surface tension measurement of liquid droplets with a volume of the order of femtolitres.

In chapter 5, I focused my attention towards the biomechanics of insect detachment. In order to enable locomotion, the insect's leg should not only show a strong adhesion to surfaces, but should also have the ability to quickly detach its leg without much effort. In this regard, based on a theoretical model, I proposed possible strategies by which an insect with hairy adhesive pads could potentially reduce its adhesion during the moment of detachment. Here, I showed that the design of the hairy pad can inherently allow the insect to modulate its maximum adhesion by simply reorienting the tilt angle of the pad relative to the surface while under contact. Such a tilt would cause some of the hairs of the pad to be stretched on one side and compressed on the other side. The resulting net elastic force due to the deformed hairs was found to significantly reduce the pad's adhesion. Further, I showed that the tilt of the pad would also cause its individual hairs to sequentially detach as distinct events rather than simultaneously. This minimised the combined effort of all the hairs and thus also reduced the total adhesion. The insect could modulate the tilt by either using its claws as a hinge or by actuating the muscle joint that connects the adhesive pad to its leg.

The presented work in this dissertation could inspire several areas of future research lines. Capillary forces could perhaps be used as a strategy to design artificial adhesives for underwater applications. Micro-structured adhesives fabricated using soft lithography techniques has been an active research area over the past decades, where the inspiration was taken mostly from geckos to design strong chemical-free 'dry' adhesives that work well in air. Research on artificial underwater adhesives has only gained increased attention in the recent years. Here, a majority of work is focused on either mimicking the strategies used by marine animals, such as designing novel chemicals with similar functional groups as the adhesive secretions of mussels and barnacles, or by designing microscopic suction cups inspired by octopuses or cling fishes. A capillary based approach for underwater adhesion, to my current knowledge, has not yet been explored in detail. Some of my preliminary work in this regard (not included in the dissertation) used artificially fabricated micropillar arrays with mineral oil deposited on the pillar tips to mimic the beetle's hairy adhesive pads. My underwater adhesion measurements did indeed show a similar trend as that of the reported values for the insect. However, a main challenge in such an artificial system was to design a method that would allow liquid bridges to remain at the tips of pillars with minimal volume loss due to repeated contacts. Even in the biological system, it is not quite clear how an insect minimises the continuous loss of fluid during the countless steps that it takes every day, nor is the exact working of its secretion system fully understood. A detailed study in this area could help develop capillary based artificial adhesive systems with a practical application. Further, my proposed detachment mechanisms that would control the adhesion of the microstructured array could also be tested on artificial systems in order to reversibly attach and detach the adhesive. Finally, I had described a new method to perform surface tension measurements on liquid droplets of femtolitre scale volume. This could be particularly useful to study systems that are governed by microscopic wetting phenomena. One example is the influence of atmospheric aerosols created by sea spray on climate change. In this regard, knowledge of the aerosol interfacial properties could provide valuable insights. Climate models typically assume the surface tension value of these aerosol particles since direct measurement on a single particle can be quite difficult. Here, the AFM based method could possibly be used to characterise the aerosols, which should potentially help improve the climate model predictions.

Acknowledgments

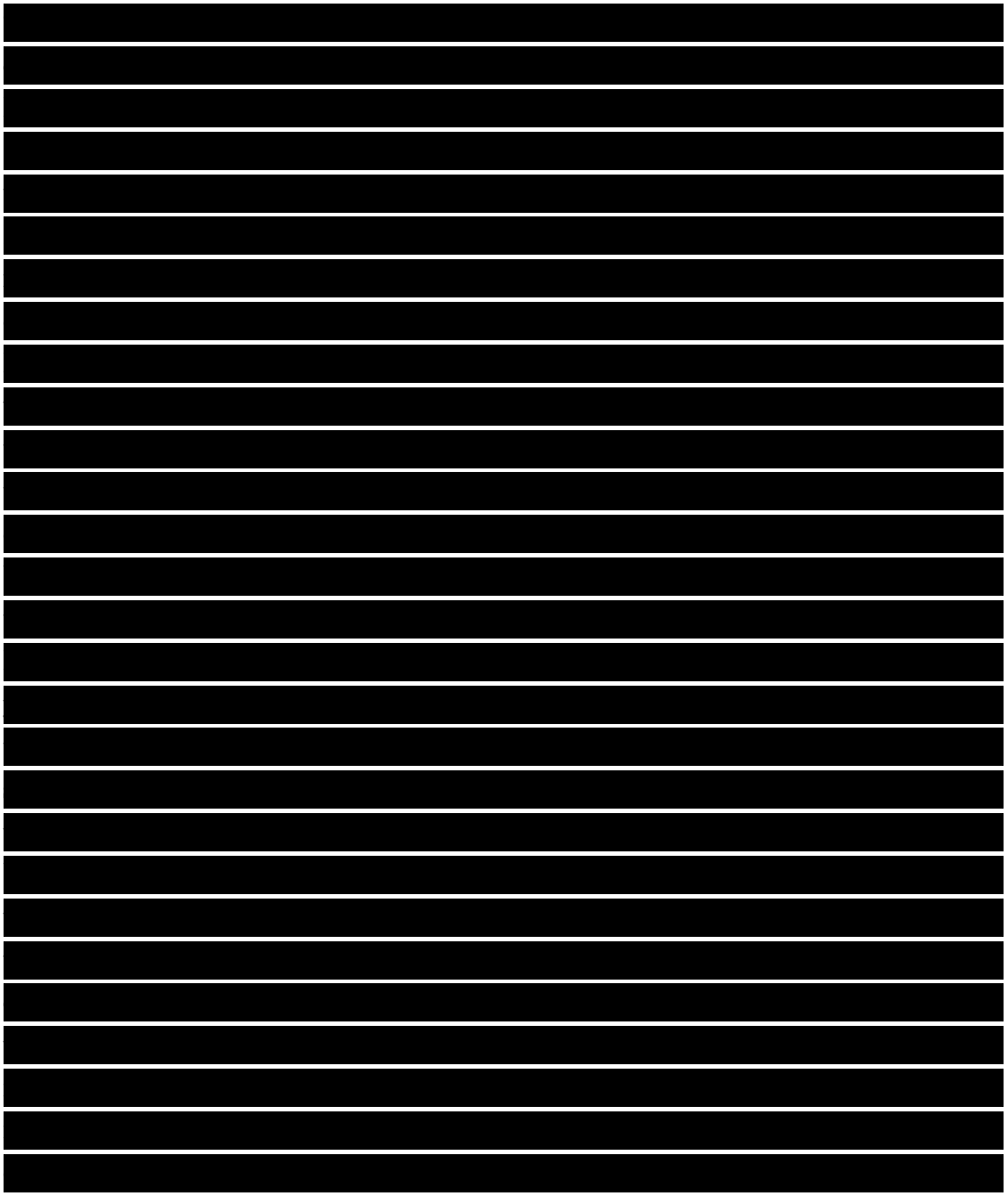

[redacted]

A. Appendix

A.1. Evolver script: Pinned circular bridge

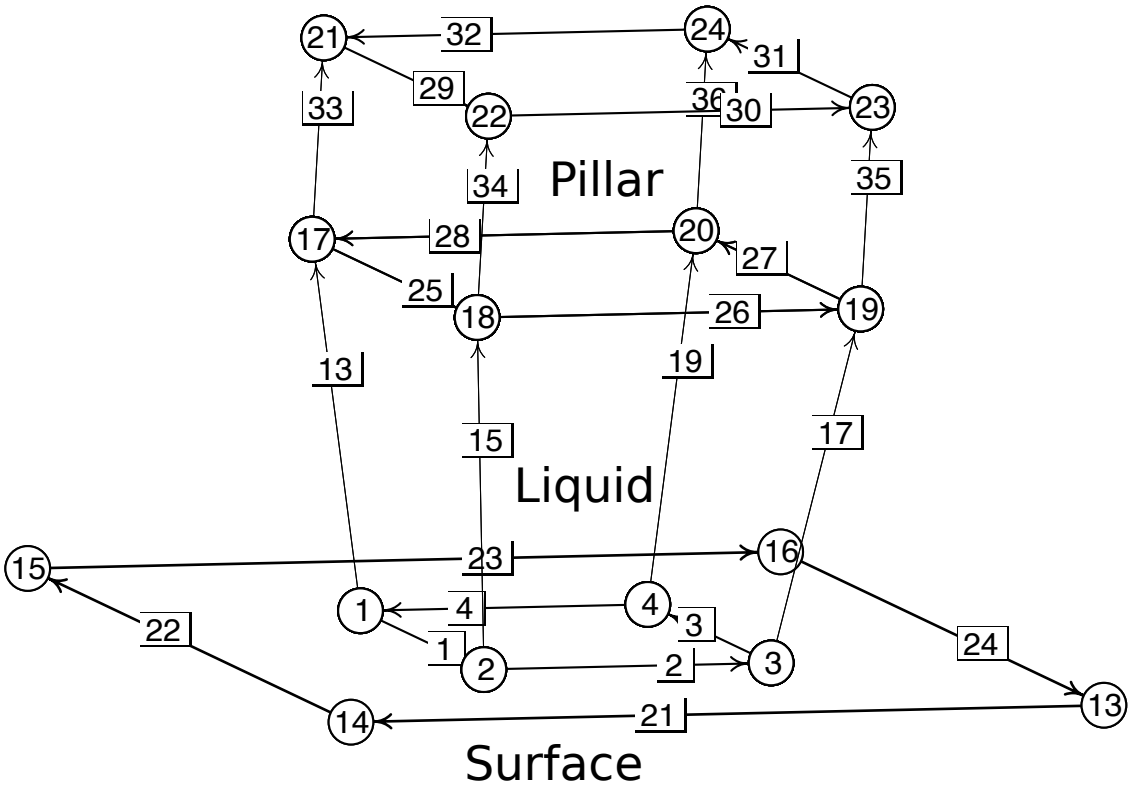

Figure A.1.: Wire diagram

Script file can be found in `https://github.com/PranavSudersan/paper-underwater_adhesion/blob/master/plot%20codes/evolver_ladybug.fe`

```
// circular_bridge_evolver.fe
// Evolver data for bubble between plate and a pillar
// Bottom surface contact angle can be varied
//Bubble is pinned to rim of pillar. Radius can be changed
//Modulus of pillar can be changed to account for elastic deformation
```

```
//Origin at center of bubble between pillar and surface

//CHECK IF CONSTRAINT 5 IS APPLIED ON FACES. REMOVE AS PER REQUIREMENT

//IMPORTANT: Angles taken w.r.t. water (outside) for a
//bubble capillary bridge. For fluid bridge,
//set angles to complement value. Check "CHECK" tags in code.

//CHECK EVOLVE ROUTINE OPTIONS "gogo" BELOW! UNCOMMENT ACCORDINGLY!

//parameter top_angle = 120     // pinning angle (top)
parameter bottom_angle = 130 // contact angle (bottom)
parameter pin_radius = 1.440965 // pinning radius
parameter height = 1.8     // current separation of plates (SET EQUAL
   TO height_start!)
parameter y_modulus = 1E6  // Young's modulus (Y*s/gamma) stiff: 1e6
parameter aspect_ratio = 1 //aspect ratio h/2r
parameter height_start = 0.3     // initial separation of plates
parameter height_end = 0.5     // final separation of plates
parameter dh = 0.025 //height step size
parameter pillar_height = 1//2*pin_radius*aspect_ratio

//pressure 10 //ideal gas model, non-dimensionalized as P/(y/s)

gravity_constant 0  // start with gravity off

keep_macros

view_matrix // view focus on bridge
1 0 0 0
0 1 0 0
0 0 1 0
0 0 0 1.5

#define vol 4*pi/3
#define width (vol/height)^0.5
//#define pillar_height 2*pin_radius*aspect_ratio

// Contact surface tensions
//#define UPPERT  (cos(top_angle*pi/180))  // virtual tension of facet
    on plane
#define LOWERT (cos(bottom_angle*pi/180))
```

```
quantity upper_length info_only method edge_scalar_integral  // top
    contact length
scalar_integrand: 1

quantity lower_length info_only method edge_scalar_integral  // bottom
     contaact length
scalar_integrand: 1

quantity upper_area info_only method edge_vector_integral  // top
    contact area
vector_integrand:
q1: 0
q2: x
q3: 0

quantity lower_area info_only method edge_vector_integral  // bottom
    contact area
vector_integrand:
q1: 0
q2: x
q3: 0

quantity mean_c info_only method mean_curvature_integral  // mean
    curvature

constraint 1 /* the lower plate */
formula: z = -height/2
energy:  // for contact angle
e1: -(LOWERT*y) //+ G*z^2/2*y
e2: 0
e3: 0
content: //volume correction
c1: 0
c2: -z*x
c3: 0

constraint 2/* the upper plate */
formula: z = height/2
//energy:  // for contact angle and gravitational energy under missing
     facets
//e1: -(UPPERT*y) //+ G*z^2/2*y
```

```
//e2: 0
//e3: 0
content:
c1: z*y
c2: 0
c3: 0

constraint pinned convex/* pinning constraint */
formula: x^2 + y^2 = pin_radius^2

//constrain all vertices to lie between plates (not used)
constraint 3 nonpositive
formula: z = (height/2)

constraint 4 nonnegative
formula: z = -(height/2)

//constrain vertices to lie outside pillar region (include in faces
   only) CHECK!
constraint 5 nonnegative //USE ONLY FOR SMALL HEIGHT AND HYDROPHILIC
   SURFACE!!
formula: x^2 + y^2 = pin_radius^2

//constraint plates (not needed)
constraint lower_plate
formula: z = -height/2

constraint upper_plate
formula: z = height/2

constraint pillar_top
formula: z = pillar_height+height/2

// for restoring after perturbation
define vertex attribute old_coord real[3]


vertices
    1   -width/2  -width/2 -height/2  constraint 1,4  /* 4 vertices on
        lower plate */
    2    width/2  -width/2 -height/2  constraint 1,4
    3    width/2   width/2 -height/2  constraint 1,4
```

```
    4   -width/2  width/2 -height/2  constraint 1,4
    5   -width/2  -width/2 height/2  constraint 2,4,pinned  /* upper
        plate */
    6    width/2  -width/2 height/2  constraint 2,4,pinned
    7    width/2  width/2 height/2  constraint 2,4,pinned
    8   -width/2  width/2 height/2  constraint 2,4,pinned
    13   2  2 -height/2 fixed constraint lower_plate/* for lower plane
         */
    14  2 -2 -height/2 fixed constraint lower_plate
    15 -2 -2 -height/2 fixed constraint lower_plate
    16 -2  2 -height/2 fixed constraint lower_plate
    17   -width/2  -width/2 height/2  constraint upper_plate,pinned
        /* pillar */
    18   width/2  -width/2 height/2  constraint upper_plate,pinned
    19   width/2  width/2 height/2  constraint upper_plate,pinned
    20   -width/2  width/2 height/2  constraint upper_plate,pinned
    21   -width/2  -width/2 pillar_height+height/2  constraint
        pillar_top,pinned
    22   width/2  -width/2 pillar_height+height/2  constraint
        pillar_top,pinned
    23   width/2  width/2 pillar_height+height/2  constraint
        pillar_top,pinned
    24   -width/2  width/2 pillar_height+height/2  constraint
        pillar_top,pinned

edges  /* given by endpoints and attribute */
    1   1 2    constraint 1,4 color green lower_length lower_area
        mean_c/* 4 edges on lower plate */
    2   2 3    constraint 1,4 color green lower_length lower_area
        mean_c
    3   3 4    constraint 1,4 color green lower_length lower_area
        mean_c
    4   4 1    constraint 1,4 color green lower_length lower_area
        mean_c
    5   5 6    constraint 2,4,pinned color red upper_length upper_area
         mean_c /* upper plate */
    6   6 7    constraint 2,4,pinned color red upper_length upper_area
         mean_c
    7   7 8    constraint 2,4,pinned color red upper_length upper_area
         mean_c
    8   8 5    constraint 2,4,pinned color red upper_length upper_area
         mean_c
```

```
    13  1 5 constraint 4 mean_c
    15 2 6 constraint 4 mean_c
    17 3 7 constraint 4 mean_c
    19 4 8 constraint 4 mean_c
    21 13 14 no_refine  fixed constraint lower_plate  /* for lower
       plane */
    22 14 15 no_refine  fixed constraint lower_plate
    23 15 16 no_refine  fixed constraint lower_plate
    24 16 13 no_refine  fixed constraint lower_plate
    25 17 18 tension 0  constraint upper_plate,pinned /* pillar */
    26 18 19 tension 0  constraint upper_plate,pinned
    27 19 20 tension 0  constraint upper_plate,pinned
    28 20 17 tension 0  constraint upper_plate,pinned
    29 21 22 tension 0 constraint pillar_top,pinned
    30 22 23 tension 0 constraint pillar_top,pinned
    31 23 24 tension 0 constraint pillar_top,pinned
    32 24 21 tension 0 constraint pillar_top,pinned
    33 17 21 tension 0 constraint pinned
    34 18 22 tension 0 constraint pinned
    35 19 23 tension 0 constraint pinned
    36 20 24 tension 0 constraint pinned

faces  /* given by oriented edge loop */
    1  1 15 -5  -13 constraint 4 frontcolor lightblue //Add constraint
        5 here for log heights
    2  2 17 -6 -15 constraint 4 frontcolor lightblue
    3  3 19 -7 -17 constraint 4 frontcolor lightblue
    4  4  13 -8 -19 constraint 4 frontcolor lightblue
    5 25 34 -29 -33 tension 0 constraint pinned frontcolor red //top
       pillar
    6 26 35 -30 -34 tension 0 constraint pinned frontcolor red
    7 27 36 -31 -35 tension 0 constraint pinned frontcolor red
    8 28 33 -32 -36 tension 0 constraint pinned frontcolor red

bodies  /* one body, defined by its oriented faces */
    1   1 2 3 4    volume vol density 1
    //    2   5 6 7 8 density 0


//------------------------SCRIPT------------------------//
read
```

```
set background white;

//set edge color clear where on_constraint pinned;

//color formatting
set face color lightred where on_constraint pinned;
set face color yellow where on_constraint 4;
//set edge color clear;


re := { refine edges where on_constraint 1 or on_constraint pinned}

// Evolve for low heights <0.5 (set as gogo when needed)
//gogo := {re; g2;
//    {r; u; V; g 2;} 3;
//    U;g20;U;
//        scale_val := scale;
//        set edge color clear where on_constraint pinned;
//        }

//gogo := {re; g2;
//    {r; u; V; g 2;} 3;
//    g100;U;g20;U;
//        scale_val := scale;
//        set edge color clear where on_constraint pinned;
//        }

// Evolve for high heights > 0.5 (set as gogo when needed)
gogo := {g5; re; g5;
        {r; u; V; g 10;} 3;
        g100;U;g100;U;
        scale_val := scale;
        set edge color clear;
        }

// For saving coordinates before perturbation
save_coords := { foreach vertex vv do
                    { set vv.old_coord[1] x;
                      set vv.old_coord[2] y;
                      set vv.old_coord[3] z;
                    }
               }
```

```
// For restoring coordinates after perturbation
restore_coords := { foreach vertex vv do
                        { set vv.x old_coord[1];
                          set vv.y old_coord[2];
                          set vv.z old_coord[3];
                         }
                   }

// Force by central difference of energy minima
compute_force := { save_coords;
                dheight := 0.000001;
                height := height - dheight;
                optimize 1;
                g100;
                lo_energy := total_energy;
                restore_coords;
                height := height + 2*dheight;
                g100;
                hi_energy := total_energy;
                restore_coords;
                height := height - dheight;
                force1 := -(hi_energy - lo_energy)/2/dheight/2/pi;
                /*force calculated by pressure and angle at bottom
                    surface*/
                force2 := (((body[1].pressure-ambient_pressure_value)*
                    lower_area.value)-
                            (lower_length.value*sin(bottom_angle*pi
                                /180)))/2/pi;
                /*force1a := -(hi_energy - lo_energy)/2/dheight;*/
                printf "%-#2.6g\t%-#2.3g\t%-#2.3g\t%-#20.15g\n",
                height,force1,force2,scale_val;
            }

//compute minimum and maximum radius
compute_neck := {
                min_radius := 1e12;
                max_radius := -1;

                foreach vertex vv where on_constraint 4 do
                {
                    vertex_radius := sqrt(vv.x^2 + vv.y^2);
```

```
                    min_radius := minimum(min_radius,vertex_radius);
                    max_radius := maximum(max_radius,vertex_radius);
                    };
                }

//compute contact angle of water at pinned contact line
compute_angle := {
    angle_sum := 0;
    ind := 0;
            foreach vertex vv where on_constraint 2 do
        {
            if vv.vertex_normal[1]*vv.x > 0 or vv.vertex_normal[2]*vv.
                y > 0 then
            {angle_sum := angle_sum+acos(vv.vertex_normal[3]);}
            else
            {angle_sum := angle_sum-acos(vv.vertex_normal[3]);};
            ind++;
        };
        pin_angle := (angle_sum/ind)*180/pi;//take average
        }

//force-distance data
curve := {
        quiet on;

    define ba_list integer[1]; //ARRAY SIZE CHECK!!!
    //ba_list := {24, 120}; //BOTTOM ANGLE LIST
    //ba_list := {30, 130, 174, 179};
    ba_list := {30};

        for (jnx := 1; jnx <= sizeof(ba_list); jnx++)
        {
            bottom_angle := ba_list[jnx];

            printf "Height:\tForce:\tForce_Calc:\tScale\n";

            num := 1+abs((height_end-height_start)/dh);
            if height_end > height_start then {h_step := dh;} else {
                h_step := -dh;};

            // save data
            outdir := "E:/Work/Surface Evolver/Data/Bubble_Bridge
```

```
    /20201123 constant total fluid volume/D_d=70/fluid/";
    //CHECK OUTPUT DIRECTORY
params := sprintf "pr%g_ba%03g_ym%g_ar%g_ap%g",pin_radius,
          bottom_angle,y_modulus,aspect_ratio,
              ambient_pressure_value; //fixed parameters
              for filenames
outname := sprintf "%sdata-%s_hi%2.6g_hf%2.6g.txt",outdir,
           params,height_start,height_end;
printf "Bottom_Angle\tPin_Radius\tElastic_Modulus\
    tAspect_Ratio\tAmbient_Pressure\t"
         "Height\tBase_Height\tHeight_Final\tStrain\tForce\
            tForce_Calc\t"
        "Energy\tArea\tScale\tVolume\tPressure\
            tBottom_Length\t"
        "Top_Length\tBottom_Area\tTop_Area\tMean_Curvature\
            t"
        "Min_Radius\tMax_Radius\tPinning_Angle\tIterations\
            n"
         >> outname;
         //local inx;

total_deform := 0;
height_deform := 1;
h_diff := 1;
h_init := height_start;
deform_newer := h_init;
h_bound1 := -100;
h_bound2 := 100;
inx := 1;
knx := 0;
min_radius := 1e12;
min_radius_tol := 0.01; //radius of rupture
dataline := "";
while inx <= num do
{
    replace_load datafilename;
    if abs(h_diff) > 0.0001 then //converge elastic
        deformation
    {
        if deform_newer < h_bound1 then {height :=
            h_bound1;}
        else if deform_newer >h_bound2 then {height :=
```

```
            h_bound2;}
        else{height := deform_newer;};
    }
    else
        {printf "%s",dataline >> outname;
         height := height_start+inx*h_step;
         h_init := height;
         total_deform := 0;
         deform_newer := 0;
         knx := 0;
         min_radius := 1e12;
         inx++;};
    pillar_height := (2*pin_radius*aspect_ratio)-
        total_deform; //update pillar height
    if inx > num then {break;};
    if knx = 2 or min_radius < min_radius_tol then {
        height_deform := 0; h_diff := 0; continue;}; //
        CHECK! maximum 2 iterations
    bottom_angle := ba_list[jnx];
    recalc;
    gogo; //evolve
    set edge color clear where on_constraint pinned;

    compute_force; //calculate force
    compute_neck; //calculate neck sizes (min and max)
    compute_angle; //calculate top contact angle

    if min_radius < min_radius_tol then {force2 := 0;}; //
        set force as zero after rupture

    h_base := h_init+(aspect_ratio*2*pin_radius);//height
        from substrate to pillar base
    strain := -total_deform/(aspect_ratio*2*pin_radius);

    dataline:= sprintf "%g\t%-#2.3g\t%g\t%-#2.3g\t%g\t
        %-#2.6g\t%-#2.6g\t"
                    "%-#2.6g\t%-#20.15g\t%-#20.15g\t
                        %-#20.15g\t%-#20.15g\t%-#20.15g\t"
                    "%-#20.15g\t%-#20.15g\t%-#20.15g\t
                        %-#20.15g\t%-#20.15g\t"
                    "%-#20.15g\t%-#20.15g\t%-#20.15g\t
                        %-#20.15g\t%g\t%-#20.15g\t%d\n",
```

```
                    bottom_angle, pin_radius, y_modulus,
                        aspect_ratio, ambient_pressure_value
                        , h_init, h_base,
                    height, strain, force1, force2,
                        total_energy, total_area, scale_val,
                        body[1].volume,
                    body[1].pressure, lower_length.value,
                        upper_length.value, lower_area.value
                        ,
                    upper_area.value, mean_c.value,
                        min_radius, max_radius, pin_angle, knx
                        +1;

//CHECK force1 or force2 for deformation calculation
height_deform := (2*pi*force2*(2*pin_radius*
    aspect_ratio)/(y_modulus*pi*pin_radius^2))-
    total_deform;
total_deform := total_deform + height_deform;

if knx = 0 then
    {deform_prev := h_init;
     deform_new := h_init;
     //don't let heights go beyond 0.3,1.8. CHECK!
     deform_newer := maximum(minimum(h_init+(
         total_deform/aspect_ratio),1.8),0.3);//divided
          by aspect ratio for faster convergence
    force_prev := force2;
    force_new := force2;
    //height limits within which solution must lie in
    h_bound1 := minimum(deform_new, deform_newer);
    h_bound2 := maximum(deform_new, deform_newer);
    }
else
    {deform_prev := deform_new;
     deform_new := deform_newer;
    force_prev := force_new;
    force_new := force2;
    k_ratio := (force_new-force_prev)/(deform_new-
        deform_prev);
    k_elastic := (y_modulus*pi*pin_radius^2)/(2*
        pin_radius*aspect_ratio);
    //secant method
```

```
                deform_newer := ((deform_prev*k_ratio)-(k_elastic*
                    h_init)-force_prev)/(k_ratio-k_elastic);
                };
            h_diff := deform_newer - deform_new;
            knx++;
            /* save dump file */
            if abs(h_diff) < 0.0001 then
            {dump sprintf "%s%s_dump%03u-h%2.6g.dmp",outdir,
                        params,inx,height;};
        };
     };
    quiet off;

    }
```

A.2. Evolver script: pyramid

Script file can be found in `https://github.com/PranavSudersan/afm_pyramid/blob/main/pyramid.fe`

```
//pyramid.fe
// A triangular pyramid shaped tip in contact with a liquid drop
//Center of bottom suubstrate is the origin of the coordinate system,
    vertically below the tip
//Pyramid tip is at 'height' distance above surface
//Contact angle of liquid with pyramid and bottom substrate are given
    by angle_p and angle_s respectively

//COMMENT "height" ,"CA_p" an "Rs" PARAMETERS WHEN RUNNING fd_series
    SCRIPT! UNCOMMENT THEM WHEN RUNNING THIS FILE!
//ALWAYS RERUN THIS FILE, THEN COMMENTS ABOVE PARAMETERS BEFORE
    RUNNING EXTERNAL SCRIPTS
parameter height = 0 // distance of pyramid tip from surface
parameter CA_p = 10 * pi/180 //liquid contact angle with pyramid tip
parameter Rs = 2.0 //pinned radius at substrate (REMOVE CONTACT ANGLE
    ENERGY CONSTRAINT 1)
parameter a_dev = 10 //deviation in pyramid geometry angle

parameter w_top =  3 //height of dummy pyramid (only for reference)
//define initial value expression by trial and error for different
    CA_p value and fitting them
parameter w_init = (2/Rs)-height//(((3.492e-5)*((CA_p*180/pi)^2))
    -(0.00814*(CA_p*180/pi))+0.914) - height  //initial wetted height
    of the pyramid


parameter SA = (0 + a_dev) * pi/180 //Side angle of pyramid 17.5
parameter FA = (0 + a_dev) * pi/180 //Front angle of pyramid 15
parameter BA = (0 + a_dev) * pi/180 //Back angle of pyramid 25
parameter tilt = 0 * pi/180 //tilt pyramid around x-axis


parameter TENS = 1 //suface tension of liquid
parameter CA_s = 30 * pi/180 //liquid contact angle with surface (
    REMOVE PINNED CONTACT ONSTRAINT 14)


gravity_constant 0  // start with gravity off
```

```
//scale_limit 0.1
keep_macros

//rotate display
parameter alpha = 20*pi/180 //rotate view around z-axis
parameter beta = 15*pi/180 //rotate view around y-axis
parameter gamma = 0*pi/180 //rotate view around x-axis

//rotation matrix (https://en.wikipedia.org/wiki/Rotation_matrix)
view_matrix
cos(alpha)*cos(beta) cos(alpha)*sin(beta)*sin(gamma)-sin(alpha)*cos(
    gamma) cos(alpha)*sin(beta)*cos(gamma)+sin(alpha)*sin(gamma) 0
sin(alpha)*cos(beta) sin(alpha)*sin(beta)*sin(gamma)+cos(alpha)*cos(
    gamma) sin(alpha)*sin(beta)*cos(gamma)-cos(alpha)*sin(gamma) 0
-sin(beta) cos(beta)*sin(gamma) cos(beta)*cos(gamma) -1
0 0 0 1.7

//surface energy of substrate and pyramid
#define TENS_s (-TENS*(cos(CA_s)))
#define TENS_p (-TENS*(cos(CA_p)))

/* COMPUTE QUANTITIES */

quantity upper_length info_only method edge_scalar_integral  // top
    contact length
scalar_integrand: 1

quantity upper_length6 info_only method edge_scalar_integral  // top
    contact length
scalar_integrand: 1

quantity upper_length7 info_only method edge_scalar_integral  // top
    contact length
scalar_integrand: 1

quantity upper_length8 info_only method edge_scalar_integral  // top
    contact length
scalar_integrand: 1

quantity upper_length9 info_only method edge_scalar_integral  // top
    contact length
scalar_integrand: 1
```

```
quantity lower_length info_only method edge_scalar_integral  // bottom
    contaact length
scalar_integrand: 1

quantity upper_area info_only method edge_vector_integral  // top
   contact area WRONG!
vector_integrand:
q1: 0
q2: x
q3: 0

quantity lower_area info_only method edge_vector_integral  // bottom
   contact area
vector_integrand:
q1: 0
q2: x
q3: 0

quantity mean_c info_only method mean_curvature_integral  // mean
   curvature

///* BOUNDARIES */
//
boundary 1 parameters 1 convex// bottom pinned contact
x1: Rs * cos(p1)
x2: Rs * sin(p1)
x3: 0



/* CONSTRAINTS */

constraint 1   // substrate face
formula: z = 0
//energy: //uncomment to consider oontact angle CHECK! keep if pinning
//e1: 0
//e2: TENS_s * x
//e3: 0

constraint 14 convex// pinning at substrate CHECK! remove if no
   pinning
formula: x^2 + y^2 = Rs^2
```

```
// fix edge center vertex at pyramid for correct calculation of line
    integrals
constraint 26
formula: x = 0

constraint 36
formula: y = 0

//pyramid tip plane constraints
constraint 2 // face 6
formula: y*(cos(tilt)-sin(tilt)*tan(FA)) + (z-height)*(sin(tilt)+cos(
    tilt)*tan(FA)) = 0
energy:
//e1: TENS_p*(1/(1*cos(FA)))*(z-height+(x/tan(SA)))
e1: TENS_p*(1/(1*cos(FA+tilt)))*(z-height+((x/tan(SA))*(cos(tilt)-tan(
    FA)*sin(tilt))))
e2: 0
e3: 0
content:
c1: -(0.5*(tan(FA+tilt)))*((z^2)-(height+((x/tan(SA))*(cos(tilt)-tan(
    FA)*sin(tilt)))^2))
c2: 0
c3: 0

constraint 25 // face 6
formula: y*(cos(tilt)-sin(tilt)*tan(FA)) + (z-height)*(sin(tilt)+cos(
    tilt)*tan(FA)) = 0
energy:
e1: TENS_p*(1/(1*cos(FA+tilt)))*(z-height-((x/tan(SA))*(cos(tilt)-tan(
    FA)*sin(tilt))))
e2: 0
e3: 0
content:
c1: -(0.5*(tan(FA+tilt)))*((z^2)-(height+((x/tan(SA))*(cos(tilt)-tan(
    FA)*sin(tilt)))^2))
c2: 0
c3: 0

constraint 3 // face 7
formula: -x - (y*sin(tilt)*tan(SA)) + (z-height)*(cos(tilt)*tan(SA)) =
    0
```

```
energy:
e1: 0
e2: TENS_p*(1/cos(SA))*(z-height+((y/(tan(FA)*cos(tilt)+sin(tilt)))*(
    cos(tilt)-tan(FA)*sin(tilt))))
e3: 0
content:
c1: 0
c2: -(0.5*(tan(SA)))*((z^2)-(height+((y/(tan(FA)*cos(tilt)+sin(tilt)))
    *(cos(tilt)-tan(FA)*sin(tilt)))^2))
c3: 0

constraint 35 // face 7
formula: -x - (y*sin(tilt)*tan(SA)) + (z-height)*(cos(tilt)*tan(SA)) =
     0
energy:
e1: 0
e2: TENS_p*(1/cos(SA))*(z-height-((y/(tan(BA)*cos(tilt)-sin(tilt)))*(
    cos(tilt)+tan(BA)*sin(tilt))))
e3: 0
content:
c1: 0
c2: -(0.5*(tan(SA)))*((z^2)-(height+((y/(tan(BA)*cos(tilt)-sin(tilt)))
    *(cos(tilt)+tan(BA)*sin(tilt)))^2))
c3: 0

constraint 4 // face 8
formula: -y*(cos(tilt)+sin(tilt)*tan(BA)) + (z-height)*(-sin(tilt)+cos
    (tilt)*tan(BA)) = 0
energy:
e1: -TENS_p*(1/(1*cos(BA-tilt)))*(z-height-((x/tan(SA))*(cos(tilt)+tan
    (BA)*sin(tilt))))
e2: 0
e3: 0
content:
c1: (0.5*(tan(BA-tilt)))*((z^2)-(height+((x/tan(SA))*(cos(tilt)+tan(BA
    )*sin(tilt)))^2))
c2: 0
c3: 0

constraint 45 // face 8
formula: -y*(cos(tilt)+sin(tilt)*tan(BA)) + (z-height)*(-sin(tilt)+cos
    (tilt)*tan(BA)) = 0
```

```
energy:
e1: -TENS_p*(1/(1*cos(BA-tilt)))*(z-height+((x/tan(SA))*(cos(tilt)+tan
    (BA)*sin(tilt))))
e2: 0
e3: 0
content:
c1: (0.5*(tan(BA-tilt)))*((z^2)-(height+((x/tan(SA))*(cos(tilt)+tan(BA
    )*sin(tilt)))^2))
c2: 0
c3: 0

constraint 5 // face 9
formula: x - (y*sin(tilt)*tan(SA)) + (z-height)*(cos(tilt)*tan(SA)) =
    0
energy:
e1: 0
e2: -TENS_p*(1/cos(SA))*(z-height-((y/(tan(BA)*cos(tilt)-sin(tilt)))*(
    cos(tilt)+tan(BA)*sin(tilt))))
e3: 0
content:
c1: 0
c2: (0.5*(tan(SA)))*((z^2)-(height+((y/(tan(BA)*cos(tilt)-sin(tilt)))
    *(cos(tilt)+tan(BA)*sin(tilt)))^2))
c3: 0

constraint 55 // face 9
formula: x + ((y*sin(-tilt)+z*cos(-tilt))-height)*tan(SA) = 0
energy:
e1: 0
e2: -TENS_p*(1/cos(SA))*(z-height+((y/(tan(FA)*cos(tilt)+sin(tilt)))*(
    cos(tilt)-tan(FA)*sin(tilt))))
e3: 0
content:
c1: 0
c2: (0.5*(tan(SA)))*((z^2)-(height+((y/(tan(FA)*cos(tilt)+sin(tilt)))
    *(cos(tilt)-tan(FA)*sin(tilt)))^2))
c3: 0

//keep liquid outside pyramid
constraint 6 nonpositive // face 1
formula: y*(cos(tilt)-sin(tilt)*tan(FA)) + (z-height)*(sin(tilt)+cos(
    tilt)*tan(FA))
```

```
constraint 7 nonpositive // face 2
formula: -x - (y*sin(tilt)*tan(SA)) + (z-height)*(cos(tilt)*tan(SA))

constraint 8 nonpositive // face 3
formula: -y*(cos(tilt)+sin(tilt)*tan(BA)) + (z-height)*(-sin(tilt)+cos
    (tilt)*tan(BA))

constraint 9 nonpositive // face 4
formula: x + ((y*sin(-tilt)+z*cos(-tilt))-height)*tan(SA)

//keep centers on pyramid
constraint 27 // face 6
formula: y*(cos(tilt)-sin(tilt)*tan(FA)) + (z-height)*(sin(tilt)+cos(
    tilt)*tan(FA)) = 0

constraint 37 // face 7
formula: -x - (y*sin(tilt)*tan(SA)) + (z-height)*(cos(tilt)*tan(SA)) =
     0

constraint 47 // face 8
formula: -y*(cos(tilt)+sin(tilt)*tan(BA)) + (z-height)*(-sin(tilt)+cos
    (tilt)*tan(BA)) = 0

constraint 57 // face 9
formula: x + ((y*sin(-tilt)+z*cos(-tilt))-height)*tan(SA) = 0


//pyramid tip constraints
constraint 10
formula: x = 0

constraint 11
formula: y = 0

constraint 12
formula: z = height

//keep liquid above substrate
constraint 13 nonnegative
formula: z
```

```
//keep liquid between faces
constraint 15 nonnegative // face 6
formula: y*(cos(tilt)-sin(tilt)*tan(FA)) + (z-height)*(sin(tilt)+cos(
    tilt)*tan(FA))

constraint 16 nonnegative // face 7
formula: -x - (y*sin(tilt)*tan(SA)) + (z-height)*(cos(tilt)*tan(SA))

constraint 17 nonnegative // face 8
formula: -y*(cos(tilt)+sin(tilt)*tan(BA)) + (z-height)*(-sin(tilt)+cos
    (tilt)*tan(BA))

constraint 18 nonnegative // face 9
formula: x + ((y*sin(-tilt)+z*cos(-tilt))-height)*tan(SA)

// for restoring after perturbation
define vertex attribute old_coord real[3]

/* INITIAL SHAPE SPECIFICATION */

vertices
//liquid bottom substrate (CHECK! include pinning/contact angle
    constraints 14)
//1 -Rs -Rs 0 constraint 1 //substrate contact angle
//2 Rs -Rs 0 constraint 1
//3 Rs Rs 0 constraint 1
//4 -Rs Rs 0 constraint 1
1 5*pi/4 boundary 1 //pinnned contact (bottom)
2 -pi/4 boundary 1
3 pi/4 boundary 1
4 3*pi/4 boundary 1
 //pyramid contact line
 5 -w_init*tan(SA) (-w_init*tan(FA))*cos(tilt)-(w_init)*sin(tilt) (-
     w_init*tan(FA))*sin(tilt)+(w_init)*cos(tilt)+height  constraint
     57,27
 55 0 (-w_init*tan(FA))*cos(tilt)-(w_init)*sin(tilt) (-w_init*tan(FA))
     *sin(tilt)+(w_init)*cos(tilt)+height  constraint 27,26
 6 w_init*tan(SA) (-w_init*tan(FA))*cos(tilt)-(w_init)*sin(tilt) (-
     w_init*tan(FA))*sin(tilt)+(w_init)*cos(tilt)+height  constraint
     27,37
 65 w_init*tan(SA) (0.5*w_init*(tan(BA)-tan(FA)))*cos(tilt)-(w_init)*
     sin(tilt) (w_init*tan(BA))*sin(tilt)+(w_init)*cos(tilt)+height
```

```
    constraint 37,36
 7 w_init*tan(SA) (w_init*tan(BA))*cos(tilt)-(w_init)*sin(tilt) (
    w_init*tan(BA))*sin(tilt)+(w_init)*cos(tilt)+height  constraint
    37,47
 75 0 (w_init*tan(BA))*cos(tilt)-(w_init)*sin(tilt) (w_init*tan(BA))*
    sin(tilt)+(w_init)*cos(tilt)+height  constraint 47,26
 8 -w_init*tan(SA) (w_init*tan(BA))*cos(tilt)-(w_init)*sin(tilt) (
    w_init*tan(BA))*sin(tilt)+(w_init)*cos(tilt)+height  constraint
    47,57
 85 -w_init*tan(SA) (0.5*w_init*(tan(BA)-tan(FA)))*cos(tilt)-(w_init)*
    sin(tilt) (w_init*tan(BA))*sin(tilt)+(w_init)*cos(tilt)+height
    constraint 57,36
10 -w_top*tan(SA) (-w_top*tan(FA))*cos(tilt)-(w_top)*sin(tilt) (-w_top
   *tan(FA))*sin(tilt)+(w_top)*cos(tilt)+height fixed
11 w_top*tan(SA) (-w_top*tan(FA))*cos(tilt)-(w_top)*sin(tilt) (-w_top*
   tan(FA))*sin(tilt)+(w_top)*cos(tilt)+height fixed
12 w_top*tan(SA) (w_top*tan(BA))*cos(tilt)-(w_top)*sin(tilt) (w_top*
   tan(BA))*sin(tilt)+(w_top)*cos(tilt)+height fixed
13 -w_top*tan(SA) (w_top*tan(BA))*cos(tilt)-(w_top)*sin(tilt) (w_top*
   tan(BA))*sin(tilt)+(w_top)*cos(tilt)+height fixed
14 0 0 height fixed

edges
//liquid
1 1 2 constraint 1,14 lower_length lower_area mean_c //bottom
   substrate (CHECK! include pinning/contact angle constraints 14)
2 2 3 constraint 1,14 lower_length lower_area mean_c
3 3 4 constraint 1,14 lower_length lower_area mean_c
4 4 1 constraint 1,14 lower_length lower_area mean_c
5 5 55 constraint 2,16,18 upper_length6 upper_length upper_area mean_c
    //pyramid top contact line
55 55 6 constraint 25,16,18 upper_length6 upper_length upper_area
   mean_c
6 6 65 constraint 3,15,17 upper_length7 upper_length upper_area mean_c
65 65 7 constraint 35,15,17 upper_length7 upper_length upper_area
   mean_c
7 7 75 constraint 4,16,18 upper_length8 upper_length upper_area mean_c
75 75 8 constraint 45,16,18 upper_length8 upper_length upper_area
   mean_c
8 8 85 constraint 5,15,17 upper_length9 upper_length upper_area mean_c
85 85 5 constraint 55,15,17 upper_length9 upper_length upper_area
   mean_c
```

```
9 1 5 constraint 13,9,6 mean_c//liquid-air interface
10 2 6 constraint 13,6,7 mean_c
11 3 7 constraint 13,7,8 mean_c
12 4 8 constraint 13,8,9 mean_c
//pyramid
17 10 11 fixed no_refine
18 11 12 fixed no_refine
19 12 13 fixed no_refine
20 13 10 fixed no_refine
21 14 10 fixed no_refine //edge of pyramid tip
22 14 11 fixed no_refine
23 14 12 fixed no_refine
24 14 13 fixed no_refine

faces
//liquid
1 1 10 -55 -5 -9 constraint 6  tension TENS color yellow //air-liquid
    interface
2 2 11 -65 -6 -10 constraint 7 tension TENS color yellow
3 3 12 -75 -7 -11 constraint 8 tension TENS color yellow
4 4 9 -85 -8 -12 constraint 9 tension TENS color yellow
//pyramid
10 21 17 -22 fixed no_refine tension 0 color red
11 22 18 -23 fixed no_refine tension 0 color red
12 23 19 -24 fixed no_refine tension 0 color red
13 24 20 -21 fixed no_refine tension 0 color red
//14 17 18 19 20 fixed no_refine tension 0 color red

bodies
    1   1 2 3 4 volume 4*pi/3 density 1

//-----------------------SCRIPT-----------------------//

read

//clear edge lines of fluid
clear_lines := {
                set edge color clear where on_constraint 6 or
                    on_constraint 7 or
                            on_constraint 8 or on_constraint 9;
                }
```

```
//compute contact angle of liquid at pinned contact line
compute_angle_bottom := {
    angle_sum := 0;
    ind := 0;
    foreach vertex vv where on_constraint 1 do
        {
            if vv.vertex_normal[1]*vv.x > 0 or vv.vertex_normal[2]*vv.
               y > 0 then
            {angle_sum := angle_sum+acos(vv.vertex_normal[3]);}
            else
            {angle_sum := angle_sum-acos(vv.vertex_normal[3]);};
            ind++;
        };
        pin_angle := (angle_sum/ind);//take average
        //print pin_angle*180/pi;
        }

//TODO: check angles
//compute contact angle of liquid top contact line with z axis
function real get_angle(real c_num) //c_num: constraint number of edge
    {
    angle_sum := 0;
    ind := 0;
    foreach edge ee where on_quantity upper_length and on_constraint
       c_num do
        {
            angle_temp := acos(ee.vertices[1].vertex_normal[3]);
            if ee.vertices[1].vertex_normal[1]*ee.vertices[1].x > 0 or
                 ee.vertices[1].vertex_normal[2]*ee.vertices[1].y > 0
               then
            {angle_sum := angle_sum + angle_temp;}
            else
            {angle_sum := angle_sum - angle_temp;};
            ind++;
        };
    angle1 := (angle_sum/ind)*180/pi;//take average
    //print angle1*180/pi;
    return angle1;

        }
```

```
compute_angle_top := {
    angle6 := 90 + (FA*180/pi) - ((get_angle(2)+get_angle(25))*0.5) +
       (tilt*180/pi); //face 6
    angle7 := 90 + (SA*180/pi) - ((get_angle(3)+get_angle(35))*0.5);
       //face 7
    angle8 := 90 + (BA*180/pi) - ((get_angle(4)+get_angle(45))*0.5)- (
       tilt*180/pi); //face 8
    angle9 := 90 + (SA*180/pi) - ((get_angle(5)+get_angle(55))*0.5);
       //face 9
    printf "%g\t%g\t%g\t%g\t", angle6,angle7,angle8,angle9;
                      }

compute_wetted_height := {
    h1 := max(vertices where on_constraint 2 or on_constraint 25,z);
    h2 := max(vertices where on_constraint 3 or on_constraint 35,z);
    h3 := max(vertices where on_constraint 4 or on_constraint 45,z);
    h4 := max(vertices where on_constraint 5 or on_constraint 55,z);
    wetted_height := (h1+h2+h3+h4)/4; //average wetted height
                               }
//change height
new_height := height //set new_height and run change_height
change_height := { old_height := height; dz := new_height - old_height
   ; height := new_height;
    set vertex z z+dz where z > 0 and (not on_constraint 6 and not
       on_constraint 7 and not on_constraint 8 and not on_constraint
       9);
    set vertex z z*(new_height+w_init)/(old_height+w_init) where
       on_constraint 6 or on_constraint 7 or on_constraint 8 or
       on_constraint 9;
            recalc;
          }


//change Rs (bottom pin radius)
new_Rs := Rs //set new_Rs and run change_Rs
change_Rs := { dRs := (new_Rs - Rs)/(2*sqrt(2)); Rs := new_Rs;
              set vertex y y-dRs where on_constraint 6;
              set vertex x x+dRs where on_constraint 7;
              set vertex y y+dRs where on_constraint 8;
              set vertex x x-dRs where on_constraint 9;
              recalc;
            }
```

```
//special refine routines
re := { refine edges where on_constraint 1;}

re_top := { refine edges where on_constraint 2; refine edges where
   on_constraint 25;
            refine edges where on_constraint 3; refine edges where
               on_constraint 35;
            refine edges where on_constraint 4; refine edges where
               on_constraint 45;
            refine edges where on_constraint 5; refine edges where
               on_constraint 55;}

//refine top facets
re_top2 := {foreach edge ee where on_quantity upper_length do
    {refine ee.facets;};
         }

//refine bottom facets
re_bottom := {foreach edge ee where on_quantity lower_length do
    {refine ee.facets;};
         }

//refine top face edges
re_top3 := {
    foreach vertices vv where on_constraint 27 and on_constraint 57
       do {
        //printf "%g %g %g\\n",x,y,z;
    refine vv.edges where length == max(vv.edges,length);
    };
    foreach vertices vv where on_constraint 27 and on_constraint 37
       do {
        //printf "%g %g %g\\n",x,y,z;
    refine vv.edges where length == max(vv.edges,length);
    };
    foreach vertices vv where on_constraint 37 and on_constraint 47
       do {
        //printf "%g %g %g\\n",x,y,z;
    refine vv.edges where length == max(vv.edges,length);
    };
    foreach vertices vv where on_constraint 47 and on_constraint 57
       do {
```

```
        //printf "%g %g %g\\n",x,y,z;
    refine vv.edges where length == max(vv.edges,length);
    };
         }

//refine top large faces
re_top4 := {
    foreach vertices vv where on_constraint 27 or on_constraint 57 or
       on_constraint 37 or on_constraint 47 do {
        //printf "%g %g %g\\n",x,y,z; //list vv.facets;
        foreach vv.facets ff do {
            vv_count := count(ff.edges where not on_quantity
               upper_length, id);
            if vv_count == 3 then {refine ff;};
                };
            };
    }


//refine edge where length > .0048 and not no_refine;

//Evolve scripts

gogo1 := {re;
        g5; r; g10; r; g20; r; g40; r; u; g100;
        scale_val := scale;
        compute_angle_top; compute_angle_bottom;
        compute_wetted_height;
        }

//better evolve routine
gogo2 := {re; g5;
        {r; u; V; g 10;} 3;
        g100;U;g100;U;
        scale_val := scale;
        compute_angle_top; compute_angle_bottom;
        compute_wetted_height;
        }
    //use for small Rs
gogo3 := {re;re_top3; re_bottom;re;re_top2;g30;
    {r; u; V; g 10;} 3; {r; V;U;g50;U;} 1;//re_top3; u; V;
    //g1000;
```

```
    V;U;g100;U;
        scale_val := scale;
        compute_angle_top; compute_angle_bottom;
        compute_wetted_height;
        }

//use for large Rs
gogo5 := {re_bottom;re;re_top3; re_top4;re_top3; re_top4;re_top2;
   re_bottom;re;g100;re_top;
    {r; u; V; g 100;} 3;//re_bottom;re;{r; u; V; g 100;} 2;//re_top;{r
       ;u;V;g100;} 1;//re_top3; u; V;
    //g1000;
    U;g300;U;
        scale_val := scale;
        compute_angle_top; compute_angle_bottom;
        compute_wetted_height;
        }

//use for small Rs
gogo6 := {g; re_bottom;re;re_top3; re_top4;re_top3; re_top4;re_top2;
   re_bottom;re;g100;re_top;
    {r; u; V; g 100;} 3;//re_bottom;re;{r; u; V; g 100;} 2;//re_top;{r
       ;u;V;g100;} 1;//re_top3; u; V;
    //g1000;
    U;g300;U;
        scale_val := scale;
        compute_angle_top; compute_angle_bottom;
        compute_wetted_height;
        }

gogo4 := {re; g5;
        {r; u; V; g 20;} 3;
        u; V; U; g10; U; u; V; g100; U;g200;U;
        scale_val := scale;
        compute_angle_top; compute_angle_bottom;
        compute_wetted_height;
        }



// For saving coordinates before perturbation
save_coords := { foreach vertex vv do
```

```
                    { set vv.old_coord[1] x;
                      set vv.old_coord[2] y;
                      set vv.old_coord[3] z;
                    }
                }

// For restoring coordinates after perturbation
restore_coords := { foreach vertex vv do
                        { set vv.x old_coord[1];
                          set vv.y old_coord[2];
                          set vv.z old_coord[3];
                         }
                    }

// Force by central difference of energy minima
compute_force := {
                /*force calculated by pressure and angle at bottom
                    surface*/
                force2 := (((body[1].pressure-ambient_pressure_value)*
                    lower_area.value)-
                            (lower_length.value*sin(pin_angle)))/2/pi;
                force1 := (((body[1].pressure-ambient_pressure_value)*
                    upper_area.value)-
                (upper_length6.value*cos(abs((angle6*pi/180)-FA)))-
                (upper_length7.value*cos(abs((angle7*pi/180)-SA)))-
                (upper_length8.value*cos(abs((angle8*pi/180)-BA)))-
                (upper_length9.value*cos(abs((angle9*pi/180)-SA))))/2/
                    pi; //top

            }



//force-distance data
get_fd := {
    //height_start := 0.001; height_end := 0.4; dh := 0.02; //SET
        HEIGHT SEQUENCE CHECK!
    outdir := sprintf "E:/Work/Surface Evolver/afm_pyramid/data
        /20220823_tipangle_sym_height0_ca30/";//TA_%0.0f/",a_dev; //
        CHECK OUTPUT DIRECTORY
    data_name := sprintf "data-CA_p%2.6g-TA_%0.0f",CA_p*180/pi,a_dev;
        //SET FILE NAME
```

```
            quiet on;
            printf "Contact_Radius:\tBottom_Angle:\tForce_Eng:\
                tForce_Calc:\tScale\n";

//            num := 1+abs((height_end-height_start)/dh);
//            if height_end > height_start then {h_step := dh;} else {
    h_step := -dh;};

            // save data
            outname := sprintf "%s%s.txt",outdir,data_name;

        if Rs == 1.0 then {printf "Contact_Radius\tHeight\tForce_Eng\
            tForce_Calc\t"
            "Bottom_Angle\tTop_Angle\tSide_Angle\tFront_Angle\
                tBack_Angle\tCone_Angle\tTilt_Angle\t"
            "Energy\tArea\tScale\tVolume\tPressure\tBottom_Length\t"
        "Top_Length\tBottom_Area\tTop_Area\tMean_curvature\t"
    "Bottom_Angle_Calc\tTop_Angle6\tTop_Angle7\tTop_Angle8\tTop_Angle9
        \tAverage Wetted Height\tInitial_guess_height\n">> outname;}
            else {printf "";};

            dataline := "";


gogo5; //evolve routine

            compute_force; //calculate force
                printf "%g\t%#2.3g\t%-#2.3g\t%-#2.3g\t%-#20.15g\n",
                        height,pin_angle*180/pi,force1,force2,
                            scale_val;

                dataline:= sprintf "%-#2.3g\t%-#2.6g\t%-#20.15g\t
                    %-#20.15g\t"
                                "%g\t%g\t%g\t%g\t%g\t%g\t%g\t"
                                "%-#20.15g\t%-#20.15g\t"
                                "%-#20.15g\t%-#20.15g\t%-#20.15g\t
                                    %-#20.15g\t%-#20.15g\t"
                                "%-#20.15g\t%-#20.15g\t%-#20.15g\t
                                    %-#20.15g\t"
                                "%-#20.15g\t%-#20.15g\t%-#20.15g\t
                                    %-#20.15g\t%-#20.15g\t%-#2.6g\n",
```

```
                                    Rs,height,force1,force2,
                                    CA_s*180/pi,CA_p*180/pi,SA*180/pi,FA
                                        *180/pi,BA*180/pi,a_dev,tilt*180/pi
                                        ,
                                    total_energy,total_area,scale_val,
                                        body[1].volume,
                                    body[1].pressure,lower_length.value,
                                    upper_length.value,lower_area.value,
                                        upper_area.value,mean_c.value,
                                    pin_angle*180/pi,angle6,angle7,angle8,
                                        angle9,wetted_height,w_init;
                 /* save data */
                 printf "%s",dataline >> outname;

                /* save dump file */
                dump sprintf "%s%s_dump-Rs%0.3f.dmp",outdir,data_name,
                    Rs;

//             };
            quiet off;

          }


get_fd2 := {
    height_start := height; height_end := 0.2; dh := 0.005;
    outdir := sprintf "E:/Work/Surface Evolver/afm_pyramid/data
        /20220323_oltespa_fd/Rs_%0.1f/",Rs; //CHECK OUTPUT DIRECTORY
    data_name := sprintf "data-CA_p%2.6g-Rs_%0.1f",CA_p*180/pi,Rs; //
        SET FILE NAME
    quiet on;
    num := 1+abs((height_end-height_start)/dh);
    if height_end > height_start then {h_step := dh;} else {h_step :=
        -dh;};
    inx := 0;
    gogo5;
    while inx < num do
        {

            compute_force;
            // save data
            outname := sprintf "%s%s.txt",outdir,data_name;
```

```
      if height == 0 then {printf "Contact_Radius\tHeight\tForce_Eng
         \tForce_Calc\t"
          "Bottom_Angle\tTop_Angle\tSide_Angle\tFront_Angle\
             tBack_Angle\tTilt_Angle\t"
          "Energy\tArea\tScale\tVolume\tPressure\tBottom_Length\t"
      "Top_Length\tBottom_Area\tTop_Area\tMean_curvature\t"
"Bottom_Angle_Calc\tTop_Angle6\tTop_Angle7\tTop_Angle8\tTop_Angle9
   \tAverage Wetted Height\tInitial_guess_height\n">> outname;}
          else {printf "";};

          printf "%g\t%#2.3g\t%-#2.3g\t%-#2.3g\t%-#20.15g\n",
                      height,pin_angle*180/pi,force1,force2,
                          scale_val;

              dataline:= sprintf "%-#2.3g\t%-#2.6g\t%-#20.15g\t
                 %-#20.15g\t"
                                 "%g\t%g\t%g\t%g\t%g\t%g\t"
                                 "%-#20.15g\t%-#20.15g\t"
                                 "%-#20.15g\t%-#20.15g\t%-#20.15g\t
                                     %-#20.15g\t%-#20.15g\t"
                                 "%-#20.15g\t%-#20.15g\t%-#20.15g\t
                                     %-#20.15g\t"
                                 "%-#20.15g\t%-#20.15g\t%-#20.15g\t
                                     %-#20.15g\t%-#20.15g\t%-#2.6g\n",
                                 Rs,height,force1,force2,
                                 CA_s*180/pi,CA_p*180/pi,SA*180/pi,FA
                                     *180/pi,BA*180/pi,tilt*180/pi,
                                 total_energy,total_area,scale_val,
                                     body[1].volume,
                                 body[1].pressure,lower_length.value,
                                 upper_length.value,lower_area.value,
                                     upper_area.value,mean_c.value,
                                 pin_angle*180/pi,angle6,angle7,angle8,
                                     angle9,wetted_height,w_init;
               /* save data */
               printf "%s",dataline >> outname;

              /* save dump file */
              dump sprintf "%s%s_dump-h%0.3f.dmp",outdir,data_name,
                  height;
```

```
                set vertex z z+h_step where not on_constraint 14;
                height := height + h_step;
                U;g100;U;
                compute_angle_top; compute_angle_bottom;
                    compute_wetted_height;
                inx++;


};
quiet off;




        }
```

A.3. Evolver script: cone

Script file can be found in `https://github.com/PranavSudersan/afm_pyramid/blob/main/cone.fe`

```
//pyramid.fe
// A triangular pyramid shaped tip in contact with a liquid drop
//Center of bottom suubstrate is the origin of the coordinate system,
    vertically below the tip
//Pyramid tip is at 'height' distance above surface
//Contact angle of liquid with pyramid and bottom substrate are given
    by angle_p and angle_s respectively

//COMMENT "height" ,"CA_p" an "Rs" PARAMETERS WHEN RUNNING fd_series
    SCRIPT! UNCOMMENT THEM WHEN RUNNING THIS FILE!
//ALWAYS RERUN THIS FILE, THEN COMMENTS ABOVE PARAMETERS BEFORE
    RUNNING EXTERNAL SCRIPTS
parameter height = 0 // distance of pyramid tip from surface
parameter CA_p = 10 * pi/180 //liquid contact angle with pyramid tip
parameter Rs = 2 //pinned radius at substrate (REMOVE CONTACT ANGLE
    ENERGY CONSTRAINT 1)
parameter tip_angle = 15
parameter cone_angle = tip_angle*pi/180 //deviation in pyramid
    geometry angle
parameter tilt = 0 * pi/180 //tilt pyramid around x-axis

parameter w_top =  3 //height of dummy pyramid (only for reference)
//define initial value expression by trial and error for different
    CA_p value and fitting them
parameter w_init = (2/Rs)-height //(((3.492e-5)*((CA_p*180/pi)^2))
    -(0.00814*(CA_p*180/pi))+0.914) - height  //initial wetted height
    of the pyramid

parameter TENS = 1 //suface tension of liquid
parameter CA_s = 30 * pi/180 //liquid contact angle with surface (
    REMOVE PINNED CONTACT ONSTRAINT 14)



gravity_constant 0  // start with gravity off
//scale_limit 0.1
keep_macros

//rotate display
```

```
parameter alpha = 20*pi/180 //rotate view around z-axis
parameter beta = 15*pi/180 //rotate view around y-axis
parameter gamma = 0*pi/180 //rotate view around x-axis

//rotation matrix (https://en.wikipedia.org/wiki/Rotation_matrix)
view_matrix
cos(alpha)*cos(beta) cos(alpha)*sin(beta)*sin(gamma)-sin(alpha)*cos(
    gamma) cos(alpha)*sin(beta)*cos(gamma)+sin(alpha)*sin(gamma) 0
sin(alpha)*cos(beta) sin(alpha)*sin(beta)*sin(gamma)+cos(alpha)*cos(
    gamma) sin(alpha)*sin(beta)*cos(gamma)-cos(alpha)*sin(gamma) 0
-sin(beta) cos(beta)*sin(gamma) cos(beta)*cos(gamma) -1
0 0 0 1.7

//surface energy of substrate and pyramid
#define TENS_s (-TENS*(cos(CA_s)))
#define TENS_p (-TENS*(cos(CA_p)))
#define Rc w_init*tan(cone_angle)
#define Rct w_top*tan(cone_angle)

/* COMPUTE QUANTITIES */

quantity upper_length info_only method edge_scalar_integral  // top
    contact length
scalar_integrand: 1

quantity lower_length info_only method edge_scalar_integral  // bottom
     contaact length
scalar_integrand: 1

quantity upper_area info_only method edge_vector_integral  // top
    contact area WRONG!
vector_integrand:
q1: 0
q2: x
q3: 0

quantity lower_area info_only method edge_vector_integral  // bottom
    contact area
vector_integrand:
q1: 0
q2: x
q3: 0
```

```
quantity mean_c info_only method mean_curvature_integral  // mean
    curvature


/* CONSTRAINTS */

constraint 1   // substrate face
formula: z = 0
//energy: //uncomment to consider oontact angle CHECK! keep if pinning
//e1: 0
//e2: TENS_s * x
//e3: 0

constraint 2// pinning at substrate CHECK! remove if no pinning
formula: x^2 + y^2 = Rs^2

//cone tip plane constraints
constraint 3// face 6
formula: x^2 + y^2 = (z*tan(cone_angle))^2
energy:
e1: -TENS_p*y/2/sin(cone_angle)
e2: TENS_p*x/2/sin(cone_angle)
e3: 0//TENS_p*z/2/cos(cone_angle)
content:
c1: y*((x^2+y^2)^(0.5))/3/tan(cone_angle)
c2: -x*((x^2+y^2)^(0.5))/3/tan(cone_angle)
c3: 0//(z^2)*tan(cone_angle)/3

constraint 4 // tip contact line
formula: x^2 + y^2 = (z*tan(cone_angle))^2

// for restoring after perturbation
define vertex attribute old_coord real[3]

/* INITIAL SHAPE SPECIFICATION */


Vertices
//vertices of the low pad
1  Rs*cos(0*pi/3)  Rs*sin(0*pi/3)  0   constraints 1,2 fixed
2  Rs*cos(1*pi/3)  Rs*sin(1*pi/3)  0   constraints 1,2 fixed
```

```
3  Rs*cos(2*pi/3)  Rs*sin(2*pi/3)  0   constraints 1,2 fixed
4  Rs*cos(3*pi/3)  Rs*sin(3*pi/3)  0   constraints 1,2 fixed
5  Rs*cos(4*pi/3)  Rs*sin(4*pi/3)  0   constraints 1,2 fixed
6  Rs*cos(5*pi/3)  Rs*sin(5*pi/3)  0   constraints 1,2 fixed
// vertices of the up pad
7  Rc*cos(0*pi/3)  Rc*sin(0*pi/3)  w_init+height  constraint 3
8  Rc*cos(1*pi/3)  Rc*sin(1*pi/3)  w_init+height  constraint 3
9  Rc*cos(2*pi/3)  Rc*sin(2*pi/3)  w_init+height  constraint 3
10 Rc*cos(3*pi/3)  Rc*sin(3*pi/3)  w_init+height  constraint 3
11 Rc*cos(4*pi/3)  Rc*sin(4*pi/3)  w_init+height  constraint 3
12 Rc*cos(5*pi/3)  Rc*sin(5*pi/3)  w_init+height  constraint 3

//to show the lower half sphere
20 Rct*cos(0*pi/3)  Rct*sin(0*pi/3)  w_top+height  constraint 4 fixed
21 Rct*cos(1*pi/3)  Rct*sin(1*pi/3)  w_top+height  constraint 4 fixed
22 Rct*cos(2*pi/3)  Rct*sin(2*pi/3)  w_top+height  constraint 4 fixed
23 Rct*cos(3*pi/3)  Rct*sin(3*pi/3)  w_top+height  constraint 4 fixed
24 Rct*cos(4*pi/3)  Rct*sin(4*pi/3)  w_top+height  constraint 4 fixed
25 Rct*cos(5*pi/3)  Rct*sin(5*pi/3)  w_top+height  constraint 4 fixed
26  0            0          0          fixed constraint 4

Edges
//the edges of the lower pad
1    1  2  constraints 1,2 lower_length lower_area mean_c  fixed
2    2  3  constraints 1,2 lower_length lower_area mean_c  fixed
3    3  4  constraints 1,2 lower_length lower_area mean_c  fixed
4    4  5  constraints 1,2 lower_length lower_area mean_c  fixed
5    5  6  constraints 1,2 lower_length lower_area mean_c  fixed
6    6  1  constraints 1,2 lower_length lower_area mean_c  fixed
//outside edges of the upper pad
7    7  8   constraint 3 upper_length upper_area mean_c
8    8  9   constraint 3 upper_length upper_area mean_c
9    9  10  constraint 3 upper_length upper_area mean_c
10   10 11  constraint 3 upper_length upper_area mean_c
11   11 12  constraint 3 upper_length upper_area mean_c
12   12 7   constraint 3 upper_length upper_area mean_c
//the vertical edges
13   1  7
14   2  8
15   3  9
16   4  10
17   5  11
```

```
18   6  12

//to show the low half sphere
37  20 21  constraint 4 fixed
38  21 22  constraint 4 fixed
39  22 23  constraint 4 fixed
40  23 24  constraint 4 fixed
41  24 25  constraint 4 fixed
42  25 20  constraint 4 fixed
43  20 26  constraint 4 fixed
44  21 26  constraint 4 fixed
45  22 26  constraint 4 fixed
46  23 26  constraint 4 fixed
47  24 26  constraint 4 fixed
48  25 26  constraint 4 fixed

Faces
// defined by oriented edge loops to have outward normal
// the vertical faces
1   1 14  -7 -13 tension TENS color yellow
2   2 15  -8 -14 tension TENS color yellow
3   3 16  -9 -15 tension TENS color yellow
4   4 17 -10 -16 tension TENS color yellow
5   5 18 -11 -17 tension TENS color yellow
6   6 13 -12 -18 tension TENS color yellow
//to show the low half sphere
19   37  44 -43    constraint 4 color red tension 0  fixed
20   38  45 -44    constraint 4 color red tension 0  fixed
21   39  46 -45    constraint 4 color red tension 0  fixed
22   40  47 -46    constraint 4 color red tension 0  fixed
23   41  48 -47    constraint 4 color red tension 0  fixed
24   42  43 -48    constraint 4 color red tension 0  fixed

//to show the bottom of the low pad
//25   -6 -5 -4 -3 -2 -1 constraints 1 no_refine color green tension 0
    fixed

Bodies // defined by oriented face list
1  1 2 3 4 5 6  volume 4*pi/3 density 1


//-------------------------SCRIPT-------------------------//
```

```
read

hessian_normal
unfix vertex where id>=7 and id<=12 // were fixed by being on fixed
    edges
//t .01 // get rid of some stuff

// do this to stop red sphere refining
fixred := { set facet no_refine where color == red;
            set edge ee no_refine where max(ee.facet,color==red) == 1;
          }


//clear edge lines of fluid
clear_lines := {
    set edge color clear where on_constraint 4;
                }

//compute contact angle of liquid at pinned contact line
compute_angle_bottom := {
    angle_sum := 0;
    ind := 0;
    foreach vertex vv where on_constraint 1 do
        {
            if vv.vertex_normal[1]*vv.x > 0 or vv.vertex_normal[2]*vv.
               y > 0 then
            {angle_sum := angle_sum+acos(vv.vertex_normal[3]);}
            else
            {angle_sum := angle_sum-acos(vv.vertex_normal[3]);};
            ind++;
        };
        pin_angle := (angle_sum/ind);//take average
        //print pin_angle*180/pi;
        }

//TODO: check angles
//compute contact angle of liquid top contact line with z axis
function real get_angle(real c_num) //c_num: constraint number of edge
    {
    angle_sum := 0;
    ind := 0;
```

```
    foreach edge ee where on_quantity upper_length do
        {
            angle_temp := acos(ee.vertices[1].vertex_normal[3]);
            if ee.vertices[1].vertex_normal[1]*ee.vertices[1].x > 0 or
                ee.vertices[1].vertex_normal[2]*ee.vertices[1].y > 0
               then
            {angle_sum := angle_sum + angle_temp;}
            else
            {angle_sum := angle_sum - angle_temp;};
            ind++;
        };
    angle1 := (angle_sum/ind)*180/pi;//take average
    //print angle1*180/pi;
    return angle1;

        }


compute_angle_top := {
    angle_sum := 0;
    ind := 0;
    foreach edge ee where on_constraint 3 do
        {
            angle_temp := acos(ee.vertices[1].vertex_normal[3]);
            if ee.vertices[1].vertex_normal[1]*ee.vertices[1].x > 0 or
                ee.vertices[1].vertex_normal[2]*ee.vertices[1].y > 0
               then
            {angle_sum := angle_sum + angle_temp;}
            else
            {angle_sum := angle_sum - angle_temp;};
            ind++;
        };
        angle_avg := (angle_sum/ind)*180/pi;//take average
        angle_top := 90 + (cone_angle*180/pi) - (angle_avg) + (tilt
           *180/pi); //contact angle
    print angle_top;
                    }

compute_wetted_height := {
    h1 := max(vertices where on_constraint 3,z);
    wetted_height := h1-height; //average wetted height
                            }
```

```
//change height
new_height := height //set new_height and run change_height
change_height := { old_height := height; dz := new_height - old_height
    ; height := new_height;
    set vertex z z+dz where z > 0 and (not on_constraint 6 and not
        on_constraint 7 and not on_constraint 8 and not on_constraint
        9);
    set vertex z z*(new_height+w_init)/(old_height+w_init) where
        on_constraint 6 or on_constraint 7 or on_constraint 8 or
        on_constraint 9;
            recalc;
          }


//change Rs (bottom pin radius)
new_Rs := Rs //set new_Rs and run change_Rs
change_Rs := { dRs := (new_Rs - Rs)/(2*sqrt(2)); Rs := new_Rs;
               set vertex y y-dRs where on_constraint 6;
               set vertex x x+dRs where on_constraint 7;
               set vertex y y+dRs where on_constraint 8;
               set vertex x x-dRs where on_constraint 9;
               recalc;
             }

//special refine routines
re := { refine edges where on_constraint 1;}

re_top := { refine edges where on_constraint 3;}

//refine top facets
re_top2 := {foreach edge ee where on_quantity upper_length do
    {refine ee.facets;};
         }

//refine bottom facets
re_bottom := {foreach edge ee where on_quantity lower_length do
    {refine ee.facets;};
         }

//refine top face edges
re_top3 := {
```

```
    foreach vertices vv where on_constraint 3  do {
        //printf "%g %g %g\\n",x,y,z;
    refine vv.edges where length == max(vv.edges,length);
    };
         }

//refine top large faces
re_top4 := {
    foreach vertices vv where on_constraint 3 do {
        //printf "%g %g %g\\n",x,y,z; //list vv.facets;
        foreach vv.facets ff do {
            vv_count := count(ff.edges where not on_quantity
                upper_length, id);
            if vv_count == 3 then {refine ff;};
                };
            };
    }


//refine edge where length > .0048 and not no_refine;

//Evolve scripts

// a typical evolution
gogo0 := { edgeswap edge where id >= 13 and id <= 18;
          g 5;
          r;
          g 5; V; g 5; V; g 5;
          r;
          g 22;
          fixred; compute_angle_top;
        }

gogo1 := {re;
        g5; r; g10; r; g20; r; g40; r; u; g100;
        scale_val := scale;
        compute_angle_top; compute_angle_bottom;
        compute_wetted_height;
        }

//better evolve routine (BEST FOR CONE)
gogo2 := {edgeswap edge where id >= 13 and id <= 18;
```

```
          re_top4; re; g5;
          {r; u; V; g 20;} 4;
          U;g100;U;
          r; u; V; g 10;
          //hessian;hessian;hessian;
          U;g10;U;
         scale_val := scale;
         compute_angle_top; compute_angle_bottom;
         compute_wetted_height;
         clear_lines;
         }

//use for small Rs
gogo3 := {re;re_top3; re_bottom;re;re_top2;g30;
    {r; u; V; g 10;} 3; {r; V;U;g50;U;} 1;//re_top3; u; V;
    //g1000;
    V;U;g100;U;
         scale_val := scale;
         compute_angle_top; compute_angle_bottom;
         compute_wetted_height;
         }

//use for large Rs
gogo5 := {re_bottom;re;re_top3; re_top4;re_top3; re_top4;re_top2;
   re_bottom;re;g100;re_top;
    {r; u; V; g 100;} 3;//re_bottom;re;{r; u; V; g 100;} 2;//re_top;{r
        ;u;V;g100;} 1;//re_top3; u; V;
    //g1000;
    U;g300;U;
         scale_val := scale;
         compute_angle_top; compute_angle_bottom;
         compute_wetted_height;
         }

//use for small Rs
gogo6 := {g; re_bottom;re;re_top3; re_top4;re_top3; re_top4;re_top2;
   re_bottom;re;g100;re_top;
    {r; u; V; g 100;} 3;//re_bottom;re;{r; u; V; g 100;} 2;//re_top;{r
        ;u;V;g100;} 1;//re_top3; u; V;
    //g1000;
    U;g300;U;
         scale_val := scale;
```

```
        compute_angle_top; compute_angle_bottom;
        compute_wetted_height;
        }

gogo4 := {re; g5;
        {r; u; V; g 20;} 3;
        u; V; U; g10; U; u; V; g100; U;g200;U;
        scale_val := scale;
        compute_angle_top; compute_angle_bottom;
        compute_wetted_height;
        }



// For saving coordinates before perturbation
save_coords := { foreach vertex vv do
                    { set vv.old_coord[1] x;
                      set vv.old_coord[2] y;
                      set vv.old_coord[3] z;
                    }
                }

// For restoring coordinates after perturbation
restore_coords := { foreach vertex vv do
                        { set vv.x old_coord[1];
                          set vv.y old_coord[2];
                          set vv.z old_coord[3];
                         }
                   }

// Force by central difference of energy minima
compute_force := {
                /*force calculated by pressure and angle at bottom
                    surface*/
                force2 := (((body[1].pressure-ambient_pressure_value)*
                    lower_area.value)-
                (lower_length.value*sin(pin_angle)))/2/pi; //bottom
                force1 := (((body[1].pressure-ambient_pressure_value)*
                    upper_area.value)-
                (upper_length.value*cos(abs((angle_top*pi/180)-
                    cone_angle))))/2/pi; //top
```

```
            }



//force-distance data
get_fd := {
    //height_start := 0.001; height_end := 0.4; dh := 0.02; //SET
       HEIGHT SEQUENCE CHECK!
    outdir := sprintf "E:/Work/Surface Evolver/afm_pyramid/data
       /20220906_cone_sym_height0_ca10/";//TA_%0.0f/",a_dev; //CHECK
       OUTPUT DIRECTORY
    data_name := sprintf "data-CA_p%2.6g-TA_%0.0f",CA_p*180/pi,
       cone_angle*180/pi; //SET FILE NAME

            quiet on;
            printf "Contact_Radius:\tBottom_Angle:\tForce_Eng:\
               tForce_Calc:\tScale\n";

//            num := 1+abs((height_end-height_start)/dh);
//            if height_end > height_start then {h_step := dh;} else {
   h_step := -dh;};

            // save data
            outname := sprintf "%s%s.txt",outdir,data_name;

        if Rs == 1.0 then {printf "Contact_Radius\tHeight\tForce_Eng\
           tForce_Calc\t"
            "Bottom_Angle\tTop_Angle\tCone_Angle\tTilt_Angle\t"
            "Energy\tArea\tScale\tVolume\tPressure\tBottom_Length\t"
       "Top_Length\tBottom_Area\tTop_Area\tMean_curvature\t"
    "Bottom_Angle_Calc\tTop_Angle_Calc\tAverage Wetted Height\
       tInitial_guess_height\n">> outname;}
            else {printf "";};

            dataline := "";


gogo2; //evolve routine

            compute_force; //calculate force
                printf "%g\t%#2.3g\t%-#2.3g\t%-#2.3g\t%-#20.15g\n",
```

```
                height,pin_angle*180/pi,force1,force2,
                    scale_val;

            dataline:= sprintf "%-#2.3g\t%-#2.6g\t%-#20.15g\t
                %-#20.15g\t"
                                "%g\t%g\t%g\t%g\t"
                                "%-#20.15g\t%-#20.15g\t"
                                "%-#20.15g\t%-#20.15g\t%-#20.15g\t
                                    %-#20.15g\t%-#20.15g\t"
                                "%-#20.15g\t%-#20.15g\t%-#20.15g\t
                                    %-#20.15g\t"
                                "%-#20.15g\t%-#20.15g\t%-#2.6g\n",
                                Rs,height,force1,force2,
                                CA_s*180/pi,CA_p*180/pi,cone_angle
                                    *180/pi,tilt*180/pi,
                                total_energy,total_area,scale_val,
                                    body[1].volume,
                                body[1].pressure,lower_length.value,
                                upper_length.value,lower_area.value,
                                    upper_area.value,mean_c.value,
                                pin_angle*180/pi,angle_top,
                                    wetted_height,w_init;
             /* save data */
             printf "%s",dataline >> outname;

            /* save dump file */
            dump sprintf "%s%s_dump-Rs%0.3f.dmp",outdir,data_name,
                Rs;

        quiet off;

    }
```

Bibliography

(1) Andreas, J. M.; Hauser, E. A.; Tucker, W. B. Boundary Tension by Pendant Drops. *The Journal of Physical Chemistry* **1938**, *42*, 1001–1019, DOI: 10.1021/j100903a002.

(2) Arutinov, G.; Mastrangeli, M.; Heck, G. van; Lambert, P.; Toonder, J. M. J. den; Dietzel, A.; Smits, E. C. P. Capillary Gripping and Self-Alignment: A Route Toward Autonomous Heterogeneous Assembly. *IEEE Transactions on Robotics* **2015**, *31*, 1033–1043, DOI: 10.1109/TRO.2015.2452775.

(3) Arzt, E.; Gorb, S.; Spolenak, R. From Micro to Nano Contacts in Biological Attachment Devices. *Proceedings of the National Academy of Sciences* **2003**, *100*, 10603–6, DOI: 10.1073/pnas.1534701100.

(4) Arzt, E.; Quan, H.; McMeeking, R. M.; Hensel, R. Functional Surface Microstructures Inspired by Nature – From Adhesion and Wetting Principles to Sustainable New Devices. *Progress in Materials Science* **2021**, *120*, 100823, DOI: 10.1016/j.pmatsci.2021.100823.

(5) Attygalle, A. B.; Aneshansley, D. J.; Meinwald, J.; Eisner, T. Defense by Foot Adhesion in a Chrysomelid Beetle (*Hemisphaerota cyanea*): Characterization of the Adhesive Oil. *Zoology* **2000**, *103*, 1–6.

(6) Autumn, K.; Liang, Y. A.; Hsieh, S. T.; Zesch, W.; Chan, W. P.; Kenny, T. W.; Fearing, R.; Full, R. J. Adhesive Force of a Single Gecko Foot-Hair. *Nature* **2000**, *405*, 681–685, DOI: 10.1038/35015073.

(7) Autumn, K.; Sitti, M.; Liang, Y. A.; Peattie, A. M.; Hansen, W. R.; Sponberg, S.; Kenny, T. W.; Fearing, R.; Israelachvili, J. N.; Full, R. J. Evidence for van Der Waals Adhesion in Gecko Setae. *Proceedings of the National Academy of Sciences* **2002**, *99*, 12252, DOI: 10.1073/pnas.192252799.

(8) Bacca, M.; Booth, J. A.; Turner, K. L.; McMeeking, R. M. Load Sharing in Bioinspired Fibrillar Adhesives with Backing Layer Interactions and Interfacial Misalignment. *Journal of the Mechanics and Physics of Solids* **2016**, *96*, 428–444, DOI: 10.1016/j.jmps.2016.04.008.

(9) Bhushan, B. In *Introduction to Tribology*; John Wiley & Sons, Ltd: 2013, pp 199–271, DOI: 10.1002/9781118403259.ch5.

(10) Bohr, N. Determination of the Surface-Tension of Water by the Method of Jet Vibration. *Philosophical Transactions of the Royal Society of London. Series A, Containing Papers of a Mathematical or Physical Character* **1909**, *209*, 281–317.

(11) Booth, J. A.; Bacca, M.; McMeeking, R. M.; Foster, K. L. Benefit of Backing-Layer Compliance in Fibrillar Adhesive Patches—Resistance to Peel Propagation in the Presence of Interfacial Misalignment. *Advanced Materials Interfaces* **2018**, *5*, 1800272, DOI: 10.1002/admi.201800272.

(12) Brakke, K. A. The Surface Evolver. *Experimental Mathematics* **1992**, *1*, 141–165, DOI: 10.1080/10586458.1992.10504253.

(13) Bullock, J. M.; Drechsler, P.; Federle, W. Comparison of Smooth and Hairy Attachment Pads in Insects: Friction, Adhesion and Mechanisms for Direction-Dependence. *The Journal of Experimental Biology* **2008**, *211*, 3333–43, DOI: 10.1242/jeb.020941.

(14) Bullock, J. M.; Federle, W. Division of Labour and Sex Differences between Fibrillar, Tarsal Adhesive Pads in Beetles: Effective Elastic Modulus and Attachment Performance. *The Journal of Experimental Biology* **2009**, *212*, 1876–88, DOI: 10.1242/jeb.030551.

(15) Bullock, J. M.; Federle, W. Beetle Adhesive Hairs Differ in Stiffness and Stickiness: In Vivo Adhesion Measurements on Individual Setae. *Naturwissenschaften* **2011**, *98*, 381–7, DOI: 10.1007/s00114-011-0781-4.

(16) Butt, H.-J.; Graf, K.; Kappl, M., *Physics and Chemistry of Interfaces*; John Wiley & Sons, Ltd: 2003, DOI: 10.1002/3527602313.

(17) Butt, H.-J.; Kappl, M., *Surface and Interfacial Forces*, 2nd ed.; Wiley-VCH Verlag GmbH & Co. KGaA: Weinheim, Germany, 2018, DOI: 10.1002/9783527804351.

(18) Butt, H.-J.; Liu, J.; Koynov, K.; Straub, B.; Hinduja, C.; Roismann, I.; Berger, R.; Li, X.; Vollmer, D.; Steffen, W.; Kappl, M. Contact Angle Hysteresis. *Current Opinion in Colloid & Interface Science* **2022**, *59*, 101574, DOI: 10.1016/j.cocis.2022.101574.

(19) Bzdek, B. R.; Power, R. M.; Simpson, S. H.; Reid, J. P.; Royall, C. P. Precise, Contactless Measurements of the Surface Tension of Picolitre Aerosol Droplets. *Chemical science* **2016**, *7*, 274–285, DOI: 10.1039/c5sc03184b.

(20) Cha, H.; Vahabi, H.; Wu, A.; Chavan, S.; Kim, M.-K.; Sett, S.; Bosch, S. A.; Wang, W.; Kota, A. K.; Miljkovic, N. Dropwise Condensation on Solid Hydrophilic Surfaces. *Science Advances* **2020**, *6*, eaax0746, DOI: 10.1126/sciadv.aax0746.

(21) Chau, A.; Rignier, S.; Delchambre, A.; Lambert, P. Three-Dimensional Model for Capillary Nanobridges and Capillary Forces. *Modelling and Simulation in Materials Science and Engineering* **2007**, *15*, 305–317, DOI: 10.1088/0965-0393/15/3/009.

(22) Chen, Y.; Shih, M.-C.; Wu, M.-H.; Yang, E.-C.; Chi, K.-J. Underwater Attachment Using Hairs: The Functioning of Spatula and Sucker Setae from Male Diving Beetles. *Journal of The Royal Society Interface* **2014**, *11*, DOI: 10.1098/rsif.2014.0273.

(23) Cheng, D. F.; Urata, C.; Yagihashi, M.; Hozumi, A. A Statically Oleophilic but Dynamically Oleophobic Smooth Nonperfluorinated Surface. *Angewandte Chemie* **2012**, *124*, 3010–3013, DOI: 10.1002/ange.201108800.

(24) Coddington, J. A.; Levi, H. W. Systematics and Evolution of Spiders (*Araneae*). *Annual Review of Ecology and Systematics* **1991**, *22*, 565–592, DOI: 10.1146/annurev.es.22.110191.003025.

(25) Cottingham, W. N.; Greenwood, D. A., *An Introduction to the Standard Model of Particle Physics*, 2nd ed.; Cambridge University Press: Cambridge, 2007, DOI: 10.1017/CBO9780511791406.

(26) De Souza, E. J.; Brinkmann, M.; Mohrdieck, C.; Arzt, E. Enhancement of Capillary Forces by Multiple Liquid Bridges. *Langmuir* **2008**, *24*, 8813–8820, DOI: 10.1021/la8005376.

(27) De Gennes, P. G. Wetting: Statics and Dynamics. *Reviews of Modern Physics* **1985**, *57*, 827–863, DOI: 10.1103/RevModPhys.57.827.

(28) Derjaguin, B. Untersuchungen über die Reibung und Adhäsion, IV. *Kolloid-Zeitschrift* **1934**, *69*, 155–164, DOI: 10.1007/BF01433225.

(29) Dirks, J. H. Physical Principles of Fluid-Mediated Insect Attachment - Shouldn't Insects Slip? *Beilstein Journal of Nanotechnology* **2014**, *5*, 1160–6, DOI: 10.3762/bjnano.5.127.

(30) Ditsche, P.; Summers, A. P. Aquatic versus Terrestrial Attachment: Water Makes a Difference. *Beilstein Journal of Nanotechnology* **2014**, *5*, 2424–2439, DOI: 10.3762/bjnano.5.252.

(31) Endlein, T.; Federle, W. To Stick and Not Getting Stuck — Detachment Control in Ants. *Comparative Biochemistry and Physiology Part A: Molecular & Integrative Physiology* **2007**, *146*, S121–S122, DOI: 10.1016/j.cbpa.2007.01.222.

(32) Endlein, T.; Ji, A.; Samuel, D.; Yao, N.; Wang, Z.; Barnes, W. J. P.; Federle, W.; Kappl, M.; Dai, Z. Sticking like Sticky Tape: Tree Frogs Use Friction Forces to Enhance Attachment on Overhanging Surfaces. *Journal of The Royal Society Interface* **2013**, *10*, 20120838, DOI: 10.1098/rsif.2012.0838.

(33) England, M. W.; Sato, T.; Yagihashi, M.; Hozumi, A.; Gorb, S. N.; Gorb, E. V. Surface Roughness Rather than Surface Chemistry Essentially Affects Insect Adhesion. *Beilstein Journal of Nanotechnology* **2016**, *7*, 1471–1479, DOI: 10.3762/bjnano.7.139.

(34) Fabié, L.; Durou, H.; Ondarçuhu, T. Capillary Forces during Liquid Nanodispensing. *Langmuir* **2010**, *26*, 1870–1878, DOI: 10.1021/la902614s.

(35) Federle, W. Why Are so Many Adhesive Pads Hairy? *The Journal of Experimental Biology* **2006**, *209*, 2611–21, DOI: 10.1242/jeb.02323.

(36) Federle, W.; Riehle, M.; Curtis, A. S.; Full, R. J. An Integrative Study of Insect Adhesion: Mechanics and Wet Adhesion of Pretarsal Pads in Ants. *Integrative and Comparative Biology* **2002**, *42*, 1100–1106, DOI: 10.1093/icb/42.6.1100.

(37) Geiselhardt, S. F.; Geiselhardt, S.; Peschke, K. Comparison of Tarsal and Cuticular Chemistry in the Leaf Beetle Gastrophysa Viridula (Coleoptera: Chrysomelidae) and an Evaluation of Solid-Phase Microextraction and Solvent

Extraction Techniques. *Chemoecology* **2009**, *19*, 185, DOI: 10.1007/s00049-009-0021-y.

(38) Gernay, S. M.; Labousse, S.; Lambert, P.; Compere, P.; Gilet, T. Multi-Scale Tarsal Adhesion Kinematics of Freely-Walking Dock Beetles. *Journal of The Royal Society Interface* **2017**, *14*, DOI: 10.1098/rsif.2017.0493.

(39) Gilet, T.; Heepe, L.; Lambert, P.; Compère, P.; Gorb, S. N. Liquid Secretion and Setal Compliance: The Beetle's Winning Combination for a Robust and Reversible Adhesion. *Current Opinion in Insect Science* **2018**, *30*, 19–25, DOI: 10.1016/j.cois.2018.08.002.

(40) Goebel, A.; Lunkenheimer, K. Interfacial Tension of the Water/n-Alkane Interface. *Langmuir* **1997**, *13*, 369–372, DOI: 10.1021/la960800g.

(41) Gorb, S. N.; Beutel, R. G. Evolution of Locomotory Attachment Pads of Hexapods. *Naturwissenschaften* **2001**, *88*, 530–4, DOI: 10.1007/s00114-001-0274-y.

(42) Greiner, C.; del Campo, A.; Arzt, E. Adhesion of Bioinspired Micropatterned Surfaces: Effects of Pillar Radius, Aspect Ratio, and Preload. *Langmuir* **2007**, *23*, 3495–3502, DOI: 10.1021/la0633987.

(43) Hayakawa, D.; Hirano, T.; Mitani, S.; Sakai, K. Measurement of Surface Tension of Liquid Microdroplets through Observation of Droplet Collision. *Japanese Journal of Applied Physics* **2017**, *56*, 07JB02, DOI: 10.7567/JJAP.56.07JB02.

(44) Heepe, L.; Petersen, D. S.; Tölle, L.; Wolff, J. O.; Gorb, S. N. Sexual Dimorphism in the Attachment Ability of the Ladybird Beetle Coccinella Septempunctata on Soft Substrates. *Applied Physics A* **2016**, *123*, 34, DOI: 10.1007/s00339-016-0684-5.

(45) Hensel, R.; Thiemecke, J.; Booth, J. A. Preventing Catastrophic Failure of Microfibrillar Adhesives in Compliant Systems Based on Statistical Analysis of Adhesive Strength. *ACS Applied Materials & Interfaces* **2021**, DOI: 10.1021/acsami.1c00978.

(46) Hooke, R., *Micrographia, or, Some Physiological Descriptions of Minute Bodies Made by Magnifying Glasses : With Observations and Inquiries Thereupon*; The Royal Society: 1665.

(47) Hosoda, N.; Gorb, S. N. Underwater Locomotion in a Terrestrial Beetle: Combination of Surface de-Wetting and Capillary Forces. *Proceedings of the Royal Society B: Biological Sciences* **2012**, *279*, 4236–42, DOI: 10.1098/rspb.2012.1297.

(48) Hsu, P. Y.; Ge, L.; Li, X.; Stark, A. Y.; Wesdemiotis, C.; Niewiarowski, P. H.; Dhinojwala, A. Direct Evidence of Phospholipids in Gecko Footprints and Spatula–Substrate Contact Interface Detected Using Surface-Sensitive Spectroscopy. *Journal of The Royal Society Interface* **2012**, *9*, 657–664, DOI: 10.1098/rsif.2011.0370.

(49) Huber, G.; Mantz, H.; Spolenak, R.; Mecke, K.; Jacobs, K.; Gorb, S. N.; Arzt, E. Evidence for Capillarity Contributions to Gecko Adhesion from Single Spatula Nanomechanical Measurements. *Proceedings of the National Academy of Sciences* **2005**, *102*, 16293–16296, DOI: 10.1073/pnas.0506328102.

(50) Hui, C. Y.; Glassmaker, N. J.; Tang, T.; Jagota, A. Design of Biomimetic Fibrillar Interfaces: 2. Mechanics of Enhanced Adhesion. *Journal of The Royal Society Interface* **2004**, *1*, 35–48, DOI: 10.1098/rsif.2004.0005.

(51) Ishii, S. Adhesion of a Leaf Feeding Ladybird Epilachna Vigintioctomaculta (Coleoptera : Coccinellidae) on a Virtically Smooth Surface. *Applied Entomology and Zoology* **1987**, *22*, 222–228, DOI: 10.1303/aez.22.222.

(52) Israelachvili, J. N., *Intermolecular and Surface Forces*, 3rd ed; Academic Press: Burlington, MA, 2011; 674 pp.

(53) Jagota, A.; Stephen, J. B. Mechanics of Adhesion through a Fibrillar Microstructure. *Integrative and Comparative Biology* **2002**, *42*, 1140–1145, DOI: 10.1093/icb/42.6.1140.

(54) Johnson, K. L.; Kendall, K.; Roberts, A. D. Surface Energy and the Contact of Elastic Solids. *Proceedings of the Royal Society A: Mathematical, Physical and Engineering Sciences* **1971**, *324*, 301–313, DOI: 10.1098/rspa.1971.0141.

(55) Kamperman, M.; Kroner, E.; del Campo, A.; McMeeking, R. M.; Arzt, E. Functional Adhesive Surfaces with "Gecko" Effect: The Concept of Contact Splitting. *Advanced Engineering Materials* **2010**, *12*, 335–348, DOI: 10.1002/adem.201000104.

(56) Kang, O. H.; Lee, S. H.; Yun, J. H.; Yi, H.; Kwak, M. K.; Lee, S. R. Adhesion Tunable Bio-Inspired Dry Adhesives by Twisting. *International Journal of Precision Engineering and Manufacturing* **2017**, *18*, 1433–1437, DOI: 10.1007/s12541-017-0171-8.

(57) Kang, V.; White, R. T.; Chen, S.; Federle, W. Extreme Suction Attachment Performance from Specialised Insects Living in Mountain Streams (Diptera: Blephariceridae). *bioRxiv : the preprint server for biology* **2020**, DOI: 10.1101/2020.09.30.320663.

(58) Kendall, K. The Adhesion and Surface Energy of Elastic Solids. *Journal of Physics D: Applied Physics* **1971**, *4*, 1186–1195, DOI: 10.1088/0022-3727/4/8/320.

(59) Kendall, K. Thin-Film Peeling-the Elastic Term. *Journal of Physics D: Applied Physics* **1975**, *8*, 1449–1452, DOI: 10.1088/0022-3727/8/13/005.

(60) Kim, T. W.; Bhushan, B. The Adhesion Model Considering Capillarity for Gecko Attachment System. *Journal of The Royal Society Interface* **2008**, *5*, 319–327, DOI: 10.1098/rsif.2007.1078.

(61) Langer, M. G.; Ruppersberg, J. P.; Gorb, S. Adhesion Forces Measured at the Level of a Terminal Plate of the Fly's Seta. *Proceedings of the Royal Society B: Biological Sciences* **2004**, *271*, 2209–2215, DOI: 10.1098/rspb.2004.2850.

(62) Lee, H. D.; Estillore, A. D.; Morris, H. S.; Ray, K. K.; Alejandro, A.; Grassian, V. H.; Tivanski, A. V. Direct Surface Tension Measurements of Individual Sub-Micrometer Particles Using Atomic Force Microscopy. *The Journal of Physical Chemistry A* **2017**, *121*, 8296–8305, DOI: 10.1021/acs.jpca.7b04041.

(63) Lee, H. D.; Tivanski, A. V. Atomic Force Microscopy: An Emerging Tool in Measuring the Phase State and Surface Tension of Individual Aerosol Particles. *Annual Review of Physical Chemistry* **2021**, *72*, 235–252, DOI: 10.1146/annurev-physchem-090419-110133.

(64) Lhermerout, R.; Davitt, K. Contact Angle Dynamics on Pseudo-Brushes: Effects of Polymer Chain Length and Wetting Liquid. *Colloids and Surfaces A: Physicochemical and Engineering Aspects* **2019**, *566*, 148–155, DOI: 10.1016/j.colsurfa.2019.01.006.

(65) Lifshitz, E. M.; Hamermesh, M. In *Perspectives in Theoretical Physics*, Pitaevski, L. P., Ed.; Pergamon: Amsterdam, 1992, pp 329–349, DOI: 10.1016/B978-0-08-036364-6.50031-4.

(66) Liu, J.; Sun, Y.; Zhou, X.; Li, X.; Kappl, M.; Steffen, W.; Butt, H.-J. One-Step Synthesis of a Durable and Liquid-Repellent Poly(Dimethylsiloxane) Coating. *Advanced Materials* **2021**, *33*, 2100237, DOI: 10.1002/adma.202100237.

(67) Lo Presti, M.; Rizzo, G.; Farinola, G. M.; Omenetto, F. G. Bioinspired Biomaterial Composite for All-Water-Based High-Performance Adhesives. *Advanced Science* **2021**, *8*, 2004786, DOI: 10.1002/advs.202004786.

(68) Maxwell, J. C. In *The Scientific Papers of James Clerk Maxwell*, Niven, W. D., Ed.; Cambridge Library Collection - Physical Sciences, Vol. 2; Cambridge University Press: Cambridge, 2011, pp 541–591, DOI: 10.1017/CBO9780511710377.058.

(69) McGuiggan, P. M.; Grave, D. A.; Wallace, J. S.; Cheng, S.; Prosperetti, A.; Robbins, M. O. Dynamics of a Disturbed Sessile Drop Measured by Atomic Force Microscopy (AFM). *Langmuir* **2011**, *27*, 11966–11972, DOI: 10.1021/la2023709.

(70) McGuiggan, P. M.; Wallace, J. S. Maximum Force Technique for the Measurement of the Surface Tension of a Small Droplet by AFM. *The Journal of Adhesion* **2006**, *82*, 997–1011, DOI: 10.1080/00218460600876225.

(71) Miles, R. E. H.; Glerum, M. W. J.; Boyer, H. C.; Walker, J. S.; Dutcher, C. S.; Bzdek, B. R. Surface Tensions of Picoliter Droplets with Sub-Millisecond Surface Age. *The Journal of Physical Chemistry A* **2019**, *123*, 3021–3029, DOI: 10.1021/acs.jpca.9b00903.

(72) Mitchell, C. T.; Dayan, C. B.; Drotlef, D. M.; Sitti, M.; Stark, A. Y. The Effect of Substrate Wettability and Modulus on Gecko and Gecko-Inspired Synthetic Adhesion in Variable Temperature and Humidity. *Scientific Reports* **2020**, *10*, 19748, DOI: 10.1038/s41598-020-76484-6.

(73) Niederegger, S.; Gorb, S. Tarsal Movements in Flies during Leg Attachment and Detachment on a Smooth Substrate. *Journal of Insect Physiology* **2003**, *49*, 611–620, DOI: 10.1016/s0022-1910(03)00048-9.

(74) Parsegian, V. A., *Van Der Waals Forces: A Handbook for Biologists, Chemists, Engineers, and Physicists*; Cambridge University Press: New York, 2006; 380 pp.

(75) Peisker, H.; Michels, J.; Gorb, S. N. Evidence for a Material Gradient in the Adhesive Tarsal Setae of the Ladybird Beetle Coccinella Septempunctata. *Nature Communications* **2013**, *4*, 1661, DOI: 10.1038/ncomms2576.

(76) Peisker, H.; Gorb, S. N. Evaporation Dynamics of Tarsal Liquid Footprints in Flies (Calliphora Vicina)and Beetles (Coccinella Septempunctata). *The Journal of Experimental Biology* **2012**, *215*, 1266–1271, DOI: 10.1242/jeb.065722.

(77) Persson, B. N. J. On the Mechanism of Adhesion in Biological Systems. *The Journal of Chemical Physics* **2003**, *118*, DOI: 10.1063/1.1562192.

(78) Sader, J. E.; Larson, I.; Mulvaney, P.; White, L. R. Method for the Calibration of Atomic Force Microscope Cantilevers. *Review of Scientific Instruments* **1995**, *66*, 3789–3798, DOI: 10.1063/1.1145439.

(79) Schargott, M.; Popov, V. L.; Gorb, S. Spring Model of Biological Attachment Pads. *Journal of Theoretical Biology* **2006**, *243*, 48–53, DOI: 10.1016/j.jtbi.2006.05.023.

(80) Singla, S.; Jain, D.; Zoltowski, C. M.; Voleti, S.; Stark, A. Y.; Niewiarowski, P. H.; Dhinojwala, A. Direct Evidence of Acid-Base Interactions in Gecko Adhesion. *Science Advances* **2021**, *7*, eabd9410, DOI: 10.1126/sciadv.abd9410.

(81) Staat, H. J. J.; van der Bos, A.; van den Berg, M.; Reinten, H.; Wijshoff, H.; Versluis, M.; Lohse, D. Ultrafast Imaging Method to Measure Surface Tension and Viscosity of Inkjet-Printed Droplets in Flight. *Experiments in Fluids* **2016**, *58*, 2, DOI: 10.1007/s00348-016-2284-8.

(82) Stark, A. Y.; Badge, I.; Wucinich, N. A.; Sullivan, T. W.; Niewiarowski, P. H.; Dhinojwala, A. Surface Wettability Plays a Significant Role in Gecko Adhesion Underwater. *Proceedings of the National Academy of Sciences* **2013**, *110*, 6340–5, DOI: 10.1073/pnas.1219317110.

(83) Stark, A. Y.; Dryden, D. M.; Olderman, J.; Peterson, K. A.; Niewiarowski, P. H.; French, R. H.; Dhinojwala, A. Adhesive Interactions of Geckos with Wet and Dry Fluoropolymer Substrates. *Journal of The Royal Society Interface* **2015**, *12*, 20150464, DOI: 10.1098/rsif.2015.0464.

(84) Stark, A. Y.; Yanoviak, S. P. Adhesion and Running Speed of a Tropical Arboreal Ant (Cephalotes Atratus) on Wet Substrates. *Royal Society Open Science* **2018**, *5*, 181540–181540, DOI: 10.1098/rsos.181540.

(85) Stork, N. E. Experimental Analysis of Adhesion of Chrysolina Polita (Chrysomelidae: Coleoptera) on a Variety of Surfaces. *The Journal of Experimental Biology* **1980**, *88*, 91, DOI: 10.1242/jeb.88.1.91.

(86) Strutt, J. W. VI. On the Capillary Phenomena of Jets. *Proceedings of the Royal Society of London* **1879**, *29*, 71–97, DOI: 10.1098/rspl.1879.0015.

(87) Sudersan, P.; Kappl, M.; Pinchasik, B. E.; Butt, H. J.; Endlein, T. Wetting of the Tarsal Adhesive Fluid Determines Underwater Adhesion in Ladybird Beetles. *Journal of Experimental Biology* **2021**, *224*, DOI: 10.1242/jeb.242852.

(88) Sudersan, P.; Kappl, M. Mechanisms of Detachment in Fibrillar Adhesive Systems. *Journal of Theoretical Biology* **2023**, *557*, 111315, DOI: 10.1016/j.jtbi.2022.111315.

(89) Sudersan, P.; Müller, M.; Hormozi, M.; Li, S.; Butt, H.-J.; Kappl, M. A Method to Measure Surface Tension of Micro-Droplets Using Standard AFM Cantilever Tips. *submitted for peer-review* **2023**.

(90) Tian, Y.; Pesika, N.; Zeng, H.; Rosenberg, K.; Zhao, B.; McGuiggan, P.; Autumn, K.; Israelachvili, J. Adhesion and Friction in Gecko Toe Attachment and Detachment. *Proceedings of the National Academy of Sciences* **2006**, *103*, 19320–19325, DOI: 10.1073/pnas.0608841103.

(91) Vonnegut, B. Rotating Bubble Method for the Determination of Surface and Interfacial Tensions. *Review of Scientific Instruments* **1942**, *13*, 6–9, DOI: 10.1063/1.1769937.

(92) Waite, J. Nature's Underwater Adhesive Specialist. *International Journal of Adhesion and Adhesives* **1987**, *7*, 9–14, DOI: 10.1016/0143-7496(87)90048-0.

(93) Wang, Y.; Hensel, R. Bioinspired Underwater Adhesion to Rough Substrates by Cavity Collapse of Cupped Microstructures. *Advanced Functional Materials* **2021**, *31*, 2101787, DOI: 10.1002/adfm.202101787.

(94) Wang, Y.; Wang, H.; Bi, S.; Guo, B. Nano-Wilhelmy Investigation of Dynamic Wetting Properties of AFM Tips through Tip-Nanobubble Interaction. *Scientific Reports* **2016**, *6*, 30021, DOI: 10.1038/srep30021.

(95) Weisstein, E. W. Spherical Cap https://mathworld.wolfram.com/ (accessed 25/09/2022).

(96) Wilhelmy, L. Ueber Die Abhängigkeit Der Capillaritäts-Constanten Des Alkohols von Substanz Und Gestalt Des Benetzten Festen Körpers. *Annalen der Physik* **1863**, *195*, 177–217, DOI: 10.1002/andp.18631950602.

(97) Williams, E.; Peterson, J. Convergent and Alternative Designs in the Digital Adhesive Pads of Scincid Lizards. *Science* **1982**, *215*, 1509–1511, DOI: 10.1126/science.215.4539.1509.

(98) Wong, T.-S.; Kang, S. H.; Tang, S. K. Y.; Smythe, E. J.; Hatton, B. D.; Grinthal, A.; Aizenberg, J. Bioinspired Self-Repairing Slippery Surfaces with Pressure-Stable Omniphobicity. *Nature* **2011**, *477*, 443–447, DOI: 10.1038/nature10447.

(99) Yazdanpanah, M. M.; Hosseini, M.; Pabba, S.; Berry, S. M.; Dobrokhotov, V. V.; Safir, A.; Keynton, R. S.; Cohn, R. W. Micro-Wilhelmy and Related Liquid Property Measurements Using Constant-Diameter Nanoneedle-Tipped Atomic Force Microscope Probes. *Langmuir* **2008**, *24*, 13753–13764, DOI: 10.1021/la802820u.

(100) Young, T. III. An Essay on the Cohesion of Fluids. *Philosophical Transactions of the Royal Society of London* **1805**, *95*, 65–87, DOI: 10.1098/rstl.1805.0005.

(101) Zhang, J.; Seeger, S. Superoleophobic Coatings with Ultralow Sliding Angles Based on Silicone Nanofilaments. *Angewandte Chemie International Edition* **2011**, *50*, 6652–6656, DOI: 10.1002/anie.201101008.